Pulsed jet arrays for turbulent separation control

An experimental study

Toma Budanko

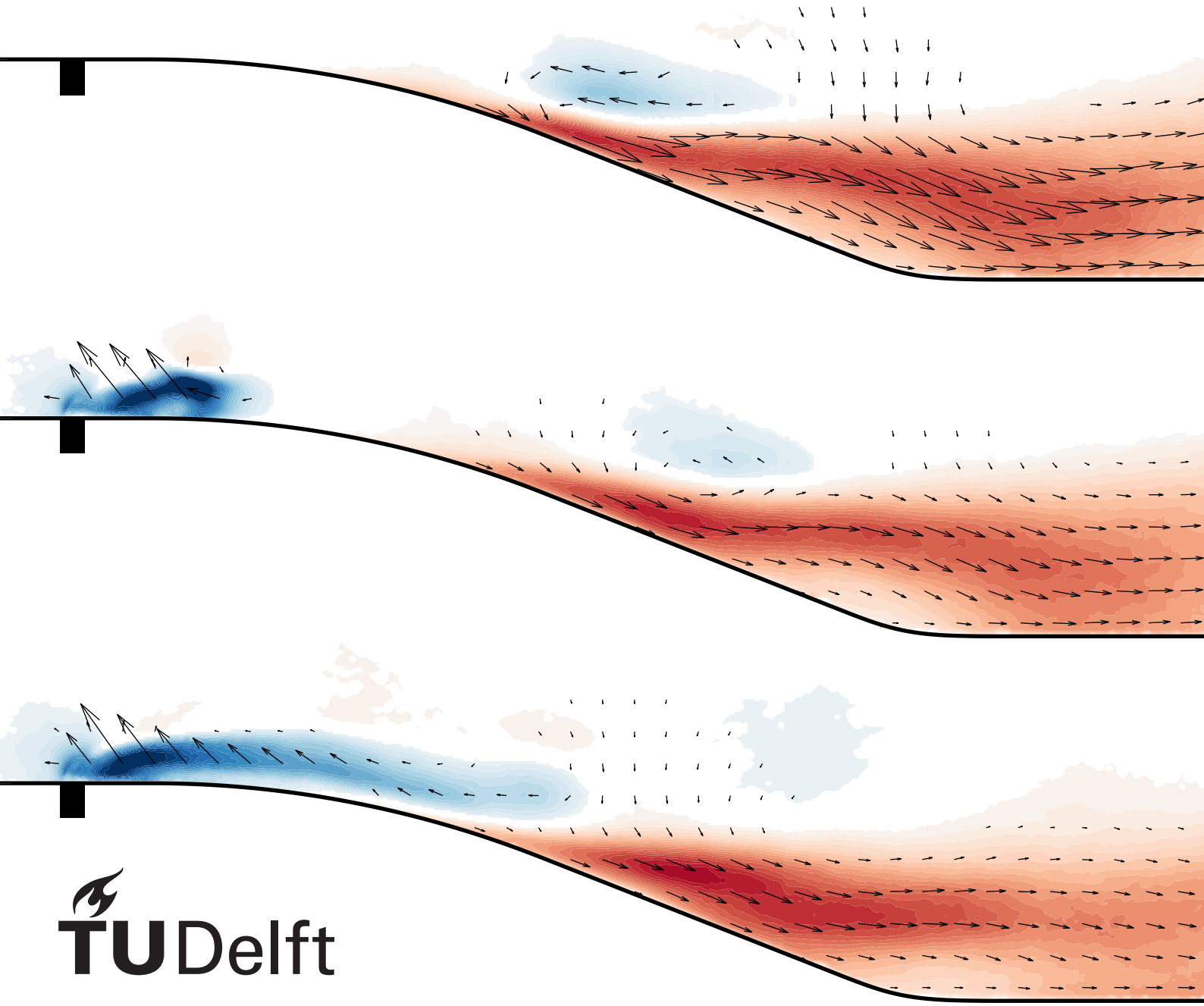

TU Delft

Pulsed jet arrays for turbulent separation control

by

Toma Budanko

to obtain the degree of Master of Science
at the Delft University of Technology,
to be defended publicly on Wednesday July 5, 2023 at 10:00 AM.

Student number:	5253780	
Project duration:	20 September, 2022 – 5 July, 2023	
Thesis supervisors:	Dr. ir. W.J. Baars,	TU Delft
	Dr. M. Kotsonis,	TU Delft

TU Delft

Abstract

An experimental investigation is presented in which an array of pulsed jet actuators is used to control a turbulent separation bubble formed on a curved backward facing ramp. The array is positioned upstream of detachment and consists of wall-normal high aspect ratio skewed rectangular jets which generate streamwise vortices in the boundary layer increasing momentum transfer and delaying separation. While similar systems have shown promise in previous research, this work considers a pressure-induced separation of a relatively high Reynolds number ($Re_\tau = 4600$) turbulent boundary layer (TBL), where the large turbulent structures of the separating BL are of similar scale and magnitude as those generated by actuation and significantly affect the dynamics of detachment.

Both steady blowing and periodic pulsing actuation strategies are tested and compared. Preliminary jet velocity and pulsing frequency sweeps are carried out to identify optimal actuator operating parameters, relying on wall static pressure measurements to evaluate control effectiveness. Select cases of interest are then investigated using two-dimensional two-component particle image velocimetry (PIV) and compared against the uncontrolled baseline which is characterized using PIV and hot wire anemometry. Additional PIV-derived metrics are utilized to assess system performance.

For steady blowing, a jet-to-crossflow velocity ratio $VR > 1$ was required to produce a separation delay, while diminishing improvements in control effect with increasing jet velocity started at $VR = 1.6$ (actuation momentum ratio of $C_\mu = 2.3\%$). This nominal velocity ratio was adopted for all further investigation. The actuator was found to produce alternating strong and weak downwash regions in the TBL resulting in an artificial sweep/ejection pattern at detachment. Periodic forcing with the same nominal velocity ratio was able to achieve better or comparable results to steady actuation, while requiring less input momentum ($C_\mu = 1.2 - 1.8\%$). The optimum actuation frequency was determined to be the natural frequency of the uncontrolled bubble, with the performance of higher frequency actuation tending towards steady blowing levels. As shown by an analysis of flow dynamics based on phase-averaged PIV velocity fields, actuation at the bubble time scales produces significant flow oscillation in phase with actuation. This resonant behaviour results in transient high momentum sweeps between actuation pulses that boost actuator performance, achieving double the performance benefit afforded by steady actuation according to multiple metrics. In comparison, actuation at time scales multiple times shorter than that of the bubble produces a quasi-steady flow and performance comparable to that of steady actuation.

Additionally, a novel alternating actuation strategy is tested, in which the period of active blowing is composed of high frequency alternation between two inverted actuator rows. This aimed to produce a quasi-2D periodic control effect using 3D actuators, which Squire's theorem suggests could excite the separated shear layer instability more than conventional 3D perturbation. While high frequency alternation did achieve a quasi-2D effect, it also prevented the sweep/ejection pattern characteristic of 3D perturbation from forming, thus significantly limiting the actuator performance.

Preface

This thesis and the last 9 months I spent working on it mark the conclusion of my master's degree and my university education. It has at times been challenging, but overall nothing short of joyous and rewarding. The following few lines I devote to the people who made it so.

Firstly, I wish to thank Woutijn and Marios for taking me under their supervision and for so selflessly offering their guidance and support whenever it was needed. I've learned a lot from you and enjoyed the process. Giulio and Theo, thank you for all the help both in and out of the tunnel. More importantly, thank you for all the valuable advice and the time you took to give it. It has been a pleasure.

For the color and texture of my life at TU Delft and beyond, I want to thank my wonderful friends. Gio, Luis, and Ricca, that first year of the pandemic might have been difficult had it not been for your company. As it was, I would not have had it any differently and I think that says everything. Luka and Lukas, we've stuck together across large stretches of time and space and I'm glad we have. Let's keep at it.

Finally, thank you to my wonderful family, my parents, grandparents and Jona, for always believing in me and offering your unfailing support. None of this would have been possible without it. And thank you my dear Toma, for a lifetime of love and friendship. You make life infinitely more beautiful.

Toma Budanko
Delft, June 2023

Contents

List of Figures

List of Tables

Nomenclature

Abbreviations

Abbreviation	Definition
APG	adverse pressure gradient
BM	burst modulation
CRVP	counter-rotating vortex pair
EIF	equivalent inviscid flow
FOV	field of view
HWA	hot wire anemometry
HF	high frequency actuation
ID(R)	incipient detachment (reattachment)
ITD(R)	intermittent transitory detachment (reattachment)
JICF	jet in crossflow
KH	Kelvin-Helmholtz
LF	low frequency actuation
PIV	particle image velocimetry
POD	proper orthogonal decomposition
S	steady blowing control
SVD	singular value decomposition
TBL	turbulent boundary layer
TD(R)	transitory detachment (reattachment)
TKE	turbulent kinetic energy
U	uncontrolled
VGJ	vortex generating jet
ZPG	zero pressure gradient

Symbols

Symbol	Definition	Unit
A_j	actuator orifice area	m^2
C_p	static pressure coefficient	-
c_μ	differential jet-crossflow momentum ratio	-
C_μ	integral actuator-crossflow momentum ratio	-
f	frequency	Hz
f_c	actuation carrier frequency	Hz
f_h	high actuation frequency	Hz
f_l	low actuation frequency	Hz
f_m	actuation modulation frequency	Hz
$f_\#$	f-stop	-
h	ramp height	m
H	shape factor	-
k	turbulent kinetic energy	m^2/s^2
l_z	spanwise length scale	m
M_p	control effectiveness metric: integral difference between measured and inviscid ramp pressure distribution	-
p	pressure	kg/ms^2

Symbol	Definition	Unit
p_m	gauge pressure	kg/ms^2
p_t	total pressure	kg/ms^2
P_2	integrated streamwise momentum flux in plane 2	m^3/s^2
P_d	boundary layer streamwise momentum flux deficit	m^3/s^2
R_{xy}	normalized covariance of variable x and y	-
Re_θ	friction Reynolds number	-
Re_τ	momentum thickness Reynolds number	-
u	instantaneous velocity, x component	m/s
u'	random velocity fluctuation, x component	m/s
$\tilde{u}$	harmonic velocity fluctuation, x component	m/s
u^*	instantaneous velocity, x^* component	m/s
u^+	inner-scaled velocity	-
u_τ	friction velocity	m/s
U	mean velocity, x component	m/s
U_0	reference velocity	m/s
v	instantaneous velocity, y component	m/s
v'	random velocity fluctuation, y component	m/s
$\tilde{v}$	harmonic velocity fluctuation, y component	m/s
v^*	instantaneous velocity, y^* component	m/s
V	mean velocity, y component	m/s
V_j	actuator cavity volume	m^3
VR	jet-crossflow velocity ratio	-
w	instantaneous velocity, z component	m/s
w'	random velocity fluctuation, z component	m/s
$\tilde{w}$	harmonic velocity fluctuation, z component	m/s
W	mean velocity, z component	m/s
s	ramp streamwise surface coordinate	m
St_h	Strouhal number based on ramp height	-
x, y, z	tunnel coordinates	m
x^*, y^*	coordinates of plane 2	m
y^+	inner-scaled wall normal coordinate	-
δ_{99}	nominal boundary layer thickness	m
δ^*	displacement thickness	m
δ_ν	viscous unit	m
δ_ω	vorticitiy thickness	m
θ	momentum thickness	m
λ_j	spanwise jet spacing	m
ν	kinematic viscosity	m^2/s
ρ	density	kg/m^3
τ_w	wall shear stress	kg/ms^2
χ	backflow coefficient	-
Φ	velocity potential	-
Ψ	streamfunction	-

1 Introduction

1.1. Flow separation and separation control

A boundary layer decelerating under the influence of an adverse pressure gradient may separate or detach from the wall if the rate of momentum transport from the freestream is insufficient for a forward flow to be maintained. When the freestream is no longer able to "drag" the boundary layer along, flow reversal occurs at the wall and the point of maximum shear moves away from it. The viscous displacement thickness increases suddenly and significantly which halts the pressure rise while the now free vorticity sheet becomes unstable and rolls up into discrete vortical structures forming a very unsteady flow.

This is almost always a performance detriment, unless the goal was indeed to trigger separation. The large low pressure wake generated behind bluff bodies is a source of significant pressure drag. Wing stall limits the maximum lift a wing can produce while experiencing the same pressure drag increase. Flow separation in a diffuser limits the pressure recovery and dictates the maximum diffuser divergence angle that can be used effectively. In axial compressors the possibility of stall and surge dictates the pressure ratio across each stage and thus the number of stages and the overall size and weight of the device. On top of this, the instability of the separated shear layer causes a strong oscillation of loads that can lead to structural fatigue in the extreme cases.

Minimizing or altogether preventing flow separation is therefore often a fundamental design constraint in fluid dynamics. Furthermore, it is a ubiquitous one, since wherever there is an adverse pressure gradient along a wall, there is the possibility of the flow separating. For all cases of external flow around objects with non-zero thickness, the flow needs to accelerate to round the obstacle experiencing a drop in pressure as it does. Naturally, this implies a necessary pressure recovery at the back of the body to return to freestream conditions. If on top of this, the body creates lift, the acceleration and subsequent deceleration of the flow is further increased on the suction surfaces. Meanwhile, in internal flows it is often necessary to decelerate a flow such that a certain process can take place effectively (e.g. combustion) again exposing the flow to an adverse pressure gradient.

Clearly, controlling the onset and development of flow separation presents a plethora of opportunities to improve engineering systems dependent on fluid flows. Fundamentally, flow separation control aims to replenish the momentum in the near wall regions which has been lost to friction such that a higher pressure rise can be sustained. In the simplest implementation, this is done by directly blowing the momentum deficit tangentially into the boundary layer. However, from a first principles consideration of efficiency, this method is always bound to just break even, so the more elegant approach involves perturbing the flowfield using appropriate *actuators* such that the vast momentum available in the flowfield away from the wall is redirected towards it. The engineering challenge is to minimize the perturbation magnitude required to achieve the target performance.

The potential of this technology is vast which is why it receives continuous attention by the research community both in fundamental research as well as applications to high lift device alternatives, very short diffusers, high pressure ratio compressor stages and the like. There are also a number of less obvious applications, such as trailing edge circulation control which provides a control surface alternative with no moving parts. Although many methods have been developed in a research environment, only the most basic ones, like vortex generators or steady blowing slots, have actually made their way into

practical use. But with the recent push for an increase in aerodynamic efficiency, this might be about to change as the potential benefits of flow control methods are hard to ignore. As an example, DARPA (US government agency) recently announced it is developing the X-65 experimental aircraft as part of the Control of Revolutionary Aircraft with Novel Effectors (CRANE) project (Walan and Lydecker 2023). It will incorporate active flow control methods from early in the design process, which will enable it to maneuver without moving control surfaces and fly at very high angles of attack.

1.2. Research scope

The objective of this research has been to:

> **Develop a pulsed jet flow control system to suppress the pressure-induced separation of a high Reynolds number turbulent boundary layer, experimentally assess its performance and identify the key flowfield features involved.**

The motivation to investigate turbulent, relatively high Reynolds number flow is that it is often encountered in practical applications but relatively less well studied in a separation control context compared to e.g. laminar flow. Some applications where thick high Reynolds boundary layers are encountered and are separating or close to separation are the aft bodies and wing root trailing edges of aircraft, internal flow diffusers and the sterns of naval vessels. The focus of the project is on pressure-induced separation as opposed to that triggered by sharp geometric abberations to increase the relevance of the findings to aerospace or naval applications in which surfaces are generally streamlined.

Turbulent separation control poses some unique challenges. The dissipative nature of turbulence reduces the persistence and coherence of control inputs, which makes the existence of targeted, optimal control strategies less likely (Wu et al. 2022). Furthermore, in a well-developed thick turbulent boundary layer (TBL) the scale of the large outer layer structures can be comparable to the scale of the local flow geometry and the perturbations introduced into the flow by the actuators, leading potentially to significant interaction effects not seen with thin boundary layers. In such situations the dynamics of separation are significantly impacted by the turbulent dynamics of the separating boundary layer.

The control system of choice are pulsed jet arrays fed by pressurized air and operated using fast-acting solenoid valves. For this actuation system the actuation timing and intensity are decoupled and therefore easily independently variable which is not always the case. This actuator therefore offers large control flexibility and operating range which is not only beneficial in application but also allows for a wide investigation of the control parameter space during development. The main drawback to this actuator implementation is a practical one and it is that a source of high pressure air is required. However, in engineering systems where fluid flows are important, such sources are often present, in the form of for example bleed air from a compressor used in another application.

1.3. Research methodology

The project was carried out experimentally in a TBL wind tunnel, where a thick, relatively high Reynolds number TBL is produced by the "long and slow" approach. The long development length ensures a sufficient Reynolds number, while the low speed ensures a thick enough boundary layer which enables much higher measurement resolution. To trigger the formation of a turbulent separation bubble the tunnel is modified by the installation of a curved backward facing ramp on one wall and a further adverse pressure gradient imposed by the contour of the opposite wall.

An actuator system consisting of spanwise arrays of rectangular slits set at alternating skew angles to the incoming flow was designed. Such a jet system in interaction with the crossflow produces an array of counter-rotating streamwise vortices, qualitatively similar to that produced by an array of counter-rotating solid vortex generators which is why such jet arrays are termed *vortex generating jets* or VGJs for short. The actuator contains two jet rows mirrored and offset in the streamwise direction. In the conventional actuation approach only a single row is used, however this project also examines a novel actuation strategy in which the two rows are pulsed in alternation. By alternating the sense of the generated streamwise vortices in this way, the intent is to produce in the time-averaged sense, a more spanwise uniform, "quasi-2D" effect on the flowfield. Properly modulated, this is hypothesized, based on the reviewed literature, to offer an improved ability in the excitation of the separated shear layer instability.

The first research aim was to characterize the baseline turbulent separation bubble. This involved assessing its extents, determining its characteristic frequencies and the associated flowfield modes, such that later the effects of actuation could be compared against the baseline and ultimately connected to the underlying nature of the bubble. Particle image velocimetry (PIV) was used to establish the spatial nature of the flow while hot wire anemometry was used to obtain temporally resolved measurements of the boundary layer upstream of separation and the turbulent separation bubble.

The first step in the investigation of controlled flow were parametric sweeps of actuation momentum and frequency, the purpose of which was to search for operating conditions of interest, where a particularly strong separation control effect was seen. Based on the reviewed literature, there were strong indications that such conditions would be found. This required a fast way of estimating control efficacy, which was achieved by using a metric derived from static pressure measurements along the ramp. Once these points of interest were determined, they were investigated more thoroughly with the ultimate goal of explaining the aerodynamic phenomena at play. For this, PIV was used to quantify changes in the size and shape of the backflow region and the redistribution of streamwise momentum. It then also enabled the identification of coherent actuation-related structures in the flowfield and their dynamics which allowed the mechanisms by which separation control is achieved to be explained.

Based on this research outline two main research questions with further subquestions are defined. The first relates to the characterization of the uncontrolled flow while the second relates to the assessment of the effects of control.

Research Question A: What are the characteristics of a turbulent wall-bounded flow separating from a curved backward facing ramp?

1. What are the inner and outer scales of the boundary layer upstream of separation?
2. How do these scales change as separation is approached?
3. What is the spatial structure and spectral content of the boundary layer?
4. What is the static pressure profile along the tunnel wall?
5. What is the uncontrolled height, length and position of the separation bubble?
6. What are the dominant spatial eigenmodes and eigenfrequencies of the bubble?
7. Are there limitations or short-comings of the experimental set-up?

Research Question B: How effective is an upstream array of dynamically actuated vortex generating jets in reducing the extent of separation?

1. How is the static pressure profile impacted by actuation?
2. How is the length, height and position of the separation bubble impacted by actuation?
3. How does the control effect depend on actuation momentum?
4. How does unsteady actuation compare to steady actuation?
5. What is the optimum actuation frequency?
6. How unsteady is the effect of control?
7. How does the frequency of actuation impact the unsteadiness of the control effect?
8. Which flow structures are identifiable and how do they explain the measured effects on the separation bubble?

1.4. Report outline

Chapter 2 discusses the theoretical background relevant to the separation of turbulent boundary layers and the state-of-the-art in jet actuators for separation control, finishing with a motivation of the current project. The following chapter 3 then presents the design of the experimental set-up, how the experiments were conducted, what measurements were taken and how they were processed. The subsequent three chapters present the results of those measurements and their analysis. Firstly, chapter 4 presents results of preliminary control experiments, including actuator characterization in quiescent flow and jet velocity and pulsing frequency control sweeps. Here optimal operating conditions are identified which are later investigated in more detail. In chapter 5 the features of the uncontrolled flow are discussed to serve as a baseline for the subsequent discussion of the controlled flow features presented in chapter 6. Finally, the report finishes with conclusions and future research recommendations in chapter 7.

2
Background

This chapter provides the theoretical background and relevant literature review for turbulent boundary layer separation control using jets. Section 2.1 discusses turbulent boundary layers and separation, while jet-based separation control is disccussed in section 2.2.

2.1. Turbulent boundary layers and separation

This section covers the fundamental aspects of turbulent boundary layers (TBL) and turbulent separation bubbles (TSB) that are relevant within this project. Firstly, TBL fundamentals are covered, discussing the basic parameters, the velocity profiles and the turbulent structure. Subsequently, the discussion turns to detachment, reattachment and TSB dynamics.

2.1.1. Boundary layer fundamentals

For high Reynolds number flows significant effects of viscosity are confined to the *boundary layer*, a thin near-wall region which vanishes in the limit $Re \to \infty$, in which shear stresses transport flow momentum towards the wall acting as a momentum sink. For low enough Reynolds numbers the boundary layer is laminar with fluid particles following smooth, steady streamlines. Past a certain critical Re and/or in the presence of perturbations, this near wall shear flow becomes unstable and transitions to turbulence. A turbulent boundary layer (TBL), is characterized by swirling fluid particle paths that can be understood as forming eddies with a wide range of scales. This swirling of fluid particles increases momentum transfer by adding a convective component to the existing viscous shear stress. This is why TBLs generate more friction drag and are much more resistant to separation than laminar BLs.

A BL developing over a flat plate is shown in figure 2.1. The coordinate system used has x as the streamwise, y the wall-normal and z the spanwise coordinate. Measuring the extent of the boundary layer is not completely trivial because the viscous effects of wall shear asymptotically drop off towards infinity. The interface between the inviscid and viscous regions of the flow is therefore technically at infinity but is by convention taken to be at the wall-normal position where 99% of the undisturbed velocity is found which represents the boundary layer thickness δ. This is a relatively flawed length scale because the upper region of the TBL velocity profile is so flat that even minor changes or errors in the profile can yield large differences in the measured boundary layer thickness. This is why other more robust measures with meaningful physical interpretations are preferred.

To obtain these measures, an integral analysis of a volume stretching from the leading edge of the plate to some downstream position x and delineated by a streamline far away from the wall ($H \to \infty$) and the flat plate is performed. The continuity equation yields the displacement thickness (expression 2.1), which represents the displacement of the freestream due to the slow-moving fluid in the boundary layer. Meanwhile, the x-momentum equation yields the momentum thickness (expression 2.2), which represents the distance the wall would have to be moved into a completely inviscid fluid for the total

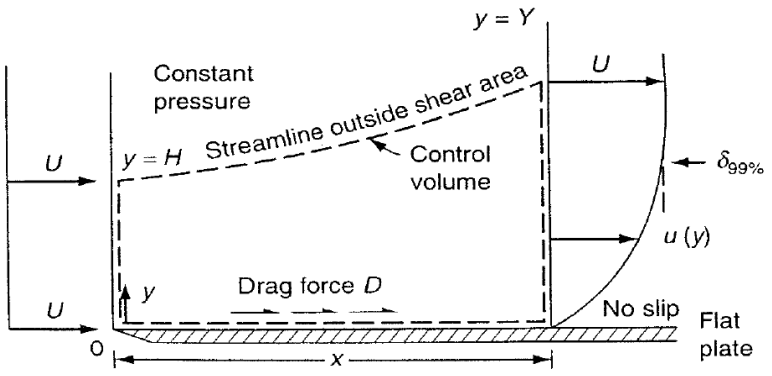

Figure 2.1: A flate plate boundary layer with an integral analysis volume delineated by a streamline outside of the shear region. From White 2006.

flow momentum to be equal to the real flow (Schlichting and Gersten 2016).

$$\delta^* = \int_0^\infty \left(1 - \frac{U(y)}{U_\infty}\right) dy \tag{2.1}$$

$$\theta = \int_0^\infty \frac{U(y)}{U_\infty} \left(1 - \frac{U(y)}{U_\infty}\right) dy \tag{2.2}$$

For the case of zero pressure gradient (ZPG), the momentum thickness is directly related to the integral friction drag of the surface.

$$\theta = \frac{D}{\rho U_\infty^2} \tag{2.3}$$

The shape factor H (expression 2.4) is an indication of the shape of the boundary layer profile, hence the name. A low shape factor represents a thin, full, high wall shear boundary layer. For example, during laminar-turbulent transition, the shape factor drops as the wall shear increases. On the other hand, in an adverse pressure gradient (APG) as the boundary layer approaches separation and the point of maximum shear moves away from the wall, the shape factor grows. From the definitions of the displacement and momentum thicknesses it's clear the shape factor is always larger than 1.

$$H = \frac{\delta^*}{\theta} \tag{2.4}$$

The determination of the above integral parameters requires a reference inviscid flow termed the equivalent inviscid flow. For the flat plate considered above this is a simple constant U_∞ and is independent of boundary layer growth. But for any geometry with streamwise curvature, in the viscous-inviscid interaction framework, the irrotational flow region away from the wall is not equivalent to one that would be obtained for the same geometry without viscosity. This is because the viscous displacement at the wall affects the entire flowfield via a pressure-driven modification of the boundary conditions that is refered to as viscous-inviscid interaction. For example, the formation of boundary layers on an airfoil leads to a virtual decambering of the airfoil that is felt through the entire domain. Therefore the term *equivalent inviscid flow* describes an inviscid flow in which the BCs have been suitably modified such that it tends exactly to the real viscous flow outside of the boundary layer (Lock and Williams 1987).

The BCs are modified either by geometrically offsetting the wall at which the non-permeability condition is applied by the displacement thickness of the BL or via a *transpiration* condition. In the latter approach, a wall-normal velocity, given by expression 2.5 is applied at the non-modified geometrical boundary. Since viscous-inviscid interactions are generally calculated numerically utilizing some domain discretization, this is the preferred approach because the geometry only has to be meshed once.

$$V_w = \frac{d}{ds}(U_i \delta^*) \tag{2.5}$$

In most cases, the BL is thin compared to the streamline curvature, so the wall-normal pressure gradient is negligible in relation, which means that the EIF velocity can simply be assumed to be constant across the BL. In such cases, the the reference EIF velocity U_i is easily observed as the asymptote of the BL profile. However, this is not the case when the boundary layer thickness is of similar magnitude as the streamline curvature and when the EIF velocity changes to a noticeable degree through the boundary layer, because the "BL asymptote" is no longer a constant. This is exactly the case encountered in this research.

In those cases, for the determination of the transpiration BC 2.5 the reference inviscid $U_{i,w}$ is then taken at the wall, while the displacement thickness is defined as

$$\delta^* = \frac{1}{U_{i,w}} \int_0^\delta (U_i - U) dy \tag{2.6}$$

Similarly, the momentum thickness is defined as

$$\theta = \frac{1}{U_{i,w}^2} \int_0^\delta U(U_i - U) + (U_i - U)(U_i - U_{i,w}) dy \tag{2.7}$$

Here both U and U_i are functions of the wall-normal coordinate y. For a more in-depth review of viscous-inviscid interaction, readers are refered to Lock and Williams 1987.

2.1.2. Turbulent boundary layer scaling

A BL velocity profile is first and foremost a function of the wall shear stress τ_w which represents the magnitude of the momentum sink at the wall that gives rise to the BL in the first place. Next, it is a function of the mechanisms which transport momentum towards the wall. Reasoning similar to the domain separation that lead to the concept of the boundary layer based on the relative significance of inertial and viscous forces, also points to a layered TBL. In the fully turbulent *outer layer*, turbulent momentum transport is dominant and viscous transport can be neglected. In the *inner layer*, turbulent fluctuations are strongly damped by the wall so viscous shear is dominant. Finally, there is an *overlap layer* smoothly connecting the two, in which both types of shear are significant.

The inner layer is relatively independent of the freestream conditions, because the pressure forces in this region are negligible compared to the viscous shear stresses in large part because the pressure forces act on a wall-normal crossplane which is small in the near wall-region (Clauser 1956). The inner velocity profile is therefore only dependent on viscosity and wall shear stress. For the outer region, this is not the case and the velocity profile is heavily modified by pressure gradients, but is relatively independent of fluid viscosity.

Dimensional analysis of these functional relations suggests the use of same characteristic velocity scale through the entire TBL, termed the friction velocity u_τ (expression 2.8).

$$u_\tau = \sqrt{\frac{\tau_w}{\rho}} \tag{2.8}$$

On the other hand, two different length scales are used, one for the inner region and one for the outer region, both of which are applicable to the overlap region. The characteristic length scale of the outer region is simply the thickness of the BL δ, while for the inner region it is the so called viscous unit $\delta_\nu = \nu/u_\tau$. Velocity and wall-normal distance are said to be given in wall units when non-dimensionalized with u_τ and δ_ν and are written as u^+ and y^+.

Various Reynolds numbers can be defined from the defined scales. Here two of the most commonly used in the field of TBLs are given. The first is based on momentum thickness as shown by 2.9, while the other is based on the boundary layer thickness and the friction velocity 2.10.

$$Re_\theta = \frac{\theta U_e}{\nu} \tag{2.9}$$

$$Re_\tau = \frac{\delta u_\tau}{\nu} \tag{2.10}$$

It can be seen that the friction Reynolds number is actually the ratio of length scales of the outer and inner regions δ/δ_ν. This gives an intuitive understanding of how the scale separation of wall-bounded turbulence develops as the boundary layer grows and the Reynolds number increases. Note that $y^+ = \frac{y u_\tau}{\nu}$ also has the form of a Reynolds number and as such it suggests, as already mentioned, how the wall-normal distance plays a part in the relative importance of viscous and turbulent stresses.

It's important to note that since a boundary layer is a dynamical system possessing inertia, its state depends not only on present boundary conditions but also on their history. This means that an infinite number of velocity profiles can be generated by applying different pressure gradient histories and that finding a universal velocity profile for a given set of parameters is generally impossible. The outer layer specifically has a much longer response time or length (on the order of hundreds of δ) compared to the inner layer (on the order of multiple δ) due to the scale of structures present within it (Klebanoff and Diehl 1952; Song and Eaton 2004). The exception to this are equilibrium BLs, in which the ratio of pressure and wall shear stress forces, expressed by Clauser's pressure gradient parameter β (expression 2.11), stays constant. A ZPG TBL is one special case of this class of flows.

$$\beta = \frac{\delta^*}{\tau_w}\frac{dp}{dx} \tag{2.11}$$

For this case it is possible to define a single-parameter family of velocity profiles where the parameter is Clauser's β. Because the relevant velocity boundary condition for the outer region is the freestream velocity U_0, the profile is represented relative to an observer moving with the freestream rather than the stationary wall, leading to the *velocity defect* law given by equation 2.12.

$$\frac{U_0 - U}{u_\tau} = g\left(\frac{y}{\delta}, \beta\right) \tag{2.12}$$

For the inner region of the boundary layer, the relevant velocity boundary condition is the no-slip condition of the wall and the velocity profile is formulated as the *law of the wall* given by equation 2.13.

$$u^+ = f\left(y^+\right) \tag{2.13}$$

The inner and outer scaled velocity profiles of a ZPG TBL are shown in figure 2.2.

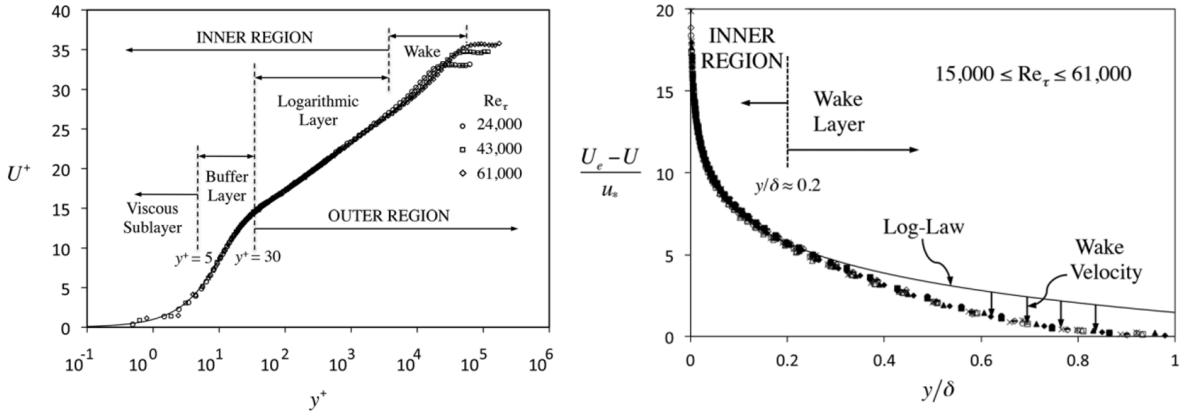

Figure 2.2: Non-dimensional velocity profiles for a ZPG TBL: (*left*) inner-scaled law of the wall and (*right*) outer-scaled defect law. From Perlin et al. 2016.

The overlap layer joins the inner and outer layers so the inner and outer laws (see equation 2.13) should smoothly join in this region. Functional analysis then dictates that the profile in this region should be logarithmic as given in both inner and outer variables in

$$u^+ = \frac{1}{\kappa}\ln y^+ + B \tag{2.14}$$

$$\frac{U_0 - U}{u_\tau} = -\frac{1}{\kappa}\ln\frac{y}{\delta} + A(\xi) \tag{2.15}$$

where the von Karman constant κ and the coefficient B have nearly universal values of 0.41 and 5 respectively, given by data correlations of Coles 1969.

Below the log layer, the region nearest the wall, commonly agreed to extend up to $y^+ = 5$, is the viscous sublayer. This region is completely dominated by viscous momentum transport and the velocity profile is linear as given by expression 2.16.

$$u^+ = y^+ \tag{2.16}$$

This is then smoothly joined to the log layer by the buffer sublayer. The inner layer is generally taken to extend up to $y/\delta = 0.1$ while the outer layer is taken to extend down to $y^+ = 30$ (Pope 2000). The overlap layer extends between these two values which makes it clear that its extent increases with the frictional Reynolds number δ/δ_ν.

To model the outer layer, Coles 1956 noted that from the perspective of the freestream the excess of velocity in the outer layer compared to the log layer has a nearly uniform wake-like form. This allows the entire velocity profile to be cast in the form

$$u^+ = f(y^+) + \frac{2\Pi}{\kappa} w\left(\frac{y}{\delta}\right) \tag{2.17}$$

where Π is the wake parameter, representing the wake strength, and w is the wake function encoding the deviation from the law of the wall which is zero at $y = 0$ and 1 at $y = \delta$. For the wake function $w =$ various values of Π this model is shown in figure 2.3. The actual form of the wake function and the wake strength then completely depend on the freestream. For equilibrium BLs, each wake strength corresponds to a single value of β.

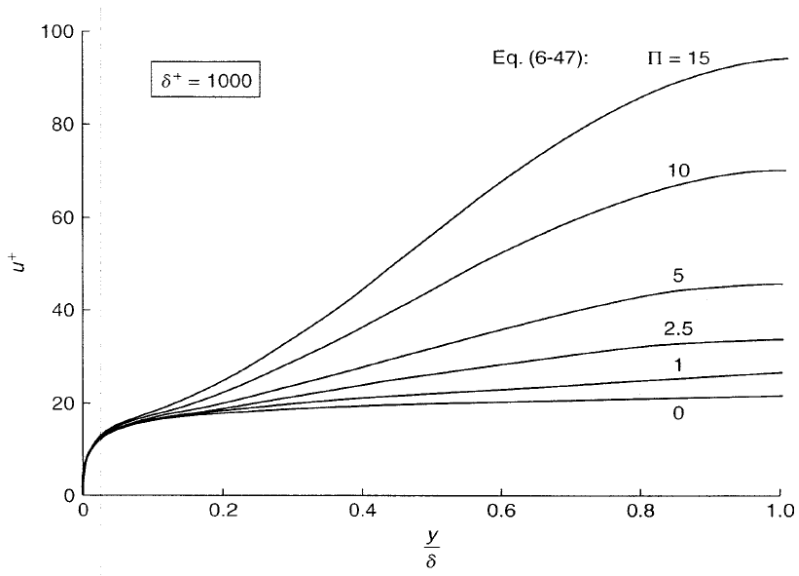

Figure 2.3: Coles' law of the wake for different values of the wake parameter Π and the wake function $w = 3\left(\frac{y}{\delta}\right)^2 - 2\left(\frac{y}{\delta}\right)^3$. From White 2006.

2.1.3. Structure of wall-bounded turbulence

The discussion so far focused on the time-averaged picture of the turbulent boundary layer, whereas now the attention is turned to the unsteady turbulent fluctuations. By way of Reynolds averaging, the instantaneous velocity u can be decomposed into a mean U and fluctuation component u' as

$$u_i = U_i + u_i' \tag{2.18}$$

The convective momentum transport due to turbulent eddies can therefore be posed as an additional Reynolds stress tensor $\langle u_i' u_j' \rangle$ while the kinetic energy contained in the fluctuations is termed turbulence kinetic energy (TKE) and defined as:

$$k = \frac{1}{2}\langle u_i' u_i' \rangle \tag{2.19}$$

The rate of change of TKE for a material volume of fluid is driven by production, dissipation, viscous diffusion, turbulent transport and pressure transport (Schlichting and Gersten 2016). The terms of the TKE transport, plotted in wall units, for a ZPG TBL are given in figure 2.4. It is clear that the highest specific turbulent activity is found in the near wall region. This so called inner peak of production is located at $y^+ \approx 12$ and it is larger than the dissipation at that location so the surplus is transported

away. Dissipation is highest at the wall where it's balanced by viscous diffusion and monotonically drops away from it. In the outer region up to $y/\delta \approx 0.4$ the production and diffusion terms are balanced and transport terms are negligible in comparison. Further out, the production drops to virtually zero, so dissipation is balanced by the various forms of transport (Pope 2000).

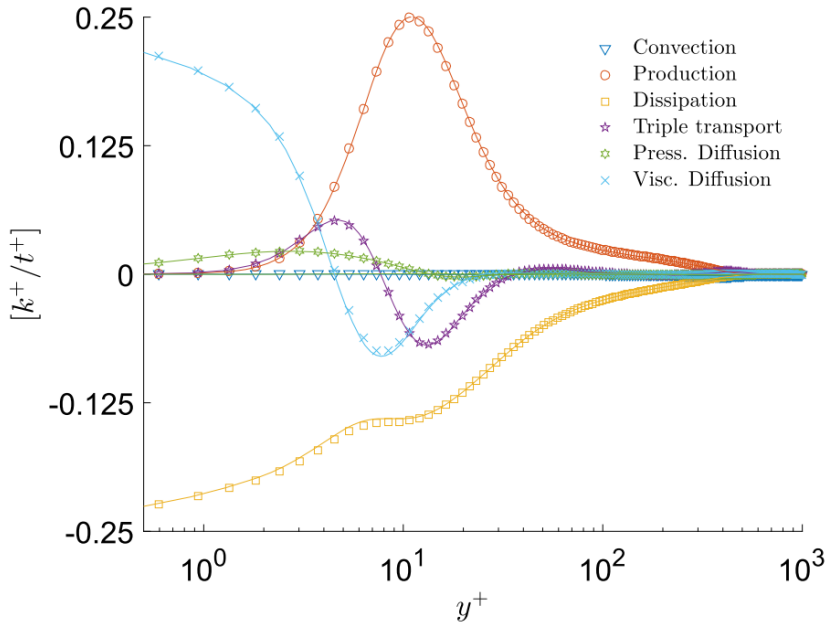

Figure 2.4: Turbulent kinetic energy budget plotted in wall units based on DNS data. Figure from Diaz-Daniel et al. 2017.

It could seem that the inner layer is by far the most dominant in turbulence production. However, this is only true at low Reynolds number flows which can be obscured by the logarithmic scale of the abscissa (Marusic et al. 2010). If the production term is premultiplied by the wall-normal coordinate, as shown in figure 2.5, a more representative image of the total content of TKE production is obtained. While the highest specific production is found in the near-wall region, at large Reynolds numbers and associated scale separation, the log layer is also much larger than the thin near wall region and in total a source of a significant proportion of turbulent energy production. Above a certain Reynolds number, even an outer peak of production appears.

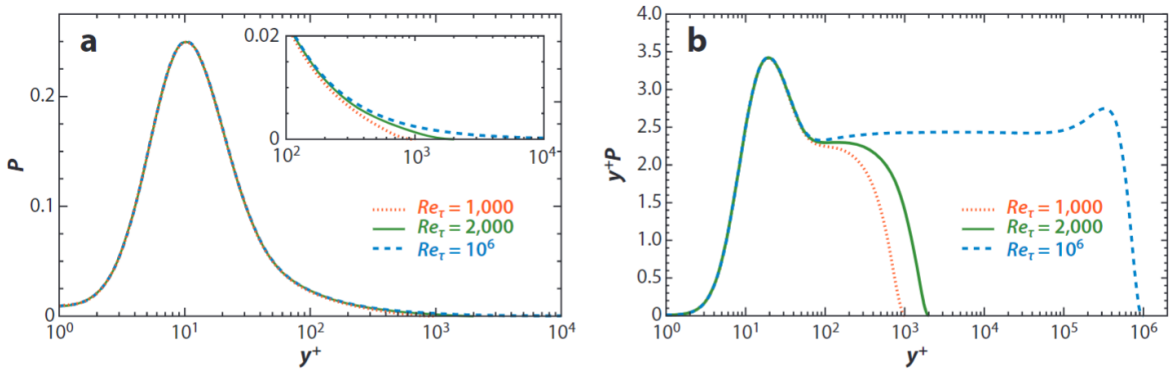

Figure 2.5: Premultiplied TKE production term for different Reynolds numbers indicating the total contribution of the larger outer scales. From Smits et al. 2011.

One of the principal approaches to studying the multiscaled turbulent flowfield is to identify elementary organized motions, termed coherent structures, the superposition of which reconstructs the flowfield. The predominant vortical elements of turbulent wall-bounded flows are hairpin-like vortices, packets of

hairpins and quasi-streamwise elongated hairpin legs (Adrian 2007; Smits et al. 2011; Wu and Moin 2009). These give rise to regions of low and high momentum which are sufficiently coherent in space and time to be noticeable as distinct features.

Aligned packets of hairpins are thought to induce large scale coherent motions (LSMs), also knows as superstructures, of low momentum fluid into the outer layer, as seen in figure 2.6. The spanwise wavelength of these structures is typically on the order of 0.3 to 0.5δ, while their streamwise coherence extends even up to 20δ according to Hutchins and Marusic 2007a. According to the authors even this might be an underestimation since the structures wander in the spanwise direction which would limit their streamwise extent measured by two point correlations. Large scale motions contain a significant amount of turbulent kinetic energy of the log region and are related to the outer peak in k that is observed with sufficient scale separation at higher Reynolds numbers. Even though the near-wall cycle was thought to be relatively autonomous and independent of these motions, it has been shown by Hutchins and Marusic 2007b that these findings stemmed from investigations limited to lower Reynolds numbers flows. In fact, in high Reynolds number flows, the superstructures are shown to significantly modulate the near-wall cycle.

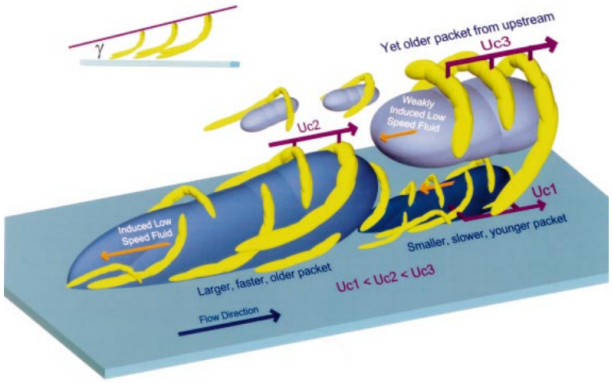

Figure 2.6: Structural model of hairpin packets and induced uniform low momentum zones by Adrian et al. 2000.

Lee 2017 investigated by way of DNS how these structures are affected by adverse pressure gradients and found that mild APGs actually increase coherent alignment of hairpin vortex packets in the streamwise direction thus increasing the streamwise length scale. However, with an increase in APG the formation of these packets is suppressed which lessens the streamwise scale of the structures. Their spanwise wavelength meanwhile increases in the log layer and decreases in the outer layer tending towards a relatively uniform scale of 0.5δ across the boundary layer.

The presence of coherent structures in the flow implies certain modes of perturbation to which the flow is most receptive. For example, Cossu et al. 2009 performed a linear stability analysis of the mean flowfield of a ZPG TBL. They determined 2 distinct peaks, an inner and an outer, in the spanwise wavelength of the maximally amplified perturbations. The inner corresponds perfectly to the well known buffer layer streaks, which have the most well defined scale of all the TBL structure. For the outer peak it is less clear but there is tentative evidence of correlation with the supestructures of Hutchins and Marusic 2007b. Therefore choosing, sizing and operating actuators such that naturally occuring structures in the flow are imitated, stands to produce the strongest effect for the lowest expenditure of energy.

2.1.4. Flow detachment

For a two-dimensional and steady turbulent separating flow in the time-averaged sense, the separation region is neither steady nor two-dimensional. For smooth surfaces, separation begins intermittently both in time and spanwise direction, with reverse flow happening only a fraction of time at a given spanwise location, which increases downstream. The same is true of reattachment if it happens. Simpson et al. 1981 proposed a quantitative classification of different regions of a separated region based on the backflow parameter χ which represents the proportion of time for which the flow moves upstream. These are

- incipient detachment (ID) - $\chi = 0.01$,
- intermittent transitory detachment (ITD) - $\chi = 0.2$,
- transitory detachment (TD) - $\chi = 0.5$,
- detachment (D) - this is the location where the mean local wall shear is zero $\tau_w = 0$.

From available data it is clear that $\tau_w = 0$ occurs when the local backflow parameter is 50%, therefore TD and D are located at the same point. For a reattaching flow, this same classification is used but with reattachment (R) instead of detachment.

Figure 2.7 shows a mean streamwise velocity field of a turbulent separation bubble generated on a flat surface by Mohammed-Taifour and Weiss 2021. The white solid line denotes the contour line $U = 0$ which encloses the *backflow region* in which the mean velocity is negative. This line also by definition corresponds to the contour line of $\chi = 0.5$ so where it meets the wall we find denoted the points of transient detachment and transient reattachment. Upstream of intermittent detachment and downstream of complete reattachment the flow is effectively always downstream and outside of the overall separation region.

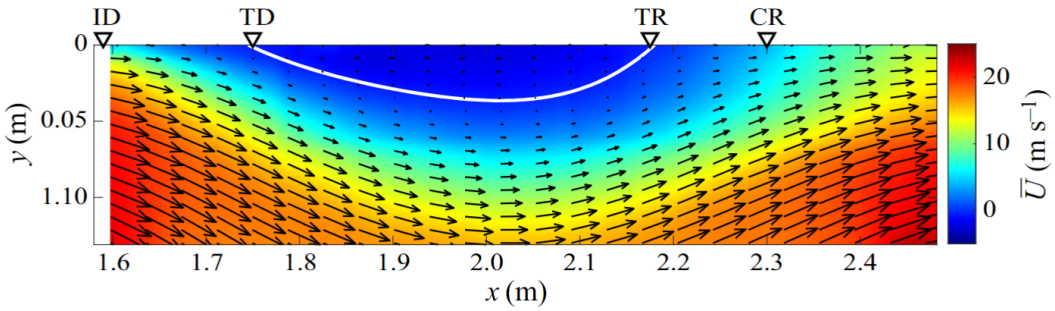

Figure 2.7: Mean streamwise velocity field showing a turbulent separation bubble generated on a flat surface using opposite wall suction and blowing. White line represents the contour line $U = 0$. From Mohammed-Taifour and Weiss 2021.

Flow reversal begins at the wall ($y \to 0$) when the rate of transport of streamwise momentum towards the wall is smaller than the rate of deceleration caused by an imposed APG. This leads to the formation of a separation surface, a sudden increase in the displacement thickness and consequently APG relief (see figure 2.8). For engineering purposes it is of interest to be able to predict where separation will begin. There have been many attempts, analytical, numerical and experimental, to try to define separation criteria based on the state of the boundary layer, usually through the shape factor which represents how concentrated streamwise momentum is near the wall. Castillo et al. 2004 analytically consider an equilibrium TBL with vanishing wall shear and therefore at the point of separation and determine a shape factor of $H_{sep} = 2.73$. This can be understood as a theoretical maximum H_sep. On the other hand, experimental data collected by Cebeci and Bradshaw 1977 indicates that H_{sep} is in the range of $1.8 - 2.4$ with the reduction in H_{sep} compared to the theoretical value being a result of other parameters such as wall rougness and curvature.

One can identify two contributing factors to the APG experienced by the near wall flow. One is the external flow, "global" pressure gradient. The other, "local" pressure gradient, stems from streamwise curvature of the wall (Simpson 1996). In the case of convex wall curvature, a local bubble of low pressure is generated, which is a purely inviscid effect. The incoming boundary layer therefore first experiences a favourable pressure gradient and then an inevitable pressure recovery. In this local pressure recovery region, the boundary layer now experiences a higher APG then one would if they were measuring away from the wall. The extreme case of this is a geometric aberration like a sharp corner. Possessing infinite curvature, such a sharp edge would in the inviscid case yield a singularity with an infinite flow velocity and APG. In reality, due to viscosity and a finite total pressure, the flow cannot take such a sharp corner and simply departs the surface tangentially.

Another factor to consider with regards to wall curvature is that even in the absence of a global pressure gradient such as in a curved duct it affects the turbulent entrainment of the BL fluid by the freestream. In case of convex streamline curvature, there is a pressure gradient normal to the wall

$\partial p/\partial n > 0$ which reduces this entrainment thus inhibiting momentum transfer. Both of these effects lead to separation beginning earlier than would otherwise happen if there was no surface curvature.

A separation occuring in a flat 2D diffuser is an example of a purely global APG driven separation, while the canonical geometry-induced separated flow is the already mentioned flow over a backward facing step as seen in figure 2.8. For general cases, both effects are involved to varying degrees. The focus of this project is on separation from smoothly contoured surfaces. It is reasoned that this is more relevant to conventional aerospace applications, as flow separation on airfoils, diffusers, etc. is primarily caused by an APG with mild convex curvature present. The study of geometry-induced separation is more relevant to separation on bluff bodies for example. With respect to flow control, this choice is important because for APG induced separation the focus is generally on *separation delay*, while for geometry-induced separation this is impossible and the focus is rather on *wake-shaping*, an example of which is given in Barros et al. 2016.

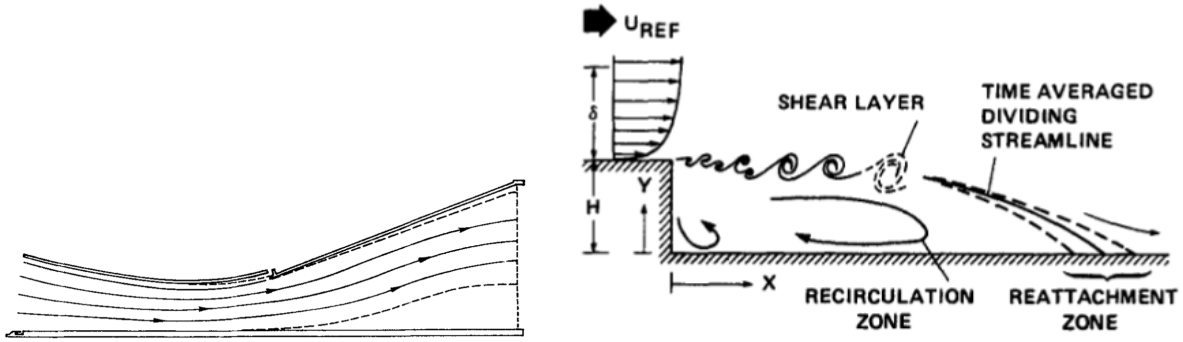

(a) **(b)**

Figure 2.8: Illustrations of: (a) Pure pressure-induced separation on a flat plate by a contoured opposite wall from Simpson et al. 1977, (b) Pure geometry-induced separation from Simpson 1996.

Based on the data reviewed by Simpson 1996, for curvature parameters $\delta/R < 0.05$ the point of detachment agrees well with data obtained on flat walls. On the other hand, for $\delta/R > 0.1$, detachment begins at lower shape factors than predictions based on flat wall data would suggest. The effect however seems to grow slowly. For example, for a single experiment with $\delta/R = 0.13$, at the point where the ITD ($\chi = 0.2$) is predicted, the backflow parameter is actually measured to be $\chi = 0.3$. This seems to indicate, at least for this limited data set, that the impact of curvature on the extent of the separation region gradually increases rather than behaving like a sudden switch.

2.1.5. Flow reattachment

As a boundary layer departs the surfaces, the point of highest shear is no longer at the wall and the mean velocity profiles away from the wall resemble the profiles of plane free shear layers. The differences with respect to this class of flows are that the fluid of the "low speed stream" is actually highly turbulent, that the presence of the wall affects the development of the shear layer and furthermore that this shear layer curves. The greatest similarity is observed in the early part of shear layer development in the case of a sudden geometry-induced separation of the backward-facing step because in this case the effect of the wall is minimal.

During development, the shear layer spreads as it entrains low speed fluid from the recirculation zone. Eventually, if the surface is still present, the flow will reattach. As a thought experiment, Greenblatt and Wygnanski 2000 consider a sharp edged flap shown in figure 2.9. The flap is initially undeflected and then is suddenly deflected. If the mass entrained by the separated spreading shear layer, represented by $\delta(x)$ is greater than the mass available for entrainment the flow will reattach. Otherwise, to satisfy continuity requirements, there is a recirculation region in the mean flowfield which artificially reduces the mass available for reentrainment.

Clearly, a sudden increase in spreading rate can cause reattachment, which is an important observation for flow control implications. This is how laminar separation bubbles are formed. The separated laminar shear layer becomes unstable and transitions which leads to a rapid increase in spreading rate on account

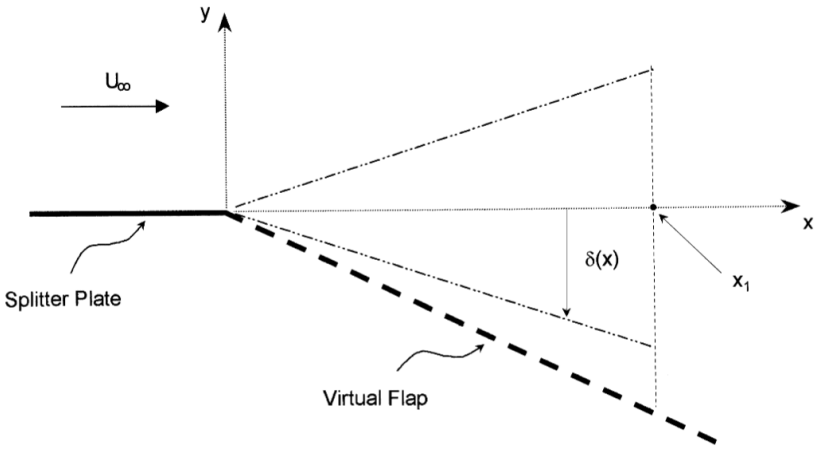

Figure 2.9: An illusration of the spreading a separation shear layer above a deflected flap. From Greenblatt and Wygnanski 2000.

of the added turbulent shear stress. This leads to the flow reattaching (O'Meara and Mueller 1987).

2.1.6. Dynamics of a turbulent separation bubble

Until now, the discussion of turbulent separation regions has been focused on the time-averaged description of the flowfield. However, as already noted, turbulent separation bubbles are highly unsteady. Modal and spectral analysis of this unsteady flowfield reveals a broadband unsteadiness due to turbulence of the incoming boundary layer and more coherent modes generated by the development of the shear layer. The coherent modes related to the shear layer development are, in order of decreasing characteristic frequency, the shear layer instability, the vortex shedding mode and the breathing or flapping mode.

The first two are related to the same Kelvin-Helmholtz instability mechanism observed in free shear layers, which have been reviewed by Ho and Huerre 1984. To elaborate, consider that an infinite flat sheet of spanwise vorticity not contrained by a wall is unstable because as soon as a streamwise velocity perturbation ("waviness") is introduced, the self induction of the sheet tends to roll it up into discrete vortices. The most amplified wavelength of the perturbation is the one which causes the fastest roll-up and will ultimately end up being equal to the characteristic wavelength of the velocity field. This array of vortices is again unstable with the most amplified perturbation being a first subharmonic with double the wavelength. This *subharmonic resonance* is easily understood by imagining that every odd vortex is raised and every even vortex lowered by a distance ϵ. The mutual induction leads to the pairing and subsequent merging of neighboring vortices faster than any other wavelength of perturbation would. This process would then repeat slower and slower with the wavelength of the velocity field increasing in step.

The flow in the described case is temporally evolving, as perturbation amplitudes increase in time but are constant in space. However, in the actual case of shear layers formed at separation, the flow is *spatially evolving* with the amplitude growing in space but constant in time. The most amplified frequency in the shear layer just after separation is that of the shear layer instability mode. Then through a series of vortex mergings, the spanwise structures grow to the lengthscale of the separation region, be it a bubble or the wake of a body. The characteristic frequency of the unsteadiness drops through this development to the ultimate vortex shedding frequency. Such a spatial development of a plane free shear (mixing) layer is shown in figure 2.10 where the appearance of small-scales in turbulent transition is also apparent.

Sigurdson 1995 notes that the initial shear layer Kelvin-Helmholtz instability is purely driven by the interaction of the spanwise vorticity with itself. This suggests the use of the same scaling based on momentum thickness for the frequency as that used for free mixing layers $St_\theta = f\theta_0/U_e$. Once the structures grow enough to start interacting with the wall, the Kelvin-Helmholtz instability is modified and, according to Sigurdson 1995, it is closer to the bluff body vortex shedding mode or to the preferred mode of jets, both of which are constrained geometrically. This is based on the fact that for a variety

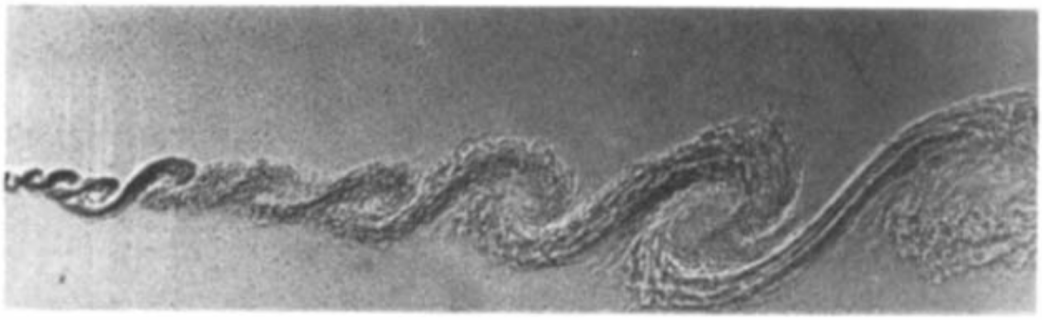

Figure 2.10: Large coherent structure development in a plane mixing layer with subsequent transition to small scales. From Brown and Roshko 1974.

of geometries, the proper scaling is found to be that based on the height of the separation bubble and the velocity at the edge of the boundary layer at the point of separation U_s giving a Strouhal number $St_h = fh/U_s$, which is analogous to the scaling of the bluff body shedding on the length scale of the body which is also the initial width of the wake.

Vortex shedding

A valid question to ask is whether this discussion of large coherent spanwise roller vortices (LCS) emerging in free shear layers by hydrodynamic instability mechanisms is at all applicable to high Reynolds number fully turbulent separating shear layers. Large coherent structures are indeed generated in plane mixing layers with turbulent initial conditions and have been observed up to Reynolds numbers of 10^7, where Re is based on the mean shear layer velocity and the initial momentum thickness (Brown and Roshko 1974; Dimotakis and Brown 1976). In fully turbulent flows the large coherent spanwise structures are fuzzy and coexist with fine scales of motion, but can still be identified through modal/spectral analysis by the energy they carry. Furthermore, due to self-induction effects they themselves tend to quickly warp and lose their spanwise shape.

Secondly, there is the question of the similarity of the dynamics of the separating shear layer and free mixing layer. Various studies have shown that the separated shear layer is similar to a turbulent plane mixing layer in terms of scaling of the mean velocity profiles and turbulent statistics, appearance of large coherent spanwise structures, spreading rate and characteristic spatio-temporal scales. This was shown both for geometry induced separations such as backward facing steps and blunt faced cylinders (Debien et al. 2015; Kiya et al. 1997; Sigurdson 1995) as well as the opposite case of APG driven separations on flat walls (Mohammed-Taifour and Weiss 2016; Wu et al. 2019).

To illustrate this, Wu et al. 2019 studied a turbulent separation bubble generated on a flat plate by an imposed APG by way of DNS. It has to be noted however that this being a DNS simulation, the Reynolds number was relatively low at $Re_\theta = 490$. Using dynamic mode decomposition and two-point correlations of the streamwise velocity fluctuations in the streamwise (xy) plane, the authors note the appearance and downstream growth of spanwise vortical structures in the shear layer as seen in figure 2.11. They even observe a very sudden growth around $x = 450\theta_0$ with an associated drop in prefered frequency which they postulate to be a merging event.

These large coherent structures supply the backflow of the "recirculation" region, which only contains recirculating fluid in the time-averaged image of the flow. The backflow region is in fact extremely unsteady with velocity fluctuations on the order of the mean backflow velocity, precisely because it is generated by relatively discrete structures which are convected with the shear layer (Simpson 1996). The separation bubble therefore fluctuates both in size and position. The shear layer grows not only through mergings of the LCS but also through the entrainment of neighbouring fluid.

Initial shear layer instability

The appearance of the initial shear layer instability and its prefered frequency can be studied using linear stability theory which is based on assumptions of laminar parallel 2D flow and a known baseflow velocity profile. The prefered frequency scales with the mean velocity of the shear layer $\bar{U}$, which for a shear layer originating from a single boundary layer can be replaced with U_e, and its initial momentum

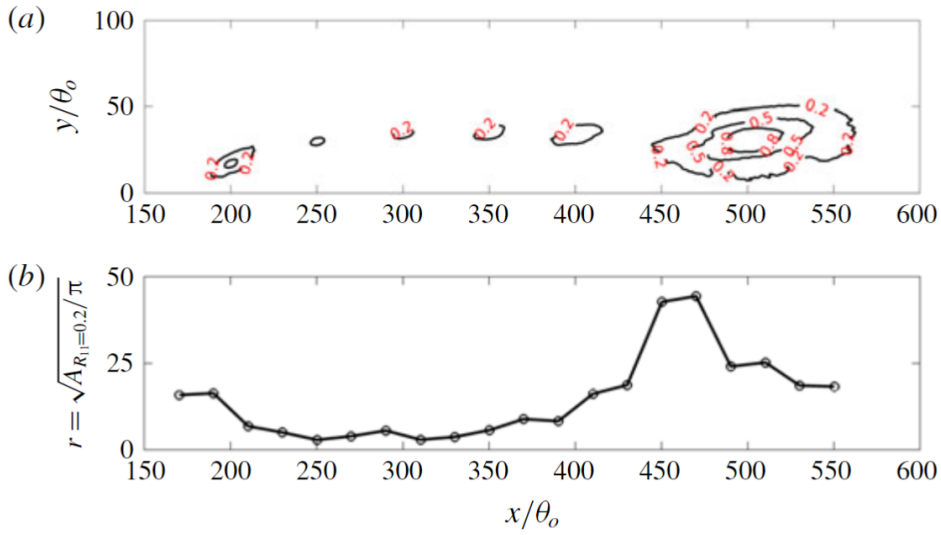

Figure 2.11: (a) Two-point correlation coefficient contours of streamwise velocity fluctuations. (b) Development of radius of roller vortex determined from $R_{11} = 0.2$ contour line. From Wu et al. 2019.

thickness θ_0 yielding the Strouhal number $St_\theta = f\theta_0/U_e$. Linear stability theory predicts this result to be $St_\theta = 0.016$ (Monkewitz 1982). As has already been noted, in turbulent separating shear layers these assumptions are never realized. However, Ho and Huerre 1984 states that the development of these structures for a turbulent flow can still be understood as hydrodynamic instability waves "propagating on the pseudolaminar flow of the time-averaged velocity field", provided that the scale separation of the turbulent fluctuations and the large scale instability is sufficient.

For cases of turbulent separation from sharp edges where the line of detachment is fixed, the shear layer instability mode *is* often detected in the region near separation. However, its St_θ varies and is generally different to the theoretically predicted value as seen in the four studies presented in table 2.1.

Study	Geometry	Re_θ of separating BL	St_θ of SLIM
Hasan and Khan 1992	BFS	904	0.011
Eaton 1980	BFS	850	0.015
Debien et al. 2014	BFR	3628	0.014
Brunn and Nitsche 2006	BFR	2210	0.021

Table 2.1: Sample of shear layer instability frequencies measured in geometry-induced separation studies. BFS: backward facing step, BFR: backward facing ramp.

Morris and Foss 2003 shed some light on this. They studied the near separation region of a backward facing step flow with a relatively large Reynolds number incoming boundary layer ($Re_\theta = 4650$). They find that only some fraction nearest to the wall of the boundary layer vorticity actually takes part in the initial inflectional instability which they term the *sub-shear layer*, as seen in figure 2.12. The physical explanation they give for this is that in a turbulent boundary layer the mean shear is much more concentrated closer to the wall with the outer velocity profiles relatively "flat". If the momentum thickness of this sub-shear layer and the velocity at its outer edge (effective U_e) are used for scaling, the frequency corresponds well to theoretical predictions and laminar results $St_\theta = 0.016$.

For turbulent separations off of smooth surfaces the line of detachment fluctuates across the span due to the turbulence of the separating boundary layer. This makes the identification of the initial shear layer instability difficult and its importance for separation control purposes less clear. Generally, studies concerned with such separation like the flat plate separations mentioned above, do not seem to detect or are at least not focused on any measurable spectral peaks corresponding to this instability (Mohammed-Taifour and Weiss 2016). The studies of Zhang and Zhong 2011 and Lardeau and Leschziner 2011, focused on curved ramps, do mention this mode but do not directly measure it.

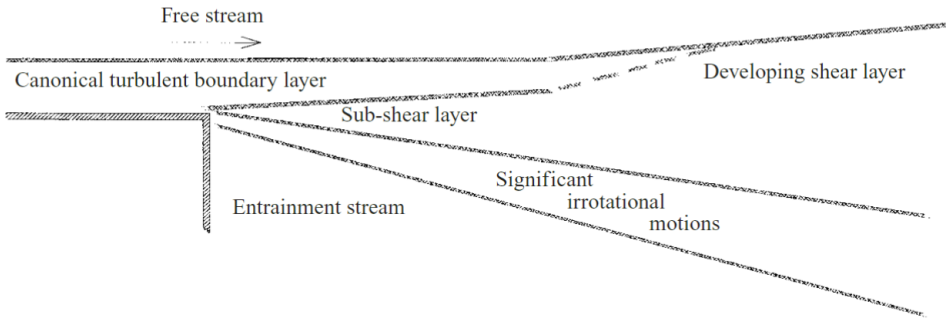

Figure 2.12: Illustration of the concept of the sub-shear layer developing in a backward facing step separation. From Morris and Foss 2003.

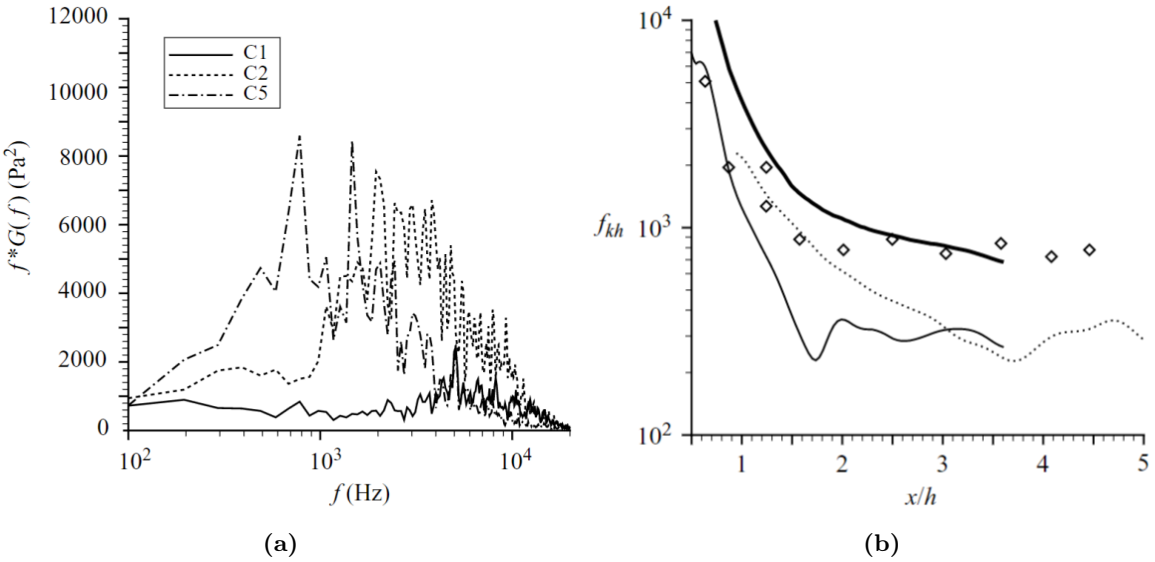

Figure 2.13: (a) Pressure fluctuation spectra at 3 different points in the shear layer. Points C1 and C2 are the first two points chosen in the shear layer. (b) Streamwise evolution of the most amplified frequency of the shear layer. Markers: spectral peaks from simulation data; thick solid line: approximate value from a two-dimensional free shear layer; Thin solid line: linear stability analysis of unforced flow; Dotted line: linear stability analysis of flow force at high frequency. From Dandois et al. 2007.

The LES study of Dandois et al. 2007 of a turbulent flow separating off a curved backward facing ramp is a unique example of a detailed analysis of this mode for such a case, although with a relatively low $Re_\theta = 1410$. Figure 2.13 shows their results. In the first two points in the shear layer where they took spectra (C1 and C2), the spectral peaks correspond really well to a linear stability analysis based on the incompressible Rayleigh equation (thin solid line). Further downstream, the linear analysis falls short because the instability mechanisms of discrete vortices are non-linear, but good agreement is seen with the data of free plane shear layers (thick solid line). Even so, the spectra for points C1 and C2 clearly show a large amount of broadband turbulent fluctuations which disguise the peak. It is likely that the larger the region of intermittent separation, the more obscured any coherent shear layer instability will be by the turbulent fluctuations. The same can be said of an increase in Reynolds number.

Breathing

Finally, a low frequency unsteady breathing mode is sometimes observed in turbulent separation bubbles. An analogue of this mode cannot be found in plane shear layers as its invariably connected to the nature of the closed separation bubble itself. The characteristic timescale of this motion is generally much higher than for the other motions discussed and it appears as a shrinkage and enlargement of the entire

bubble.

The mechanism behind this one is still debated. Generally, the proposed mechanisms can be split into two streams of thought:

- feedback mechanism
- feedforward mechanism

The feedback mechanism is generally supported by studies of geometries with fixed separations and wandering reattachments such as backward facing steps. This view holds that perturbations originating at the reattachment propagate upstream affecting the separation bubble as a whole. For example, one proposed mechanism is that there is an instantaneous imbalance between the mass of fluid entrained from the recirculation zone and that reinjected near the point of reattachment which leads to a fluctuation of the overall size of the separation bubble. This mechanism has been supported by Durst and Tropea 1983.

In contrast, the feedforward mechanism has been proposed by those studying global pressure gradient induced separations where there is an extra degree of freedom in the form of the wandering of the detachment line. The already mentioned studies of Mohammed-Taifour and Weiss 2016 and Wu et al. 2019 as well as their follow-ups in which forcing was applied (Mohammed-Taifour and Weiss 2021; Wu et al. 2022) had as their primary objectives precisely to study this low frequency unsteadiness.

Mohammed-Taifour and Weiss 2021 proposed that the low frequency breathing is a "response of the TSB to upstream turbulent perturbations". They found that the TSB acts as a low pass filter which converts the broadband fluctuations present in the incoming boundary layer into a large-scale contraction and expansion of the bubble. The upstream turbulent fluctuations affect the point of separation which affects the global pressure and velocity field leading to a downstream effect on the point of reattachment as well.

Wu et al. 2019 meanwhile note, after performing DMD of their DNS dataset, that the mode related to the low frequency motion is related to elongated streamwise structures which extend all the way from the separation region across the bubble to downstream of reattachment. They determine that the concave curvature of streamlines caused by the detachment of the boundary layer is enough to generate counter-rotating streamwise Goertler vortices of scale δ through a centrifugal instability mechanism. They presume that the periodic breakdown of these structures downstream modulates a merging of the shear layer vortices which are then shed downstream as a large packet of vorticity which leads to a temporary increase in the size of the backflow region.

2.2. Separation control using jet actuators

The following section provides a review of active separation control using jet actuators. Useful reviews dealing with this topic are the work of Gad-el-Hak and Bushnell 1991 who provide an overview of the entire separation control field, Greenblatt and Wygnanski 2000 who focus on oscillatory control and Choi et al. 2008 who discuss the application to the control of flow around bluff bodies. Meanwhile, a review of general jet-crossflow interactions with a lot of information important for the design of separation control systems is given by Mahesh 2013.

While this project is concerned with non-zero mass flux jets, a lot of the reviewed literature utilizes synthetic jets. These are cavities, periodically driven by an energy source (a piezo-electric diaphragm, plasma heater, etc.) such that they alternately ingest and expel the surrounding fluid. When the operating conditions are right, there is a net transfer of momentum to the fluid even with zero net mass flux, generating a train of vortical structures which in turn produce a jet formed of the surrounding fluid. Comprehensive reviews are given by Glezer and Amitay 2002 and Glezer 2011. Despite the differences in implementation between zero and non-zero mass flux jets, it is argued that conclusions gleaned in separation control applications are quite interchangeable, because in the farfield the effect of both actuators can be reduced to a momentum source. Furthermore, the higher the unsteadiness of actuation the more similar the actuators become even in the near field.

2.2.1. Fundamental principles

Fundamentally, separation control involves replenishing momentum in the near wall region which has been lost to friction such that separation is either minimized or completely eliminated in the APG imposed by pressure recovery. The simplest strategy to achieve this is to either directly blow tangentially to the wall, adding the lost momentum, or to use suction to remove the low momentum fluid near the wall. These concepts have been around as long as the concept of the boundary layer but many other more efficient methods have been proposed.

For any desirable system the goal is for the energy saved by control to outweigh the energy expended as much as possible. For a case of direct momentum addition such as blowing it's clear from a first principles consideration that this is always bound to just break even. Consider a bluff body with a wake behind it. The total pressure deficit in the wake is equal to the drag generated on the body. If we use a perfect control system with no internal losses to replenish the lost momentum of the entire wake, we have completely eliminated the drag of the body, but to do that we have also had to add the same amount of momentum. The efficiency from a flow control system standpoint is therefore zero as no net saving has been achieved. To achieve efficient separation control, the important realization is that momentum in the flow is abundant, but simply not near the wall. So the goal of most separation control systems is to efficiently redirect this momentum towards the wall, such that the potential for pressure recovery is increased.

There are two mechanisms which a successful jet-actuated separation control system aims to exploit (Gad-el-Hak and Bushnell 1991). The first is direct momentum transfer induced by flow structures generated by the actuators. A jet is fundamentally a *momentum source of finite extent* and the jet-crossflow interaction is driven by the competition between their respective momenta. A fundamental jet parameter is therefore the momentum ratio

$$c_\mu = \frac{\rho_j U_j^2}{\rho_\infty U_\infty^2} \tag{2.20}$$

When the crossflow and the jet fluid are the same and the velocities are small enough to ignore changes in density, this momentum ratio reduces to the velocity ratio

$$VR = \frac{U_j}{U_\infty} \tag{2.21}$$

For purposes of separation control system evaluation, it is not simply enough to compare the differential momenta of jet and crossflow but also their integral values. For this reason most authors define the C_μ as the ratio of the total jet momentum flux and some crossflow momentum flux using a reference dimension.

$$C_\mu = \frac{\rho_j U_j^2 A_j}{\rho_\infty U_\infty^2 A_{ref}} \tag{2.22}$$

Based on the reasoning of flow control efficiency and its relation to the momentum deficit of the boundary layer given above, it is this author's opinion that the best reference crossflow momentum is precisely the momentum flux deficit between the viscous and equivalent inviscid flows. The "ideal" tangential blowing would therefore have a $C_\mu = 1$ and its result would be a flow locally equivalent to the EIF.

Because the edges of a jet source represent discontinuities in momentum, jets are also *sources of vorticity*. This vorticity rolls up into vortical structures which can carry a significant amount of energy and persist far downstream. They induce swirling motions in the boundary layer, producing artifical ejection and sweep events, lifting low momentum fluid away from the wall and bringing higher momentum fluid towards the wall. Besides changing the operating parameters such as the amplitude and time-profile of momentum addition, the jet-crossflow interaction is most effectively tailored by changing the shape and direction of the momentum source. This ultimately controls the nature and downstream trajectory and development of the vortical structures produced by the interaction. The fundamental distinction here is made between two-dimensional semi-infinite jets and finite three-dimensional jets which produce a much more complex interaction flowfield. The fundamental aspects of the interaction flowfields and how they apply to separation control are discussed in sections 2.2.3 and 2.2.4.

The other separation control mechanism of note is the excitation of natural flow instabilities to amplify the control input. First and foremost this entails turbulence amplification. An obvious example and a "zeroth order effect" for this is promoting laminar to turbulent transition which massively increases momentum transfer through the boundary layer and delays separation or promotes reattachment as in the case of laminar separation bubbles. If the separating boundary layer is already turbulent, transition is no longer an available control strategy but the possibility of optimal actuation being related to the natural scales of the TBL remains.

On top of that, shear flows exhibit other instabilities which can be targeted. Chief of these is the inviscid Kelvin-Helmholtz (KH) instability of a separated shear layer. The similarity between separated single-stream turbulent shear layers and plane mixing layers has already been noted in the section on turbulent separation. This similarity is here extended to excited shear layers (Greenblatt and Wygnanski 2000). Even very low amplitude excitation at the right frequencies can significantly affect the development of a shear layer, modifying the rate of entrainment (Oster et al. 1978). It is clear how in the case of a separation bubble this could affect its extent. This phenomenon is marked by a pronounced frequency sensitivity and the optimal excitation frequency usually is the focus of time-periodic excitation separation control studies. This is discussed at length in section 2.2.2. Furthermore, in separations with sufficient concave streamline curvature the Goertler instability mechanism can be quite significant in modulating the flowfield and thus promising for exploitation in separation control systems.

Both of these principles, direct momentum transfer and instability excitation, are in action in every flowfield perturbed by a jet and are heavily coupled. The spatio-temporal nature of the actuated flowfield drives the development of instability and in turn the latter affects the former. For example, it is often argued that 2D actuators have the most potential to induce large effects in the flow (Leschziner and Lardeau 2011), firstly because the entire span is actuated and secondly due to Squire's Theorem. This states that a two-dimensional (2D) flow is most unstable to a two-dimensional perturbation (Squire 1933). Squire analytically determined this in the context of laminar to turbulent transition, obtaining smaller disturbance growth rates for three-dimensional (3D) perturbations. This indirectly implies that in the context of 2D or quasi-2D flow separation control, if aiming to excite the 2D KH instability, a 2D actuator stands to be the most effective. This is indeed one of the reasons why most 2D separation control studies focused on unsteady actuation and instability excitation have tended to use 2D actuators.

However it is a common finding in all cases where 2D and 3D actuation (with jets and other actuators) approaches are directly compared, that 3D actuation performs better, either by achieving the same effect with less input momentum or by achieving an improved effect with the same input. For examples the reader is refered to the studies of Seifert et al. 1998, Aram and Mittal 2011 and Kim et al. 2012 who find that the flowfield induced by a spanwise varying perturbation, marked by streamwise vortices, looks to be more effective at replenishing fluid momentum in the near wall region compared to a completely 2D perturbation.

The question remains of whether or not the 3D perturbations in these cases are utilizing the benefits of resonance with the 2D shear layer instability to the same extent as the 2D actuators. To properly study this, a direct comparison of the amplification rates should be made and at that point it's unclear whether or not this is even important if the same effect is achieved with a different mechanism. However, answers to these question could potentially allow even more effective 3D actuation methods to be

designed which is something that is considered in this work in the form of an alternating 3D actuator.

The other important thing to note is that many unsteady actuation studies focus on flows separating from sharp edges. Based on the observations of Vukasinovic et al. 2005 it seems that in these cases, a receptivity mechanism based on the Kutta condition at the sharp edge triggers the shedding of large spanwise vortices, essentially wake vortices, upon onset and termination of control irrespective of the control topology. Due to the topological similarity of these shed structures to the shear layer structures, it's clear how this could strengthen the coupling of control and the 2D shear layer instability.

Further proving this point, Debien et al. 2015 explicitly note that large spanwise structures are created in their sharp backward facing ramp experiments even though a completely 3D control system is utilized, indicating the excitation of the separated shear layer. It is unlikely that this would be observed to the same extent in cases of separation from smoothly curved walls, as the freely moving detachment line would greatly reduce the spanwise flow coherence, especially in the case of a 3D actuation. In their numerical investigation of a curved backward facing ramp separation, Lardeau and Leschziner 2011 express doubt about the ability of 3D actuators to excite the 2D shear layer modes.

2.2.2. Shear layer instability modulation

Based on the notion of two fundamental modes (instabilities) driving a turbulent separation bubble, namely the Kelvin-Helmholtz shear layer instability mode with frequency f_{SLI} and the vortex shedding mode with frequency f_{VS}, Sigurdson 1995 notes four different regimes of forcing depending on forcing frequency f_f:

1. $f_f >> f_{SLI}$
2. $f_{SLI} \geq f_f >> f_{VS}$
3. $f_f \approx f_{VS}$
4. $f_{VS} >> f_f$

This assumes that the scale separation of the separating boundary layer θ_0 and the extent of the separation h is sufficient such that $f_{SLI} > f_{VS}$. Forcing at frequencies between f_{VS} and f_{SLI} is amplified by the shear layer, as this range of frequencies coincides with the variation of the most amplified frequency during the development of the separated shear layer until reattachment (Greenblatt and Wygnanski 2000).

To illustrate, attention is again turned to the similarity between free mixing layers and a separated shear layer. Figure 2.14 shows a flow visualization of a plane free shear layer excited at the initial most amplified frequncy and its first subharmonic (half the frequency) acquired by Oster et al. 1978. It is clear that forcing at the initial shear layer instability frequency leads to a much faster formation of the large scale vortices the size of which is then stabilized by the excitation. Excitation at half the frequency meanwhile leads perhaps initially to a slower development but then the structures suddenly grow to a size that wasn't achieved in the other case. In this case, the subharmonic resonance is excited, which accelerates the merging of the initial structures leading immediately to an appearance of larger structures without an intermediate step. For cases of even lower excitation frequency, Ho and Huerre 1984 notes the phenomenon of *collective interaction* in which multiple initial structures can be force to interact and merge leading to a very sudden increase in structure size. For cases of turbulent separation bubbles in which the VS frequency is much smaller than the KH frequency and the bubble is forced at the VS frequency it is likely that this phenomenon is at play.

In general, separation control studies tend to find the optimum frequencies of actuation somewhere in the range of what the shear layer can amplify which leads to the conclusion that coupling of the actuation with the shear layer dynamics is what drives the optimum. This isn't however entirely clear for all geometries as will be shown below. For *geometry-induced separations* this tends to give St_h in the range between 0.2 and 0.4 (Bhattacharjee et al. 1986; Brunn and Nitsche 2006; Kiya et al. 1997; Sigurdson 1995). An example of drag reduction for a blunt-faced cylinder with leading edge separation is shown in figure 2.15. The shedding frequencies of these flows generally tend to be clustered around $St_h \approx 0.08$ and $St_h \approx 0.2$. Sigurdson 1995 notes that these flows tend to exhibit a vortex merging event close to the reattachment location which could be an explanation for these two clusters of data, the former corresponding to flows with a final merging event and the latter corresponding to flows without it. In any case, for flows with a merging event, the optimum frequencies remain the same, in which case Sigurdson 1995 points out that the forcing frequency should be at least above the first harmonic of the ultimate, post-merging shedding frequency.

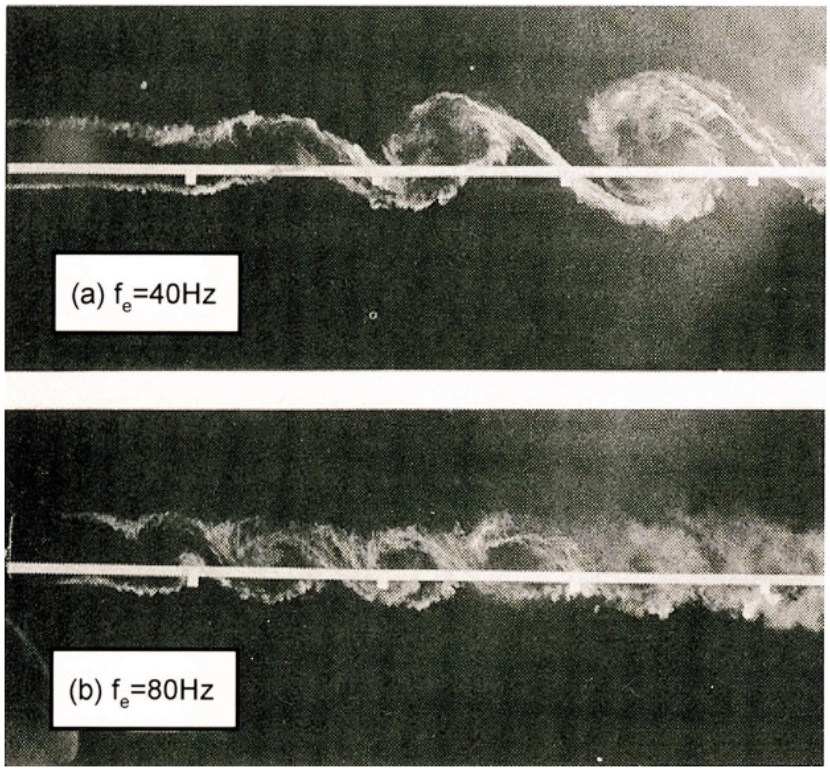

Figure 2.14: Plane free shear layer excited at (a) the initial shear layer instability frequency (80 Hz) and (b) at the first subharmonic (40 Hz). From Oster et al. 1978.

The range of "optimal" frequencies is dictated by the trade-off between the control effect amplification and dissipation. Lower frequencies closer to f_{VS} tend to accelerate the growth of large scale vortices through amalgamations of initial roll-ups. Higher frequencies however are amplified earlier in the shear layer development which could be the reason that in some cases these show better performance, leading presumably to earlier increased entrainment (Sigurdson 1995). Secondly, higher frequency perturbations dissipate more quickly which could ultimately limit the extent of control (Greenblatt and Wygnanski 2000). Furthermore, a complicating factor is that once control reduces the size of a separation bubble the natural shedding frequencies *increase*, which could mean simply that the optimum is indeed generally close to the shedding frequency of the controlled bubble.

The lower bound of effective frequency of actuation is set by the largest wavelength of perturbation that the separation bubble can amplify and this is usually approximately equal to the length of the bubble. This frequency also approximately corresponds to the vortex shedding frequency for most cases. A second issue for very low frequency forcing is that it by default has large periods with no control, which reduces overall effectiveness.

In the case of pressure-induced separations from low curvature surfaces with a wide region of intermittent separation, the mechanism of earlier reattachment through accelerated SL development is less apparent. Mohammed-Taifour and Weiss 2021 used a pulsed 2D slot jet to control a turbulent separation bubble induced by an imposed adverse-favorable pressure gradient on a flat plate. This study has a relatively high $Re_\theta = 5500$ and a relatively low adverse pressure gradient which produces a large region of intermittent separation and consequently no clear spectral peak for the initial shear layer instability. The authors find no apparent strong lock-on effect when using a forcing frequency close to that of natural vortex shedding and in fact as control reduces the size of the bubble the turbulent activity in the shear layer reduces with the bubble which leads them to conclude that forcing only slightly modifies the shear layer dynamics only by reducing the size of the bubble. Instead, their analysis of the control mechanisms points mainly at the momentum transfer induced by the actuator vortical structures delaying separation. The reattachment is consequently affected via a global viscous-inviscid interaction mechanism.

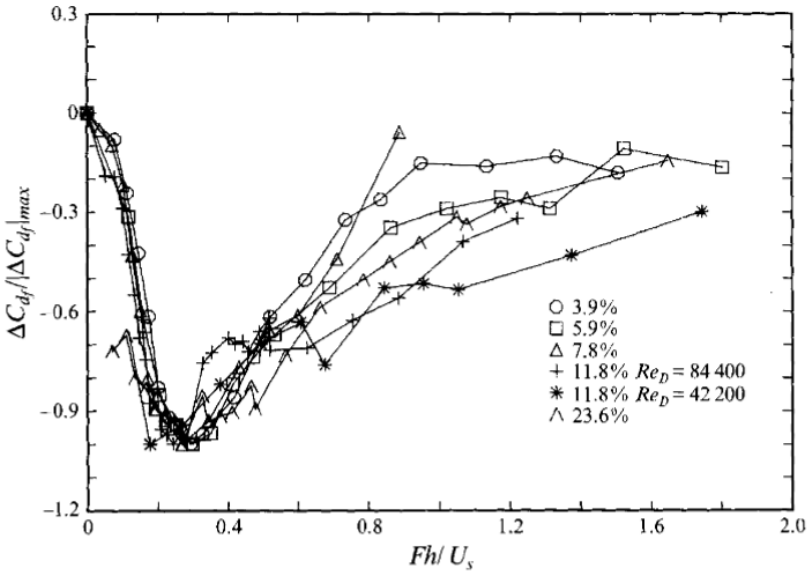

Figure 2.15: Drag reduction of a blunt-faced cylinder with axysymmetric fluidic control at the leading edge as a function of forcing frequency. From Sigurdson 1995.

They find that the control effect steadily grows with frequency due to the mixing effect of the jet produced spanwise vortices becoming more steady in time and at some point continuously suppressing the separation bubble rather than letting it recover to the unforced state between the passage of individual vortices. However, with an increase in frequency for a given velocity ratio, the jet vortices weaken and once the control effect on the bubble becomes quasi-steady the frequency trend reverses yielding an "optimal" frequency. This is compounded by the fact that the smaller weaker vortices dissipate more quickly further diminishing the effect. These observations are supported by a further investigation of the transient application and termination of forcing. It turns out that the response time of the bubble is commensurate with the time-scale of the low-frequency breathing mode of the bubble so the bubble is interpreted by the authors as a low-pass filter with a cut-off frequency. Once the cut-off frequency is surpassed by the forcing, the effect becomes quasi-steady.

High frequency actuation at frequencies an order of magnitude above the initial shear layer instability frequency has generally not shown any promise for separation control, however a few interesting results lead to continued interest in the topic. The most well known is that of Amitay and Glezer 2002 who observed that a slot 2D synthetic jet actuated at a frequency approximately 10 times larger than the vortex shedding frequency could completely prevent separation on a NACA0012 airfoil model, without the unsteadiness linked to actuation at lower frequencies.

In most cases however, including a lot of synthetic jet studies, high frequency actuation has a negligible or even detrimental effect for separation control. Stanek et al. 2002 and Vukasinovic et al. 2005 note that forcing of single-stream shear layer at frequencies an order of magnitude above the frequencies of the spectral peaks of the unforced flow seems to suppress the formation of ubiquitous large coherent structures and thus slows down the growth of the shear layer. It is clear how this would negatively affect separation control on account of reduced entrainment, as already discussed. Stanek notes that the high frequency actuation leads to an increase in local diffusion which alters the mean flow velocity profiles in such a way that they are more *inviscidly stable*. This hypothesis was validated by the work of Dandois et al. 2007.

Of interest is also forcing at multiple superimposed frequencies and whether or not multiple effects can be targeted in this way. In the simplest case, the actuation signal is made up of a higher "carrier" frequency and a lower "modulation" frequency. Besides studying single high-frequency actuation, Vukasinovic et al. 2005 investigated concomitant frequency actuation to control a backward facing step flow. They used a modulation signal in the form of a square wave with a 50% duty cycle and they confirm that large scale structures are generated by the low-frequency amplitude modulation of the high-frequency signal. It is in fact the onset and termination transients of the modulation cycle that

cause a quasi-step change in the boundary layer vorticity triggering the shedding of a large structure.

Their data seem to confirm that both the effects of high-frequency actuation, namely increased local diffusion, as well as the effects of large scale structure generation, namely increased entrainment, are present. Taking into account the dynamics and the response times of the overall flowfield it would seem that the two time-scales are uncoupled. However, this effect is achieved with separation happening on a sharp edge, where a Kutta condition can be invoked to explain the transient-induced shedding of a large structure. It is unclear whether the same would be true of a separation happening on a smoothly curved surface.

2.2.3. Two-dimensional jets

Due to the aforementioned potential benefits of 2D control, many studies investigate the use of 2D slot jets for separation control. A practical advantage of such actuators is that for 2D separation control problems, a 2D actuator reduces the parameter space by a whole dimension, which is highly beneficial for example in the case of synthetic jets which are already described by a large number of parameters. Furthermore, the representation of the geometry is massively simplified for numerical simulations (Leschziner and Lardeau 2011).

Clearly, if the jet is wall normal, a purely steady "curtain" of air would simply blow the crossflow boundary layer off of the wall, triggering rather than inhibiting separation. But in unsteady operation, slot jets can be quite effective. The fluid dynamic mechanism of control for this case is exemplified by the LES results of Dandois et al. 2007, shown in figure 2.16. This particular case is one where the actuation frequency is close to the vortex shedding frequency. A street of 2D spanwise roller vortices is formed at the downstream lip of the jet as seen in the instantaneous flowfield, while the upstream lip vortices have opposite sense to the crossflow boundary layer and are weakened by interaction with it, having little further effect.

The highly coherent large scale spanwise rollers sweep high momentum fluid into the region in front of them and generate a small local separation bubble just behind them at the wall. This means that what is effectively an intermittent triggering of separation, produces a highly unsteady but on average very attached flow seen in the time-averaged flow in figure 2.16. The vortex street is topologically completely similar to the naturally formed shear layer vortices and so by running the actuator at close to the natural shedding frequency it's clear how a resonance mechanism could easily be excited.

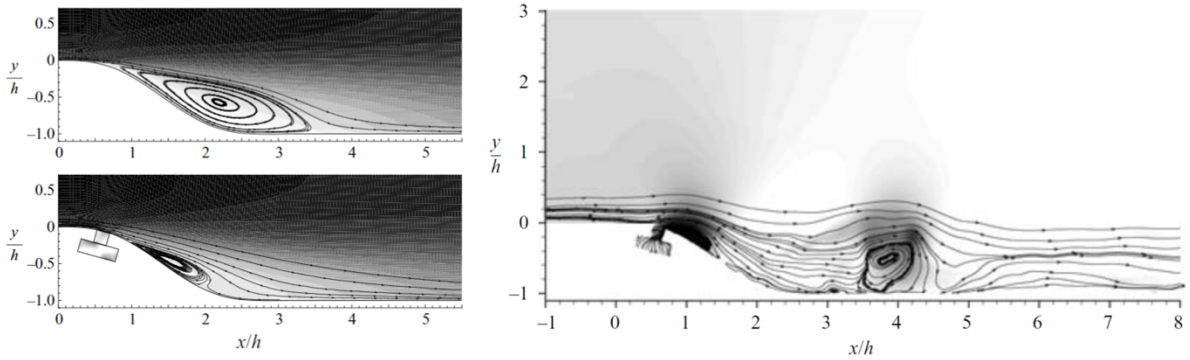

Figure 2.16: LES of turbulent separation control on a curved backward facing ramp using a 2D synthetic slot jet actuated at frequency close to that of natural vortex shedding. (*Left*) Mean streamwise velocity and streamline for unactuated (*top*) and actuated (*bottom*) cases. (*Right*) Instantaneous streamlines and pressure field for the actuated case. From Dandois et al. 2007.

2.2.4. Three-dimensional jets

As opposed to two-dimensional slot jets, finite "three-dimensional" jets produce a much more complex crossflow interaction which is marked by dominantly streamwise vorticity. The following discussion looks into the flowfield features of high and low velocity ratio jets and how these are affected by unsteady operation. These principles are then studied in the context of separation control by discussing various implementations of *vortex generating jets* (VGJ), so called because the streamwise vortices they produce

in the boundary layer are reminiscent of well-known solid vortex generators.

A quick note regarding turbulence; most studies that attempt to characterize jet in crossflow flowfield topologies deal with laminar flows because it is far simpler to observe and study structures which are in turbulent flowfields only seen in time or phase-averaged flowfields. The question arises then of how appropriate it is to apply insights gained from these studies to the issue of turbulent separation. Some authors (Jabbal and Zhong 2010; Zhong et al. 2007) argue that qualitatively, the structures generated by interaction with a laminar flow are the same as those produced by interaction with a turbulent flow. And since the goal of flow control is generally not a specific effect in a single instantaneous moment but a time-averaged or phase-averaged effect, studies conducted in laminar flows should have relevance for separation control application in turbulent flows.

Jet in crossflow topology

The flowfield of a jet in crossflow even with steady boundary conditions is still instantaneously highly unsteady. The time-averaged and instantaneous flowfield topologies of a high-velocity ratio steady round jet in crossflow are illustrated in figure 2.17. At high velocity ratios ($VR > 1$), the interaction between the jet and the crossflow boundary layer vorticity is weak or negligible.

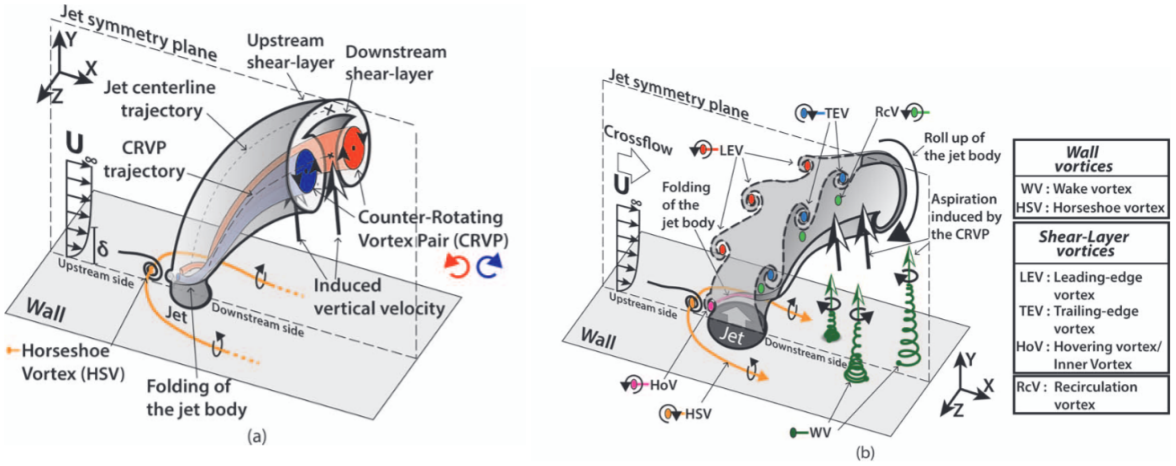

(a) Time-averaged. **(b)** Instantaneous.

Figure 2.17: High velocity ratio round steady jet in crossflow topology. From Cambonie and Aider 2014.

The dominant vortical structure of the time-averaged flowfield is the counter-rotating vortex pair ($CRVP$) which is aligned with the jet axis. While different mechanisms have been put forward to explain the formation of this structure, that proposed by Kelso et al. 1996 is the generally accepted explanation. They reason, based on experimental observations, that the CRVP is formed as the jet shear layer vorticity folds under the effects of self-induction. The downstream section of each vortex ring is pulled up and through the preceding vortex ring which has been convected downstream by the crossflow. This leads to a reorientation of initially streamwise vorticity in the direction of the jet axis and ultimately to the formation of the CRVP. Further information can be found in the work of Muppidi and Mahesh 2006 and Bidan and Nikitopoulos 2013.

The main feature of the instantaneous flowfield are the shear layer vortices, namely the leading edge (LEV) and trailing edge vortices (TEV), which are part of the vortex loops formed by the same self-induction mechanism that forms the CRVP (Lim et al. 2001). The horseshoe vortices are formed as the crossflow boundary layer separates under the influence of the adverse pressure gradient caused by the jet and forms vortices which wrap around the jet column and stretch downstream (Krothapalli et al. 1990). They are present in both the time-averaged and instantaneous flowfields but for large velocity ratios they have little effect on the overall behaviour of the jet.

The upright "wake" vortices on the leeward side of the jet seemingly look like the Von Karman vortex street in the wake of a cylinder. However, Fric and Roshko 1994 experimentally determined these wakes to be quite different at the same Reynolds number. They posit that the wake vortices stem from

separation events in the crossflow boundary layer driven by the adverse pressure gradient encountered on the leeward side of the jet, as described by (Ersoy and Walker 1985). These are then raised off the wall by the induced upwash of the CRVP if the CRVP is far enough for the space to be available, but close enough to produce enough upwash.

At and below a velocity ratio on the order of $VR \approx \mathcal{O}(1)$, the jet is strongly bent by the crossflow and the interaction of the jet with the crossflow boundary layer and the wall strongly affects its evolution. The studies of Bidan and Nikitopoulos 2013 and Cambonie and Aider 2014 systematically characterize this regime in which the structure of the jet-crossflow interaction is highly sensitive to minor changes in the boundary conditions resulting in multiple subregimes with different characteristics.

At low VR the blockage generated by the crossflow momentum at the leading edge of the jet is strong enough to disrupt the shedding of the jet LEVs. This leads to the formation of hairpin vortices illustrated in figure 2.18 and transitional vortical structures between vortex rings and hairpins, such as rings with trailing legs (Zhou and Zhong 2010). The discontinuous hairpin legs form in the time-averaged flowfield what appears as an attached CRVP. The horseshoe and counter-horseshoe vortices meanwhile wrap around the obstacle of the jet, forming positive and negative *side vortices* which are similar in strength to the quasi-CRVP. The evolution of the hairpins is dictated by the self-induction and the interaction with the wall which can be understood via its mirror image as shown in figure 2.18b. The legs are pushed together and lift off the wall. The spanwise head lifts off the wall but is also retarded by the induction of its mirror image which causes the entire structure to bend.

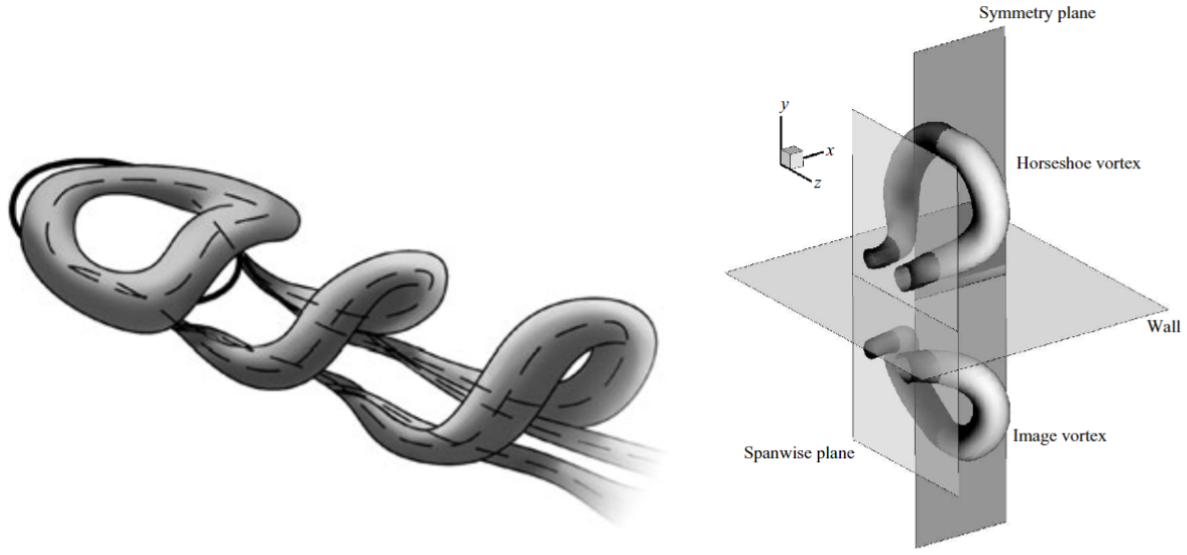

Figure 2.18: Hairpin vortices generated by a low velocity ratio jet in crossflow: (a) Illustration of the interlocked hairpin structure, connected to the inner vortex. From Bidan and Nikitopoulos 2013., (b) Vortex dynamics of a near-wall hairpin vortex. From Sau and Mahesh 2008.

Design for separation control

The dominant CRVP feature of a jet-crossflow interaction is the key structure in separation control systems using 3D jets. For jet boundary conditions symmetric about a streamwise, wall-normal plane, the CRVP is symmetric. By breaking this symmetry, a lopsided CRVP with a dominant streamwise vortex can be generated. Due to the similarity of the resulting flowfield to one generated by a solid vortex generator such jet actuators are often termed vortex generating jets or VGJs. The two most common implementations are shown in figure 2.19 and are a rectangular wall normal slit which has been skewed with respect to the crossflow and an pitched and skewed round jet.

A PIV acqusition of the crossplane downstream of such a rectangular VGJ with a skew angle $\beta = 45°$ taken by Scholz et al. 2005 is shown in figure 2.20. Clearly visible is a strong dominant vortex near the wall. Apparent also are the low streamwise momentum core, an increase in streamwise momentum

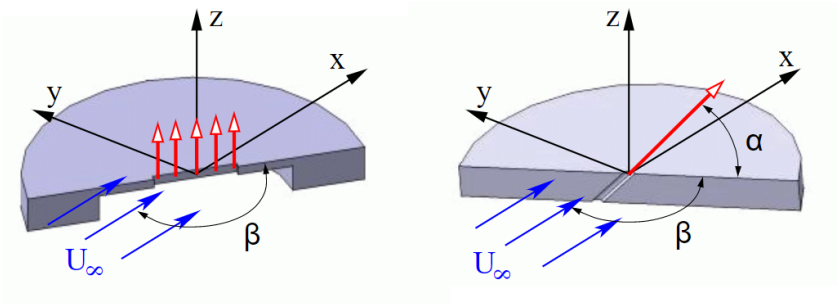

Figure 2.19: Vortex generating jet implementations: (*left*) high aspect ratio skewed slit and (*right*) pitched and skewed round jet. From Scholz et al. 2005.

near the wall on the downwashing side (right) and a decrease on the upwashing side (left). One can also identify a much weaker opposite vortex above it, with which it forms the jet CRVP. Due to the difference in vortex strengths, the small vortex orbits the larger one which is why in this plane, some streamwise distance downstream of the actuator, it has moved to directly above it.

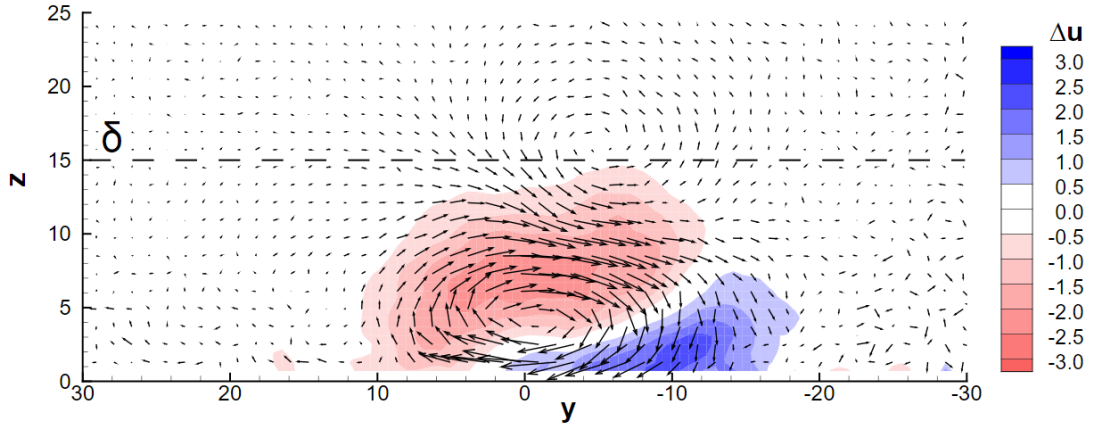

Figure 2.20: Crossflow plane PIV acquisition downstream of a rectangular actuator skewed at 45° with respect to the crossflow. PIV acquisitions of Scholz et al. 2005.

Round inclined VGJs have been demonstrated to offer higher peak performance than slit VGJs (Godard et al. 2006; Godard and Stanislas 2006). This is generally ascribed to the fact that the inclination of the jet, besides making the CRVP asymmetric, keeps the strong resulting vortex close to the wall while still allowing a high *VR*. This way the vortex strength is maximized and distance from the wall minimized, yielding the highest benefits for separation control. This geometry has been extensively developed particularly by the flow control research group at NASA Langley. They applied them to separation control of a backward facing ramp flow (Johnston and Nishi 1990), performed parametric studies (Selby et al. 1992) and characterized the resulting vortices comparing them against solid vortex generators (Compton and Johnston 1992).

While round VGJs might offer higher peak performance, they also show a much higher sensitivity to yaw than slit jets, as shown by Scholz et al. 2005. Furthermore, the lateral inclination of round VGJs results in a 3D trajectory so when the jet velocity is changed the trajectory moves in both the wall-normal and spanwise directions. This is a complication that makes wall-normal rectangular slits a more practical option in cases when the trajectory has to be relatively predictable such as was encountered in this research due to a limited test section span.

The two extremes of the wall normal slit jet are one aligned to the crossflow and one perpendicular to it. Smith 2002 experimentally evaluated both using HWA and found that spanwise oriented slots produce a boundary layer with the signs of a wake leading to a thickening of the boundary layer while

the streamwise oriented slits produce longitudinal vortices embedded within the boundary layer and show larger penetration. This is explored in more detail by the PIV acquisitions of Van Buren et al. 2016 who studied a comprehensive set of rectangular orifice pitch and skew angles. They find that the more streamwise oriented the long axis of the actuator is, the smaller is its wake and the larger its penetration. This behaviour is similar to solid bodies with different frontal areas immersed in a flow. They also find that the strongest and most persistent vortical structures are produced by wall-normal jets which is logical as this produces the largest velocity gradients in the cross-flow directions yielding the strongest streamwise vorticity. Both of these effects can be seen in the 3D Q-criterion iso-surface visualization shown in figure .

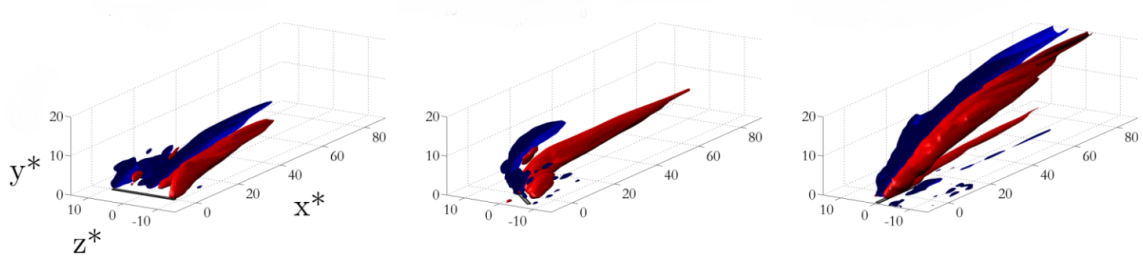

Figure 2.21: Iso-surfaces of Q-criterion for a wall-normal rectangular synthetic jet at skew angles of 0° (left), 45° (middle) and 90° (right) with respect to the flowfield. PIV acquisitions of Van Buren et al. 2016.

Both Van Buren et al. 2016 and Scholz et al. 2005 use their measurements of single actuators in a ZPG BL to make suggestions on the optimum skew angle β, based on quantities relevant to separation delay like the integrated streamwise momentum downstream of the actuator. Both groups report an optimum of $\beta = 45°$. However, the issue in applying these findings in separation control is that for practical separation control a continuous array of these jet slots is used and is most likely operating in an APG which is a significantly different situation to a single jet in a ZPG BL. Indeed a lower skew angle β is prefered for arrays operating in APG to reduce the low momentum wake of the jets. Godard and Stanislas 2006 performed parametric sweeps of full arrays of rectangular slit VGJs in an APG and reported an optimal skew angle of 15°.

There are multiple probable contributing factors to this that are useful to consider in the design of a separation control system. Firstly the mutual induction of the trailing vortices of a jet actuator array changes their motion and their growth eventually puts them in contact leading to an accelerated decay. Furthermore, more spanwise oriented orifices produce a larger blockage for the crossflow. So while in the case of a single orifice, the crossflow diverts not only above but also to the sides of the jet this three-dimensional relief is weakened significantly in the case of an array, leading to an effective increase in the blockage of each jet. Finally, the pressure gradient experienced by the vortex core is amplified by its circulation, which makes the vortices grow in size more quickly in APG than ZPG and in sufficiently strong adverse pressure gradients, could even lead to break down (Delery 1994).

Just like solid vortex generators, VGJs can be arrayed such that they produce co-rotating or counter-rotating arrays of vortices. Counter-rotating arrays produce more spanwise variation but also higher peak downwash onto the wall and consequently increase in shear stress, while in a co-rotating array vortices act in opposition to each other accelerating their decay. This locally stronger effect on separation means that for 2D separation counter-rotating arrays generally perform better when all other parameters are equal (Lin 2002). Furthermore, due to effects of self and wall induction the co-rotating array tends to migrate spanwise, while the counter-rotating array of vortices tends to lift off the wall.

Dynamic actuation

As already discussed, dynamically operated actuators are able to exploit flow instability to amplify the control input. There are further unsteady actuation phenomena related to jets which offer separation control performance gains which are discussed here.

For a start, impulsively started jets are marked by the formation of starting vortical structures which, although qualitatively similar to those produced by steady jets, are stronger and more coherent (Tricouros et al. 2022). The elaborate on this, consider that the source of the vorticity of these structures

is ultimately the velocity gradient around the orifice edge and on the wall of the jet duct. In the inviscid case, this would be a singular momentum discontinuity represented by a vortex filament, but due to the no-slip condition and viscous diffusion the vorticity concentration is finite and its value dictates the starting strength of the produced vortical structure. Since, as Tricouros et al. 2022 point out, for an impulsively started jet, the BL from within the jet duct has a larger concentration of vorticity, the starting structure is stronger than those produced later by the roll-up of the jet shear layer. The authors demonstrate this analytically by comparing the steady Blasius boundary layer and the impulsively started Stokes layer.

Besides the velocity ratio VR, to describe dynamically operated jets a further parameter is introduced, namely the stroke ratio L/D where the stroke length is

$$L = \int_0^T U_j dt = \langle U_j \rangle T \tag{2.23}$$

where U_j is the mean jet velocity across the orifice and T is the active blowing time. The different topological regimes can then be organized in a velocity ratio - stroke ratio parameter map, shown in figure 2.22 (Bidan and Nikitopoulos 2013). Below a $VR \approx 0.6$ starting hairpin vortices are formed, while above this VR starting rings are formed. Furthermore, for each VR there is a *formation stroke ratio* below which a single starting structure is formed, and above which the starting structure is followed by trailing structures similar to the steady state. If the pulsing frequency is sufficiently low or in other words the stroke ratio long enough, the jet reaches a quasi-steady state between transients.

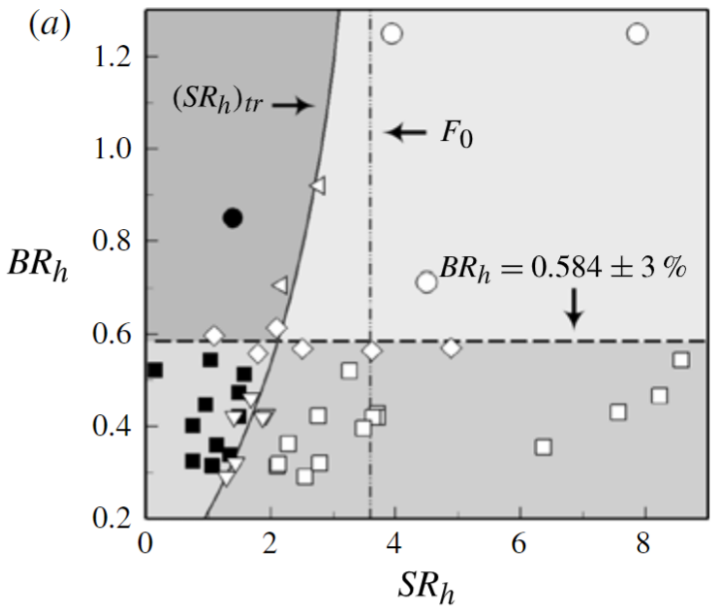

Figure 2.22: Velocity ratio - Stroke ratio parameter maps for impulsively started (pulsed) jets. Above/below dashed line: rings/hairpins. Right/left of solid line: with/without trailing column. From Bidan and Nikitopoulos 2013.

Zhou and Zhong 2010 build up a similar map for a round synthetic jet in a laminar crossflow with a target application in separation control. While there is a slight difference in the transitional VR, the actuation structures produced by pulsed and synthetic jets are qualitatively similar, which is a valuable finding because it expands the pool of relevant literature for each actuator type. The authors attempt to assess the effectiveness of the various flowfield topologies for separation control based on surface shear stress. The same study was performed experimentally by Jabbal and Zhong 2010 using quantitative thermography. Generally, with increasing velocity and stroke ratio, or in other words increasing *added momentum*, there is a larger integral gain in momentum, which is only logical. However, the consensus is that the transitional form of stretched vortex rings (effectively high VR hairpins) shows the largest net increase in wall shear stress with the largest streamwise persistence and the smallest RMS of wall shear

fluctuations. This serves to indicate that conscious design of the topology of the actuator jet flowfield can enable particularly efficient systems to be designed.

This was then put to the test when Zhang and Zhong 2011 controlled a turbulent separation bubble formed of a curved backward facing ramp using 3 round wall-normal synthetic jets, following up with a more in-depth investigation (Zhong and Zhang 2013). The relatively low VR synthetic jets produce trains of hairpin vortices. The counter-rotating hairpin legs and secondary induced structures draw high momentum fluid towards the wall and low momentum fluid away from it. However, the hairpin heads also play an important role which is illustrated by the contours of the periodic velocity fluctuations shown in figure 2.23 as they generate strong sweep events just downstream.

After an initial frequency sweep, they noted two local minima in the height of the separation bubble. One of the minima corresponds to the natural shear layer frequency of vortex shedding $St_h = 0.2$ and this seems to indicate that some degree of control amplification is happening. The authors reason based on results of Zhou and Zhong 2010 that the second, higher optimal frequency leads to an optimal streamwise separation between the hairpin heads to maximize this effect while at the same time keeping the separation bubble continuously suppressed. Lardeau and Leschziner 2011 however numerically replicate the investigation and finds negligible frequency sensitivity expressing doubt about the excitation level of the shear layer modes.

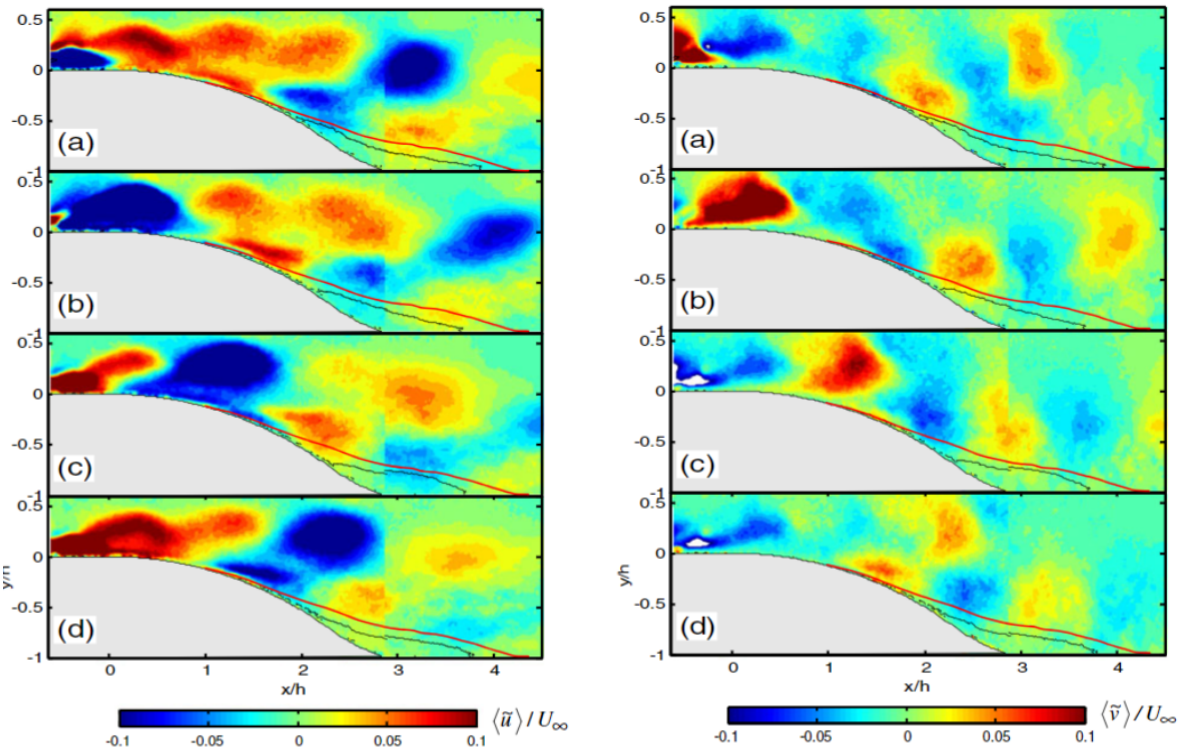

(a) **(b)**

Figure 2.23: Contours of periodic (a) streamwise and (b) vertical velocity in the center plane behind a round synthetic jet actuating a turbulent separation bubble formed on a curved backward facing ramp at four phases of the actuation cycle 0°, 90°, 180° and 270° (from top to bottom). The velocity ratio is $VR = 0.3$ and the frequency is $St_h = 0.2$. From Zhong and Zhang 2013.

Besides changes to flowfield topology, there are a few other factors which make pulsed jets more advantageous for separation control. Ortmanns et al. 2008 experimentally studied pulsed wall normal jets issuing from a rectangular orifice. They found that the start-up process is dominated by an overshoot in velocity. They ascribe this to the fact that upon the opening of the jet valve, the quiescent fluid in the feed line is suddenly exposed to a large pressure gradient, but due to an undeveloped velocity profile, the bulk of the flow experiences very little shear stress. This overshoot helps to generate an even stronger starting structure which is not present for a steady jet.

Finally, multiple authors have found increased penetration for pulsed jets compared to their steady counterparts (Eroglu and Breidenthal 2001). This is connected to the discrete vortex ring (loop) structure that is a feature of pulsed jets and the increased penetration is in fact a function of the vortex ring spacing.

Leveraging the benefits of these transient phenomena enables stronger effects with less required mass flux (Cattafesta and Sheplak 2011). For example, Steinfurth and Weiss 2022 use pulsed jets to control a separated flow in a one-sided diffuser test section and find that a duty cycle of 0.1 produces an equal or even better control effect compared to a duty cycle of 0.5 while simultaneously requiring 3 times less massflow. Based on the aforementioned factors, it makes sense that most of the jet control effect is in the start-up phase, allowing the duty cycle to be shortened without disadvantages as long as the start-up is unaffected.

Another strategy that makes use of this is so called burst modulated actuation where, during one modulation period, the jet is started and shut multiple times, maximizing the vorticity generated. Abdolahipour et al. 2022 used such a strategy to operate a spanwise counter-rotating array of vortex generating jets installed in the flap of a multi-element wing and found again the same or improved control effect while requiring half the massflow. If this is completely due to the start-up phenomena it is possible that the optimal pulse duration is precisely that equal to the formation stroke lengths such that a *single* structure of maximum strength is produced. All blowing past that tends toward a steady state, with weak trailing structures.

2.3. Summary and research motivation

A review of the state-of-the-art of jet actuator separation control has shown that arrays of jets generating lopsided CRVPs (vortex generating jets) are an extremely promising separation control system. Unlike conventional solid vortex generators, these jet arrays offer the advantage of being able to be turned off when not needed, thereby avoiding performance penalties. Furthermore, the jets allow for greater control flexibility in the form of variable perturbation magnitude and control timing which can be actively adjusted to the operating conditions. In particular, dynamically operating these jets generates transient flowfield features which yield improvements in the separation control effect while requiring a smaller mass flow. One of these dynamic phenomena is the modulation of the development of the separation shear layer.

The objective of this study was to develop and apply a vortex generating jet (VGJ) array to the control of a pressure-induced high Reynolds number, thick turbulent boundary layer (TBL) separation. Such a scenario, in which the magnitude and scale of the outer BL turbulent structures is commensurate to those generated by actuation, is relevant to the flow over aft bodies of aircraft, rotorcraft, or ships, and has not been extensively addressed in the existing literature. Steady and unsteady actuation strategies with various operating parameters were tested to validate the presence and significance of performance trends and flowfield features reported in other separation control studies. Particle image velocimetry and hot wire anemometry techniques were employed to characterize the spatial and temporal scales of the flowfield.

Furthermore, a novel alternating VGJ actuation strategy is proposed, whereby the sense of the streamwise vortices is alternated at time-scales shorter than those of the separation bubble response time. This approach aims to create a quasi-2D perturbation, taking inspiration from Squire's theorem, with the goal of enhancing the excitation of the 2D Kelvin-Helmholtz instability mode in the separated shear layer while retaining some of the advantages of 3D actuation reported by various comparative studies.

3

Experimental methodology

This chapter details the design of the experiment as well as the measurement and processing techniques used. Section 3.1 presents the design and implementation of the flow actuators and the backward facing separation ramp. The calculation procedure for an inviscid solution for the flow geometry, which was required for parts of the analysis, is covered in section 3.2. Subsequent sections then detail the used flow measurement techniques including pressure measurements (section 3.3), PIV (section 3.4) and HWA (section 3.5).

3.1. Experiment design

3.1.1. Test section and separation ramp

This experimental study was carried out in the W-tunnel of Delft University of Technology, an open-circuit wind tunnel powered by a centrifugal fan used for low subsonic aerodynamic testing. Different contractions and test sections can be attached depending on the use case. For this research, a 60x60cm contraction is installed allowing a maximum velocity of 16.5 m/s.

Figure 3.1: Modular turbulent boundary layer test sections developed for use in the W-tunnel by Dacome and Baars 2023.

The test section used downstream of this contraction is the turbulent boundary layer set-up developed by Dacome and Baars 2023. It consists of two modular 1.8m test sections, shown in figure 3.1, which are designed to produce a high Reynolds number boundary layer using the "long and slow" approach, commonly used in turbulent boundary layer facilities. The long development length ensures a high Reynolds number, while the low speed ensures a boundary layer thick enough to provide high measurement resolution.

The lower wall is flat and made of panels which can be switched out, while the ceiling is made of flexible 4mm polycarbonate mounted on movable spanwise beams. By adjusting the beam positions, the streamwise ceiling curvature and consequently the pressure gradient along the tunnel can be controlled. The leading edge of the lower wall is fitted with a knife edge and sits above the lower rim of the contraction. A deflector panel is attached to this lower rim to adjust the flow direction at the knife edge to prevent separations. The first 10 cm of all four walls are covered with P40 sandpaper to initiate transition.

Separation was triggered on the lower wall by the implementation of a smoothly curved backward facing ramp, a commonly used geometry to study pressure-induced separation. The strategy to install the ramp in the section is adopted from the master thesis research of Ramírez Vázquez 2022. The upstream section is raised on concrete blocks to the required ramp height and then the first replaceable panel of the downstream section is replaced with the ramp assembly. While a new ramp assembly was designed, because Ramírez Vázquez 2022 studied the separation from a sharp-edged ramp, some components from that research were reused in the present experiments.

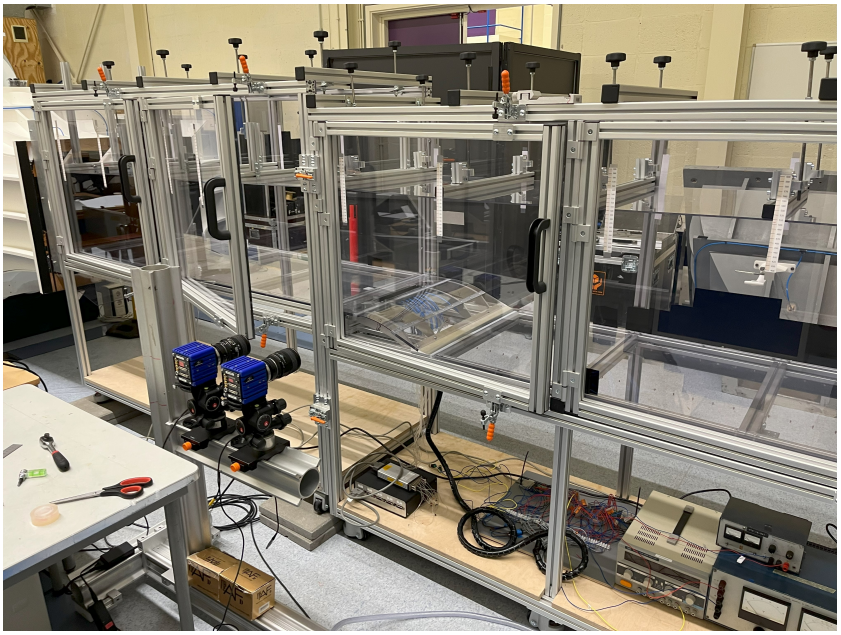

Figure 3.2: Curved backward facing separation ramp test section showing the upstream section lifted on blocks.

The ramp profile is shown in figure 3.3. The upstream flat development section is 1.94 m long and is connected to a flat inclined backward-facing section by a section with constant, low curvature. This type of profile has been extensively utilized by the group at NASA Langley (see Lin 1992) and it was selected in the present case because it allowed for a modular design that reused a large amount of material of the sharp-edged ramp previously tested by Ramírez Vázquez 2022.

A comparison of the key parameters of the present ramp with notable implementations from literature with similar profiles is given in table 3.1. For reference, in the present case, PIV of the uncontrolled flow determined the δ_{99} of the BL upstream of the ramp to be 120mm.

Regarding the proportions of the ramp, firstly, the ratio l/h has the strongest influence on the APG and the extent of separation and its value for the designed ramp is within the range of commonly encountered values. Secondly, since the test section has a limited span the flow will necessarily be three-dimensional, but to what extent is primarily driven by the ramp aspect ratio l/w (Simmons et al. 2022). For cases with $l/w << 1$, one can safely regard the flow around the central plane of the test section as two-dimensional and this is the case for multiple studies listed here which use very high aspect ratio BL tunnels to achieve it.

Given the relatively low and fixed span of the present set-up, the aspect ratio can only be lowered by reducing the length and height of the ramp. However, one also needs to consider that the ratio δ/h determines how significant of a perturbation the separation is to the BL and conversely, how influential

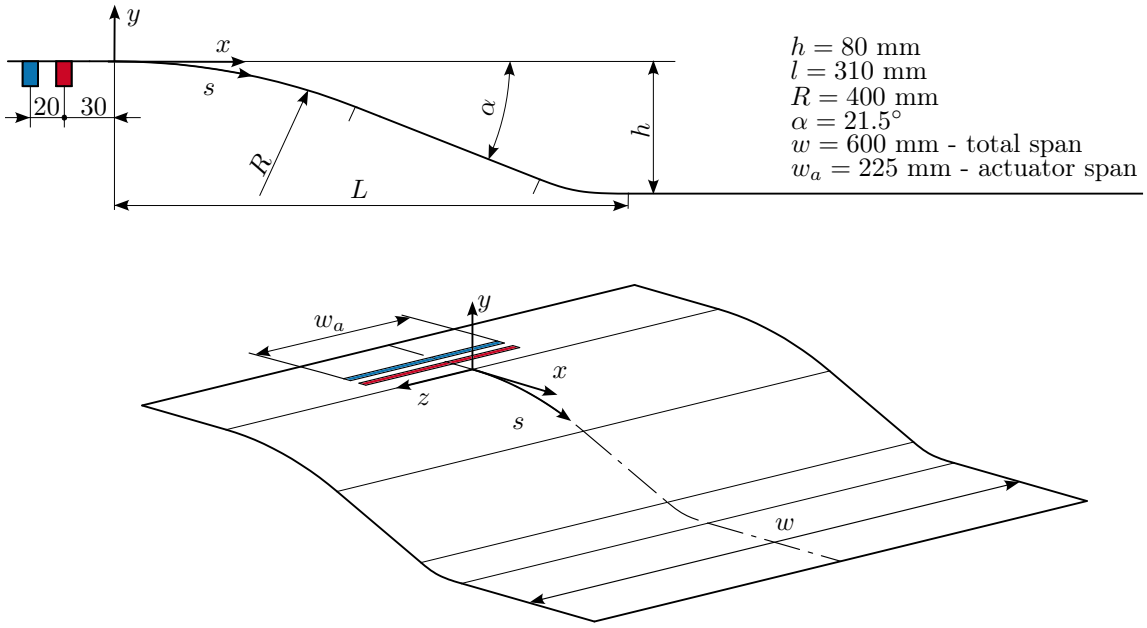

Figure 3.3: Separation ramp schematic with coordinate system, dimensions and marked actuator positions.

Study	δ/h	δ/R	l/h	l/w	profile
present	1.5	0.3	3.9	0.75	flat incline with fillets
Koklu 2018	0.25	-	5.3	1.1	Stratford
Zhong and Zhang 2013	0.89	0.22	2.8	0.07	circular arcs
Debien et al. 2014	0.22	-	3.3	0.24	5th order polyinomial
Lin 1992	0.86	0.16	4.7	0.18	flat incline with fillets

Table 3.1: Curved backward facing ramp design parameters from this and other relevant separation control studies.

the BL dynamics are on the dynamics of the TSB. When the TSB is small with respect to the upstream BL, most of the BL simply flows above the bubble almost undisturbed and after reattachment, recovers very quickly to its canonical form (Simpson 1996). Simultaneously, the dynamics of detachment are significantly driven by the turbulence of the incoming BL along with the APG and wall curvature.

To achieve a very low l/w, the ramp would have to be an order of magnitude smaller than the BL. So in a bid to keep the influence of the BL turbulence and the APG on the TSB dynamics commensurate, the target scale ratio of the TBL and the TSB was $\delta/h = \mathcal{O}(1)$. The experimental set-up used in this experiment particularly lends itself to this studying this type of flow, because the large BL scale allows a high resolution of the TBL unsteadiness. Consequently, this necessitated an aspect ratio of $l/w = 0.75$ which, while high, is still within the range observed in other separation control studies. The resulting three-dimensionality of the flow is analyzed in section 5.1.

An improved set-up with a lower l/w within the same test section would require a simultaneous reduction in the height of the ramp and the boundary layer thickness. To retain a similar Reynolds number this would then require a movement of the ramp upstream and an increase in tunnel velocity. The former could be achieved but would require a significant redesign of the upstream test section, which was determined to be out of the scope of the present work, while the latter is impossible as the tunnel fan was already being run at maximum RPM.

Lastly, such a thick BL required a proportionally large curvature radius to ensure that detachment was mainly driven by APG rather than surface curvature, according to the objectives of this research. The specific value for R was selected for a target $\delta/R = 0.15$ based on the observations given by Simpson

1996. The actual BL δ ended up being twice as thick as initial predictions, due to the APG modifications imposed by the ceiling, but even so the final δ/R presently is not much larger than for the other listed cases.

The overall tunnel geometry, including the tested ceiling profile, is shown in figure 3.4. After initial experimentation with a flat tunnel ceiling, the extent of the separation region was found to be quite small. To increase it the ceiling was set to the configuration shown, which increased the adverse pressure gradient imposed on the flow and the size of the separation bubble. This scheme also shows the positions of the Prandtl-Pitot tube used to set the tunnel velocity and the static pressure taps along the lower wall used to determine the streamwise pressure distribution.

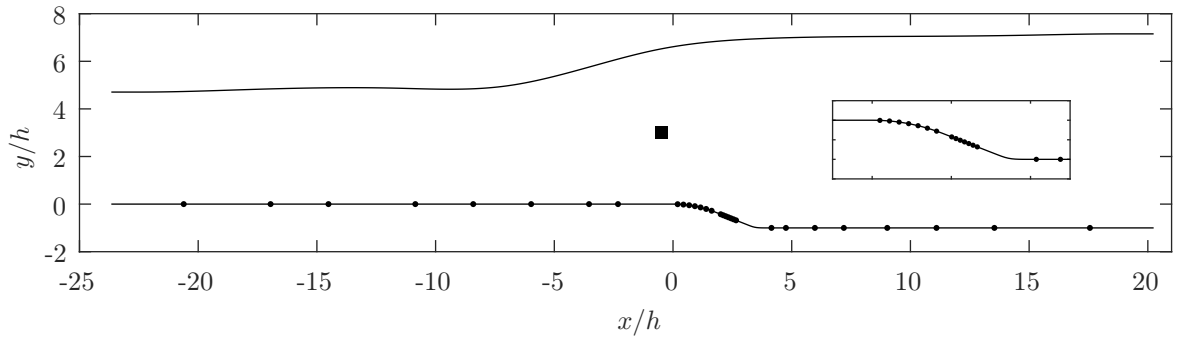

Figure 3.4: Profile of the entire length of the test section including the ceiling. Positions of static pressure taps marked by (•) and Prandtl-Pitot tube by (■).

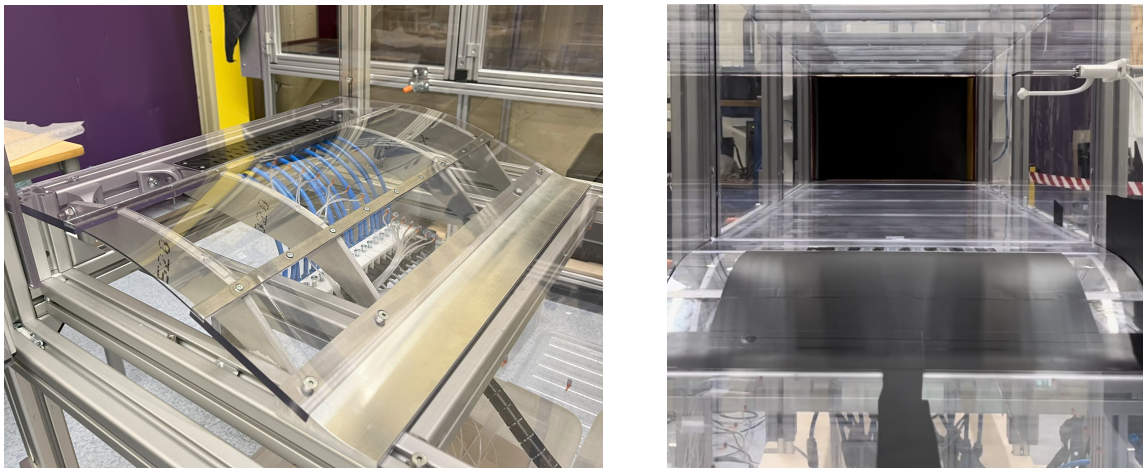

(a) **(b)**

Figure 3.5: Photos of the installed separation ramp: (a) isometric view with the actuator and pressure taps apparent, (b) view upstream with ramp installed in the tunnel and covered by black antireflective tape.

The completed ramp installed in the test section with actuators is shown in figure 3.5. The flat sections are made out of the same 9.5mm polycarbonate plate as the rest of the test section, while the curved section is made out of 2mm polycarbonate sheet which is bent over 4 aluminium ribs to the design radius. Although the sheet is thin, the bending preload gives it a high degree of rigidity. Because the sheet shape is supported at only 4 spanwise locations by the ribs, to prevent twisting 2mm steel strips were sandwiched in the overlap joint between the sheet and the upstream and downstream polycarbonate sections, which along with a row of countersunk bolts, kept the edges flat and flush with the upstream and downstream sections. A milled aluminium block, originally designed by Ramírez Vázquez 2022, with a concave fifth-degree polynomial profile joins the inclined plate with the downstream tunnel section.

3.1.2. Actuator

The actuator is an array of non-zero mass flux jets, fed by pressurized air and controlled by fast-acting solenoid valves. Each of the jets is designed to produce a dominant streamwise vortex in interaction with the crossflow, acting as an active, controllable vortex generator. In this section, firstly the geometry of the jets that produces this interaction is discussed. This is followed by a description of the feed system and manifold and finished with a description of the open-loop control strategy.

Vortex generating jet orifice geometry

A predictable jet trajectory was deemed important for this project because of the limited span of the test section, easier positioning of the PIV planes and so that the proposed alternating actuation strategy could be tested without an extra unknown in the form of the spanwise offset between the actuation structures of the two rows. Furthermore, even though pitched round VGJs seem to offer better peak performance, this performance is much more sensitive to operating conditions like crossflow yaw (Scholz et al. 2005). For these reasons a rectangular, high aspect ratio, wall-normal jet implementation is prefered in this project.

To form an actuator row, the jets are arrayed along the span in a counter-rotating arrangement which was preferable to the co-rotating configuration (Lin 2002). Furthermore, the actuator has a second, mirrored row offset in the streamwise direction to enable the proposed alternating actuation. In further discussion, the downstream row (marked in red) is refered to as row 1, while the upstream row (marked in blue) is refered to as row 2. The final, tested actuator layout and dimensions as well as a schematic of the conventional and alternating actuation are shown in figure 3.6. Note that the actuated span width w_a shown in figure 3.3 is nominally considered to be equal to 6 times the jet spacing $w_a = 6\lambda_j$. This is consistent with considering a set of 6 jets taken from an infinite array.

To elaborate on the proposed alternating actuation consider the schematics in figure 3.6. Conventional actuation with row 1 nominally produces an array of streamwise vortices that has a spanwise varying effect on wall shear dependent on the sweep/ejection pattern induced. By alternating between the two rows during actuation as illustrated, at time scales shorter than the response time of the detachment line, the intent is to produce, in the time-averaged sense, a more spanwise uniform, "quasi-2D" effect on the wall shear. If this high frequency alternation is then modulated by a frequency close to the natural flow frequency, a quasi-2D periodic actuation is achieved using a 3D actuator. Based on Squire's theorem, this is hypothesized to yield a stronger effect on the separated shear layer instability than could be achieved with conventional 3D actuation.

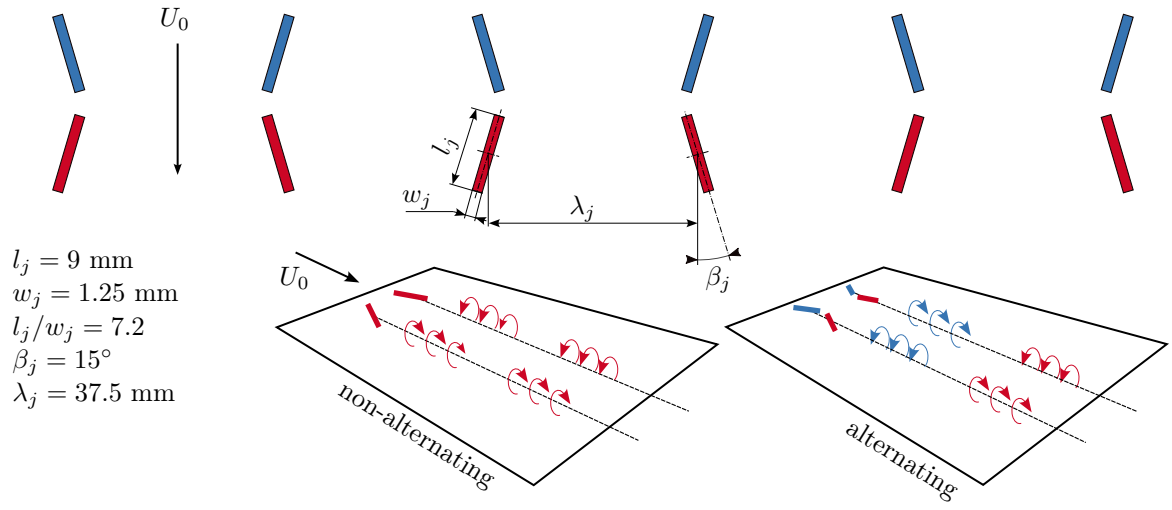

Figure 3.6: Actuator jets: geometry, dimensions and operation schematic.

The aspect ratio of the jets was adopted from a range of commonly implemented values while making sure that the width was large enough for printing in PLA without issues. The skew angle β was set according to the discussion given in section 2.2.4. Although studies of isolated actuators in ZPG boundary layers indicate higher skew angles $\beta = 45°$ to be optimal for separation control, a significantly

lower value of 15° is selected. This is because the importance of minimizing the low momentum wake of the jets was expected to increase when the jets are arrayed and operating in an adverse pressure gradient which stands to expand the wakes.

The jet spacing was initially set to 1/4 of the predicted BL thickness to mimic the average spanwise length scale of the large scale outer layer motions. The dimension of each orifice was then set according to a target porosity λ_j/l_j. Initially, there was a plan to directly compare a 2D slot jet with this VGJ array at the same mass and momentum flux requiring the same orifice area. Despite efforts to the contrary, this could only be achieved with a porosity that in initial testing proved to be too small, leading to earlier rather than delayed separation. So comparison with the 2D jet was abandoned and the spacing (and porosity) of the jet increased threefold to the final value given here. This worked out favourably with respect to the BL thickness because the prediction of δ was based on ZPG experiments and underestimated the actual value by more than twice.

Feed system

The actuators are fed by pressurized air from the laboratory supply via a settling tank and the actuator manifold. The jet velocity is adjusted via a pressure regulator connecting the settling tank to the 10bar pressurized air supply. The pressure regulator is passive and therefore during operation the pressure in the tank depends on the mass flow through the system. From the tank the air supply is split into separate lines, each of which connects to a fast acting Festo solenoid valve and from there into the actuator manifold.

The upstream part of this system was adopted from Dacome 2021, while the actuator manifold was specifically designed for this research and was 3D printed out of PLA polymer. The main design targets for the manifold were to:

1. make the design modular to enable easy changes to the jet geometry,
2. actuate a span of at least $w_a = 2.5h$ =180 mm,
3. enable actuation frequencies up to 100 Hz,
4. achieve a uniform and wall normal flow at the orifice with minimum losses through the cavity.

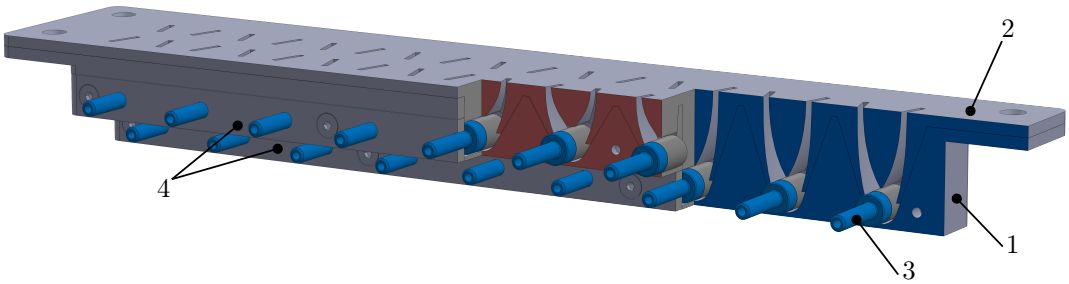

Figure 3.7: Isometric view of manifold CAD model with sections through both jet cavities. Components: 1 - block, 2 - lid, 3 - filter, 4 - closing plates. Red section: downstream actuator row, blue section: upstream actuator row.

The CAD model of the final manifold design is shown in figure 3.7 with sections to show the internal geometry. It consists of two main components, a main block (1) and a lid (2). The block has 18 cavities, with 9 per actuator row, each of which contains a Festo filter (3) held in place by closing plates (4). These filters add additional pressure drop to the system to enable finer control of jet exit velocity via the pressure regulator as the velocity is otherwise extremely sensitive to adjustments. The flow exits the filters radially through it's cylindrical face, which is why the filters are oriented horizontally within the block.

The components are connected by M3 countersunk screws. The closing plate screws self-thread holes drilled in the PLA material, while the lid screws go through the block flange and screw into threaded holes made in the upstream ramp flate plate. The manifold is sealed using double sided and teflon tape, but due to the relatively low operating gauge pressures in the cavities, leakage was minimal so achieving proper sealing was not difficult.

The top surface of the lid forms part of the test section surface, lying flush with the tunnel floor. The main jet ducts are designed into lid protrusions which slot into the main block and fit snugly around the filters. Such a design of the lid and block allows various orifice geometries to be installed with ducts optimized for each case. It only requires the printing of a new lid, with no dissasembly of the rest of the system required, satisfying requirement 1.

Because of test section structural elements upstream of the actuator, feed lines of the upstream jet row (blue section) couldn't be freely routed in that direction so a staggered design was adopted to enable the feed lines of both rows to attach from the same direction. The upstream and downstream cavities are therefore different, with the downstream cavities being shorter.

The number of supply lines from the settling tank was limited to 15 and so with the initially planned spanwise jet spacing, the only way to actuate across a large enough span (requirement 2) was to design a lid in which each block cavity fed two rather than a single jet. To prevent flow asymmetry or oscillation between the two orifices, the splitter between the two jet flow paths was purposefully made relatively sharp and extended all the way to the filter with the aim of isolating the flow paths. Ultimately, when after initial control testing the jet spacing needed to be increased, this turned out to not be necessary. Due to time constraints, instead of printing a new lid, one jet duct per active cavity was simply blocked off.

Also related to the jet duct design, requirement 4 would need to be experimentally verified using a flow visualization technique like PIV, which has not been done. However, great care was taken to create smoothly curved internal cavity surfaces. The flow volumes of both cavities are shown in figure 3.8, excluding the filters which are meant to slot into and fill the cylindrical volume apparent in these images. Because cavity 1 is slightly shorter, a more aggressive curvature of the duct is necessary, which ultimately lead to more losses.

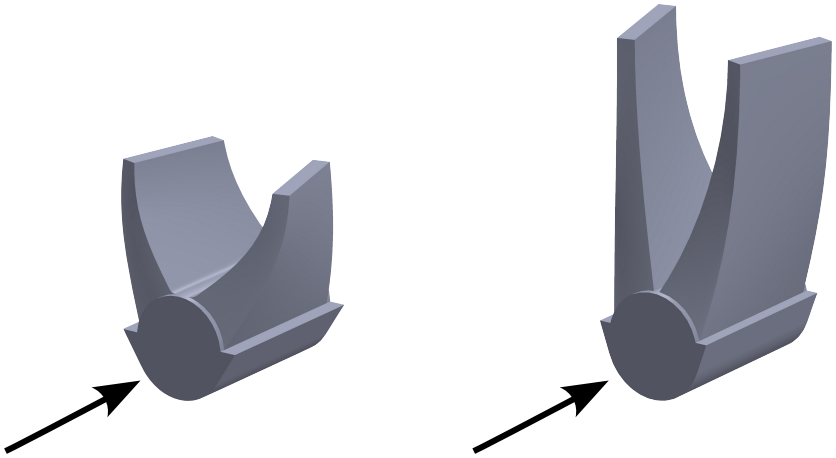

Figure 3.8: Flow volume of manifold cavities: left - cavity 1 (downstream row), right - cavity 2 (upstream row).

To elaborate on requirement 3, the decay time of the jet velocity after the valve is shut dictates the highest frequency that the actuator can be run at while still allowing the jet to fully stop between active blowing periods. As a first approximation, consider a lumped parameter model of the jet cavity. From a steady state blowing condition when the valve is shut off the decay is governed by conservation of mass in the cavity as

$$V\frac{d\rho}{dt} = -A\rho U_j(p,\rho) \tag{3.1}$$

where U_j is the jet velocity. For the same working fluid, initial conditions and cavity losses the decay time of the jet velocity depends exclusively on the characteristic cavity length scale V/A.

By making exactly these assumptions, the upper bound on V/A for the present design was set to 66.3 mm according to the results of a characterization of a similar manifold and the same feed system carried out by Dacome and Baars 2023, where frequencies up to 100 Hz were still found to be usable. Ultimately a lower value was achieved by the lid design for both cavities, 39.6 mm for cavity 1 and 54.1 mm for cavity 2. Note that the volume V is taken to *exclude* the filter and the section of air line from

the valve to the filter. The pressure drop through that filter is so significant that it is reasonable to assume that the pressurized air upstream of it contributes little to the residual jet velocity compared to the pressurized air in the cavity.

When after initial tests the jet spacing was increased this was done simply by utilizing every third jet orifice and blocking off the rest. As only one duct in every second cavity was used, the total cavity orifice area A was halved. So to retain the intended frequency characteristics, the unused jet ducts were plugged from within the cavity rather than at the exit using modelling clay, effectively cutting the cavity volume V in half as well and retaining nominally the same V/A scale.

Control

Regarding actuator control, figure 3.9 illustrates all of the actuation modes tested in this research. The open-loop control signals were generated using an NI-cRIO controller, programmed in LabVIEW 18. Those which only include the downstream row of actuators are termed **3D1** and colored in red, while of the modes which also include the upstream row of actuators are termed **3D2** and marked with blue. So for steady blowing (**S**), 3D1 and 3D2 refers simply to whether the downstream or the upstream rows are blowing. For unsteady actuation cases meanwhile, 3D1 means that only the downstream row is firing, while 3D2 means that the downstream and upstream rows are firing in alternating fashion.

For unsteady actuation, two different timing signals types were tested: single frequency actuation and burst modulation. Single frequency actuation is self explanatory and consisted simply of a square wave with a 50% duty cycle. The burst modulated signal meanwhile is a combination of two square signals: a carrier signal and a modulating signal. The nominal period (and frequency) of the signal is that of the modulation component, which is marked in the illustration. The frequency of the carrier is exactly 3 times larger, meaning the burst modulated signal has an effective duty cycle of 33%.

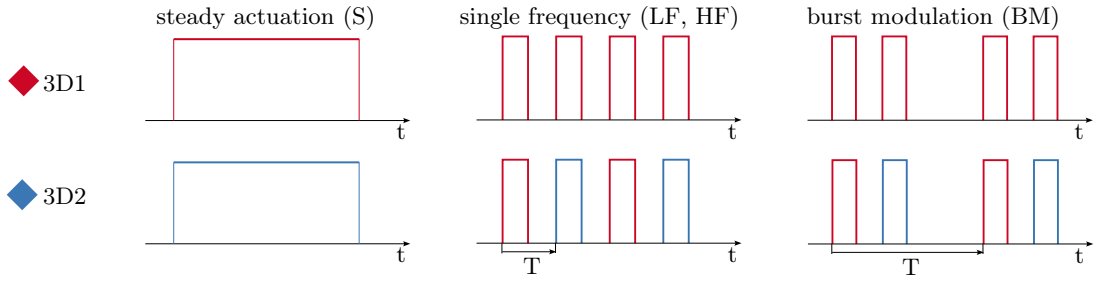

Figure 3.9: Trigger timing scheme of the tested actuation strategies. Red: downstream row 1, blue: upstream row 2.

The cRIO controller is operated in Scan Mode, instead of compiling the control code on the built-in FPGA, such that the operating parameters can be quickly changed during control sweeps. This however means that the refresh rate of the I/O streams of the controller is set at 2kHz. So to achieve a precisely timed control signal with no jitter, each timed period, active or inactive, in the tested control signals needs to be a multiple of 0.5 ms. For single frequency actuation at $DC = 50\%$ this means that the tested frequencies all conform to the following expression

$$f = \frac{2000DC}{k},\ k = 1, 2, ... \tag{3.2}$$

The highest achievable frequency is 1000 Hz which is the maximum that the valves are rated for and significantly higher than what the jet cavity is able to achieve and thus completely sufficient for the purpose. A side-effect of this, ultimately unimportant to the experiment objectives but important to point out, is that the tested frequencies aren't necessarily round numbers. The three actuation frequencies that were used in detailed analysis are for example 27.78, 83.33 and 111.11 Hz.

Finally, setting the actuator jet velocity is done in quiescent conditions. A thin Pitot probe is positioned just above the jet orifice and the jet is turned on in steady blowing mode. The measured dynamic pressure is then used to set the nominal jet velocity by adjusting the pressure regulator connecting the settling tank to the laboratory compressed air supply. Because of the finite size of the tank and the nature of the regulator , when the jets are pulsed this velocity changes slightly (see actuator characterization results 4.1). Furthermore, turning the tunnel on also affects the realized jet velocity due to the crossflow interaction and the change in static pressure above the actuator.

3.2. Inviscid flow calculation

In this work the 2D inviscid flow solution for the test section geometry is used for the determination of boundary layer parameters and for the evaluation of control effectiveness using pressure measurements. This section therefore describes the methodology used for obtaining that solution.

An inviscid incompressible velocity field can be represented by the gradient of a scalar potential Φ. The continuity equation therefore reduces to the Laplace equation

$$\nabla^2 \Phi = 0 \tag{3.3}$$

For a flow with no singularities or trailing edges in which the Kutta condition has to be invoked, any solution to this equation is a valid flowfield. For steady potential flows, the momentum equation reduces to the Bernoulli equation, valid through the entire domain, which states that the total pressure is constant

$$\nabla \left(p + \frac{1}{2} \rho U^2 \right) = 0 \tag{3.4}$$

For a given geometry with proscribed BCs, the velocity field is first obtained by solving the Laplace equation after which the pressure follows from the Bernoulli equation.

In the present case, the test section, shown in figure 3.4, is treated as a closed domain with an inlet, outlet and upper and lower walls. At the walls Neumann BCs prescribe a zero component of velocity normal to the wall $\vec{n} \cdot \nabla \Phi = 0$. At the inlet and outlet Dirichlet BCs are prescribed giving constant values of potential Φ, -1 at the inlet and 0 at the outlet. The actual values are not important because the Laplace equation is linear so the obtained solution can simply be scaled and remain valid. Secondly, the pressure is non-dimensionalized to form the static pressure coefficient C_p which then remains unchanged regardless of velocity scaling.

The Laplace equation is solved using the finite element method after discretizing the domain with a structured mesh composed of linear triangular elements. The solver was implemented in Matlab based on the implementation put forward by Alberty et al. 1999. The calculated C_p field with overlayed mesh nodes, is shown in figure 3.10. Every tenth mesh node is shown for clarity. The mesh is particularly refined around the ramp with care taken to keep the element aspect ratio close to 1 in that region. While a mesh sensitivity study was performed, the solution procedure is so quick that the mesh was made preemptively too dense. Finally, the solution was validated against a finite volume solution obtained with ANSYS Fluent.

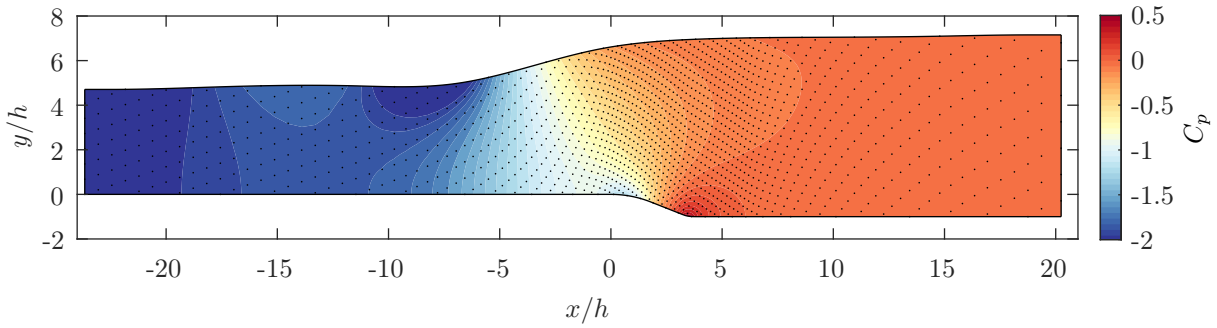

Figure 3.10: Inviscid 2D static pressure coefficient C_p solution with every tenth FEM mesh node shown.

Solution of the Laplace equation yields potential values Φ at the grid nodes. To obtain velocity components and then pressure through the Euler-Bernoulli equation the gradient of Φ is numerically determined. The mesh is not Cartesian but it is structured so there exists a $R^2 \rightarrow R^2$ mapping of the x, y space into the p, q mesh space, which is defined such that p increases by 1 with each column to the right and q with each row upwards. The Jacobian of this mapping is determined using central differencing for internal points and forward/backward differences at the edges. The potential gradient is likewise determined in mesh coordinates and then transformed to x, y coordinates using the calculated Jacobian to obtain U_x and U_y as given by expression 3.5.

$$\begin{bmatrix}\Phi_x\\ \Phi_y\end{bmatrix} = \begin{bmatrix}p_x & q_x\\ p_y & q_y\end{bmatrix}\begin{bmatrix}\Phi_p\\ \Phi_q\end{bmatrix} \tag{3.5}$$

3.3. Static wall pressure measurements

Prior to detailed flow characterization using PIV and hot wire measurements, a preliminary investigation of the control parameter space was performed with the intent of finding operating points of interest. The results of this are covered in chapter 4. To enable this, a quick method of assessing the control effect was developed based on its effect on the static pressure distribution for which static pressure measurements were taken along the bottom tunnel wall. This section firstly details the pressure measurement system, including the Prandtl-Pitot tube with which the reference tunnel velocity was measured. Following that the baseline pressure measurements are presented and a control effectiveness metric is developed.

3.3.1. Experimental set-up and procedures

The distribution of pressure taps along the bottom wall and the position of the Prandtl-Pitot tube within the tunnel are shown in figure 3.4. There were 14 pressure taps drilled along the ramp, 7 in the curved section and 7 in the flat inclined plate. Both groups of taps were spaced equidistantly along the ramp surface, those in the curved section with 15mm between them and those in the flat inclined section with 10mm. Both were positioned slightly off the tunnel symmetry plane, such that they would not interfere with the streamwise wall-normal PIV plane, for which non-reflective tape would be added on the ramp. Furthermore, there were 8 pressure taps in the flat upstream section of the tunnel and 8 in the downstream section, also positioned off the tunnel symmetry plane.

The pressure taps are 0.3mm holes in the tunnel wall, connected by 1.5-2m of flexible tubing to a NUB 160 Pa pressure scanner. Each scanner had 16 ports, so two scanners had to be used for the 30 taps in total. The remaining 2 ports were used to connect the static and total lines of the Prandtl-Pitot tube set above the ramp. Due to the inertia of the air column within these long tubes, the system is unable to temporally resolve the pressure fluctuations in the tunnel and is used exclusively to determine time averages.

The scanner measures the pressure difference between the connected pressure tap and a reference pressure. In this case all of the reference ports were left open to the atmosphere such that the scanner readings are the gauge pressures of each connected line. The scanner was placed under the test section to minimize the length of the connecting tubes, which unfortunately put it into airflow diverted under the section by the deflector panel installed on the lower contraction rim. To minimize the effect of this flow on the reference ports, the scanner was wrapped in multiple thick blankets.

Taking as reference values those at the exit of the test section, where the static pressure is equal to ambient atmospheric, the static pressure coefficient was simply determined as

$$C_p = \frac{p_m}{p_{m,t}} \tag{3.6}$$

where p_m is the static gauge pressure measurement, while $p_{m,t}$ is the total gauge pressure measurement obtained from the Prandtl-Pitot tube. The latter is equal to the dynamic pressure at the exit of the tunnel under the assumption that the Prandtl-Pitot tube is positioned within the irrotational core flow and that within this core flow the total pressure remains constant.

3.3.2. Baseline measurements

The measured static pressure along the tunnel wall for the uncontrolled case is shown in figure 3.11, along with the calculated inviscid solution. By design, the boundary layers in this test section grow extremely thick with respect to the cross-section, which leads to a significant displacement effect on the irrotational core flow and ultimately to the large difference between the viscous and inviscid pressure distributions. The effective area expansion ratio of the tunnel is reduced which greatly decreases the overall pressure ratio. The ramp is effectively "decambered", reducing streamline curvature and the depth of its suction peak. And finally, the adverse pressure gradient triggers separation at the foot of the ramp, which is measured here as a region in which the static pressure rise is temporarily halted. Note also that the density of pressure taps is insufficient in the upstream and downstream flat tunnel sections near the ramp to resolve the still high pressure gradients.

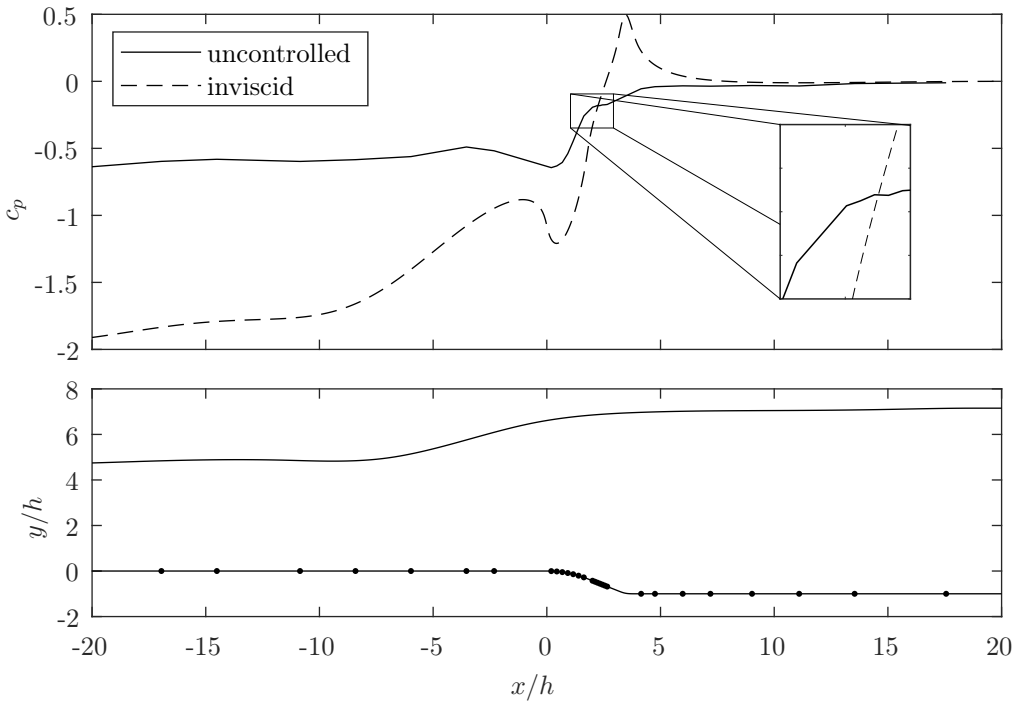

Figure 3.11: Static pressure coefficient along the bottom wall of the test section (*top*) and lower and upper tunnel wall contours with pressure tap locations marked (*bottom*).

Pressure recovery is first driven by the contour of the ceiling and begins at approximately $x/h = -10$. The recovery isn't monotonic as the convex curvature of the ramp first causes a localized suction peak on the bottom wall and then an even steeper pressure gradient due to the local flow area expansion and the convex curvature between the ramp and the downstream tunnel section. A pressure recovery that occurs in two stages with a localized suction peak inbetween is commonly encountered. Most notably this is found in the case of deflected flaps or morphing wings, where there is a "global" pressure recovery from the wing angle of attack, a local bubble of suction due to high curvature at the location where the wing is deformed and then an even higher adverse pressure gradient following the low pressure bubble.

3.3.3. Control effectiveness metric

With the measurement system in place, performing parametric control sweeps of actuation momentum and frequency required a suitable metric, derived from the static pressure readings at the wall, that would give an indication of control effectiveness. For example, if a wing was being studied, then a key performance indicator of control would be the efficiency L/D, whereas for a bluff body with a wake, the main indicator would be the drag coefficient C_D. Ultimately, all of these metrics including the ones given above boil down to the amount of viscous losses present in the system.

As an attempt to quantify these viscous losses, the metric selected for the present case compares the measured pressure distribution with that which would be established if the flow within the tunnel was inviscid, or essentially equal to the solution given in figure 3.10. It is argued that as a separation control system transfers momentum towards the wall, its most fundamental effect on the flowfield is in making it more similar to an inviscid flow with the same geometric boundary conditions. As the momentum deficit of the BL is decreased, the viscous displacement boundary condition applied to the equivalent inviscid flow tends to zero and the real viscous flow tends to a purely inviscid flow with the same geometric BCs.

Note from figure 3.11 that upstream of a certain point the inviscid pressure is lower than the real pressure and higher downstream. As the boundary layer momentum deficit is decreased by the actuator, the accompanying reduction in displacement thickness is expected to decrease the difference between the pressure distributions. The metric, which is termed M_p, is therefore defined as the integrated difference between the measured pressure distribution and the calculated inviscid pressure distribution at the wall,

as given by equation 3.7.

$$M_p = \int_{s_1}^{s_2} |c_p - c_{p,i}| ds/h \tag{3.7}$$

where s is the streamwise coordinate which runs along the wall. The density of pressure taps is only sufficient to resolve the pressure gradients properly along the ramp itself. As mentioned, just upstream and downstream of the ramp there are still quite sensitive regions with high pressure gradients, which remain unresolved. For this reason, the integration of the metric is carried out from the first to the last pressure tap on the ramp ($s_1/h = 0.1$ to $s_2/h = 4.1$), excluding the long upstream and downstream development sections. Naturally, since the pressure distribution is measured in discrete points, the integration is carried out numerically, using the trapezoidal rule.

Finally, to measure this metric a measurement time had to be decided. Convergence plots for a single reading of the final ramp pressure tap and the integral metric M_p are given in figure 3.12. While the measurements look fully converged with measurements of $t > 300$ s, note the scale and the fact that even with a low measurement time of 15 s, both measurements are already well within 1% of the final converged value. If experimental time was unlimited, then a conservative approach would have been taken and each point acquired for 300s but this was not the case so the acquisition times were reduced as much as possible while still resolving clear trends in the data. Two sweeps were performed, of actuation momentum and frequency. For the momentum sweep (section 4.2) acquisition times of 60 s per data point were found to be sufficient while for the frequency sweep (section 4.3) they were increased to 120 s which still left noise in the data but was enough to produce clear trends.

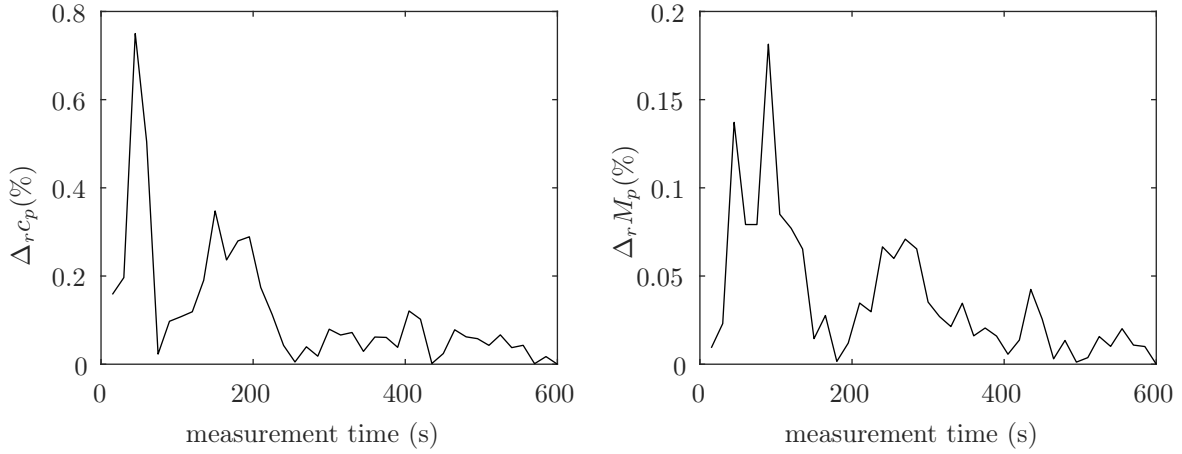

Figure 3.12: Static pressure measurement convergence for the case of 3D1 actuation at $f = 27.78$ Hz: (*left*) last pressure tap of ramp and (*right*) control performance metric M_p.

3.4. Particle Image Velocimetry

Two-dimensional two-component (2D-2C) PIV was used to obtain velocity fields in two different planes. This was used to characterize the size, shape and unsteady modes of the separation bubble as well as the flow structures produced by the jet crossflow interaction responsible for separation suppression.

3.4.1. Working principles

2D-2C PIV yields two velocity components along a plane. To do this, tracer particles are introduced into the flow and illuminated in the plane of interest at two close time instants by a laser pulse which is formed into a sheet by an optical system. The tracer particles scatter this light and a camera, synchronized to the laser, acquires images of the illuminated plane in the two pulses. The difference between the two acquired images will be that the particles imaged in the domain have moved by a certain $\Delta\mathbf{x}$, which together with the pulse separation time Δt will yield particle velocities.

Important lens/camera parameters are the magnification M, focal length f, aperture D and the f-stop $f_\# = f/D$. These parameters need to be adapted to the case at hand. Firstly, the depth of field needs to be at least as thick as the laser sheet. Secondly, the particle images need to be of sufficient size.

The imaged particle diameter in pixels is given by

$$d_\tau = \sqrt{M^2 d_p^2 + (2.44(1+M)f_\# \lambda)^2} \tag{3.8}$$

where the first term is the physical particle size and the second term is the diffraction diameter which is independent of particle size. For small particles, as are generally used in studies involving air, diffraction is much more significant than their physical size. If d_τ is smaller than a single pixel, it's no longer possible to discern the particle position to less than pixel accuracy, a phenomenon called peak-locking. Ideally, the particles should be 2-3 pixels across in which case their diffraction pattern, given by the Airy function, can be approximated by a Gaussian and their position determined to sub-pixel accuracy as the location of the Gaussian peak.

To obtain the displacements from the acquired image pairs, a statistical technique of image cross-correlation is used. For this the images are divided into *interrogation windows* and for each window pair a cross-correlation is calculated. The position of the cross-correlation peak represents the *average displacement* of particles within this window. This displacement, determined in pixels, then has to be mapped to physical space based on the parameters of the camera and lens. This mapping includes a pure magnification and a distortion of the image due to defects in the equipment such as a tilted sensor. The exact mapping is determined by a calibration in which a calibration target with marked dimensions (generally millimeter paper on a flat plate) is imaged by the camera. With the displacements transformed to physical space, the velocity field is easily determined since the time separation of the two pulses is known.

To maximize the measurement resolution the interrogation windows have to be made as small as possible but that quickly runs into issues. Between pulses some particles move out of the interrogation window and new ones enter. This leads to non-phyical peaks in the cross-correlation map, decreasing the signal-to-noise. The way to increase resolution once the window can no longer be made smaller is to do the processing in multiple passes where the pair of interrogation windows is offset by the displacement determined in the previous pass prior to the computation of the correlation map. In subsequent passes the windows can then be made much smaller because they track the particles. Besides just translating the windows, they can also be deformed to further improve this tracking capability which is especially important for flows with high velocity gradients.

3.4.2. Imaging

Two PIV planes were imaged:

- Plane 1 - wall normal streamwise (xy),
- Plane 2 - wall "parallel" spanwise (x^*z).

These are illustrated in a three-dimensional model of the ramp (figure 3.13) and on mean velocity fields acquired for the case of steady blowing (figure 3.14). Plane 1 is positioned at $z = -18.75$ mm to run exactly through one of the actuators closest to the tunnel centerline. As such it provides information about the actuation jet trajectory as well as the BL velocity profiles, location of detachment and reattachment points and the size and shape of the separation bubble. If a purely 2D flowfield was being studied, plane 1 would be sufficient to completely characterize the flowfield, but given the 3D nature of the applied actuation, this is not the case and a spanwise plane is necessary to obtain information about the spanwise flow variation.

Given the curved nature of the ramp, the position of plane 2 is ofcourse not actually wall-parallel but from initial velocity fields acquired in plane 1 it was positioned to run approximately along the flow streamlines in the region approaching and just past detachment. This is where the largest separation delay effects are measured and was thus of biggest interest. A wall "parallel" plane is selected over a wall normal one because it runs along the main convection vector of the flow and thus gives information on the streamwise development of the applied perturbation. Because of the large streamwise gradients, this is considered more important for the assessment of control performance than a full snapshot at one streamwise location.

The coordinate system of plane 2 is denoted by x^*y^*z and its origin is at the intersection of $z = 0$ and the upstream edge of plane 2. The results suggested that the largest angle between the mean flow direction and the direction of plane 2 was 10° and was seen for the uncontrolled case at the downstream edge of the plane. For controlled cases the flow turned more over the ramp and the out-of-plane component was reduced.

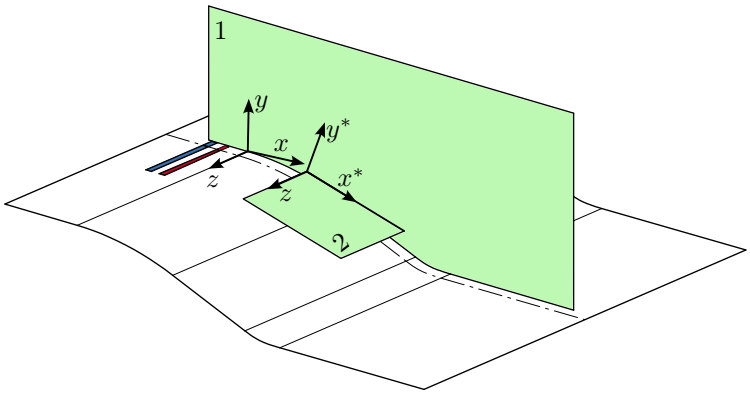

Figure 3.13: Three-dimensional illustration of the PIV plane positions in relation to ramp geometry with marked coordinate systems.

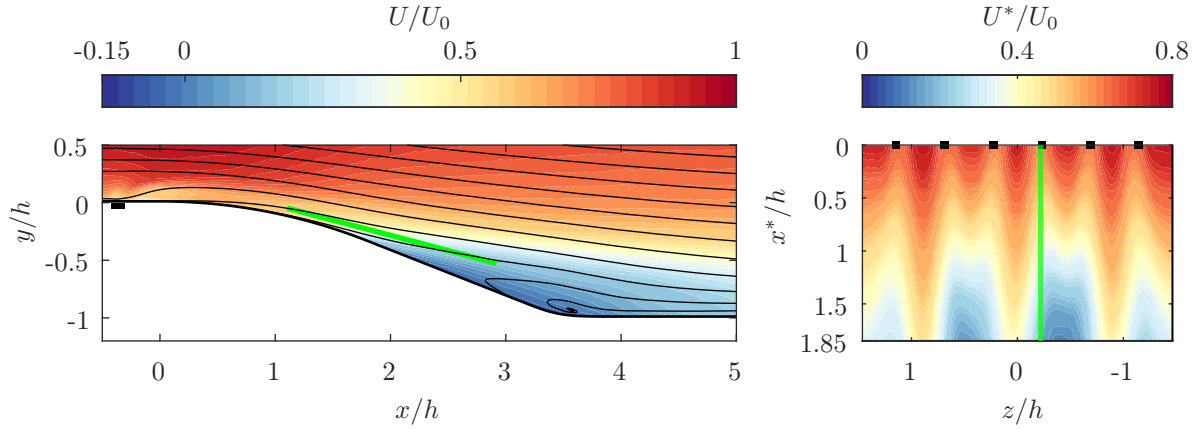

Figure 3.14: Position of the PIV planes (green lines) shown in the velocity fields for the case of steady blowing.

3.4.3. Set-up

The camera and laser set-ups that enabled the imaging of these planes are shown in figure 3.15. For plane 1, the laser was positioned downstream of the tunnel entrance and 2 cameras, positioned side by side to increase the field of view, were located beside the test section and pointed in the $-z$ direction. In the case of plane 2, the laser was positioned where the cameras were placed for plane 1 and the laser sheet formed in the $-z$ direction with the required tilt angle. A single camera, was fixed above the tunnel looking down perpendicularly to the imaging plane. The angle was set using an inclinometer to minimize the angular deviation of the focal and imaging plane. The downstream edge of the FOV of plane 2 was limited by test section construction elements but as shown in figure 3.14, the area of separation delay was satisfactorily captured. In both cases, black non-reflective tape was used across the ramp to minimize reflections (see photo 3.5b) and the surface of the ramp thoroughly cleaned with ethanol before every acquisition.

All of the image acquisition and processing was carried out in LaVision's DaVis 10.2 PIV software. The cameras used were LaVision sCMOS 2560x2160 pixel resolution cameras equipped with Nikon 60mm lenses for both planes. The laser used was a Quantel Evergreen Nd:YAG. The laser sheet was formed using an optical arrangement of a diverging and converging lens to form the beam waist followed by a mirror to turn the beam through 90 degrees and a cylindrical lens to open it up into a sheet. Qualitatively the same optical set-up was used for both planes, but lenses with different focal lengths were used due to the area of interest being at different distances from the laser. The sheet thickness was adjusted to be on average 1 mm through the camera FOV. Using a mirror to turn the beam makes adjustment of the sheet direction easier and in the case of plane 1 reduces blockage at the tunnel

exit which is good for repeatability. Finally, the flow seeding was provided by a SAFEX fog generator operating in the fan chamber of the wind tunnel and running on a glycol-water solution generating particles with a mean diameter of 1-3 μm.

Custom calibration targets were made for both planes, enabling not only camera calibration but laser sheet positioning. With plane 2 the laser sheet positioning was more of a challenge, because the high velocity gradients in the wall normal direction make the acquired velocity fields very sensitive to vertical offsets or plane tilt. Every care was taken to minimize tilt during set-up but a small tilt remained, noted as a slight asymmetry in the uncontrolled flow velocity field which should have been fully symmetric. The asymmetry in velocity between the two edges of the plane indicates that the sheet rises slightly in the $-z$ direction and is $< 5\%$ which is satisfactory.

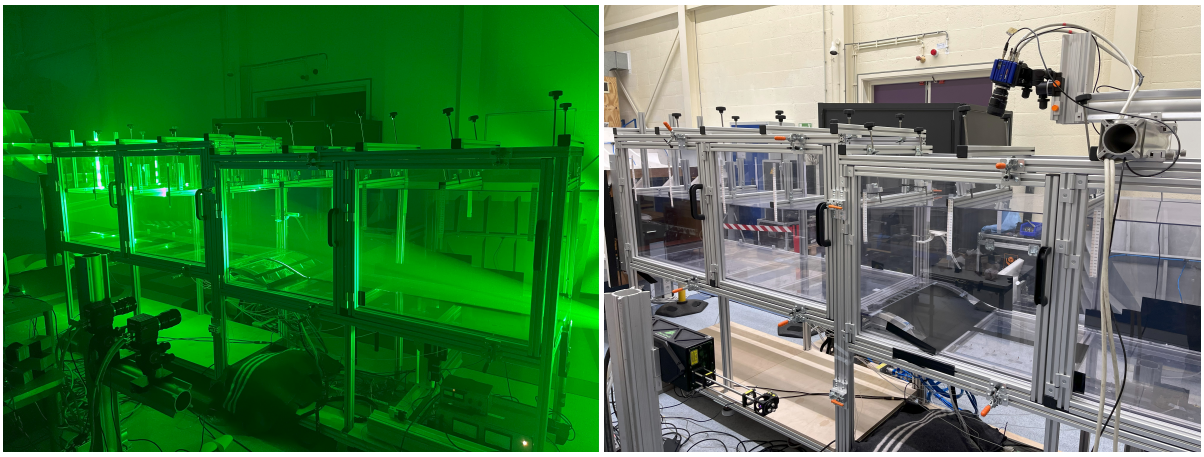

(a) **(b)**

Figure 3.15: Photos of PIV laser and camera set-ups for (a) plane 1 and (b) plane 2.

Initial PIV acquisitions were performed for both planes to set the camera focus and aperture settings, the pulse spacing dt and to assess the best particle image density. In both cases the same camera and lens were used and they were similarly far away from the imaged plane so these parameters ended up being similar. The planes were relatively far from the camera and so the particles were dim necessitating in both cases the aperture to be set to $f_{\#} = 5.6$ to increase the amount of light acquired. Furthermore, with a perfectly in-focus plane the imaged particle diameters were of sub-pixel size which led to peak-locking. To fix this, the cameras were intentionally slightly defocused to achieve imaged particle diameters of the order of 3 pixels such that sub-pixel interpolation could be effectively carried out in post-processing. The imaged separating flow has a high dynamic range because by definition there are regions of the flow where the velocity is close to zero. To accurately determine velocity, a relatively high pulse spacing dt was therefore required and after some testing it was set to 120μs for both planes. The camera settings and the size of the field-of-view for both planes are given in table 3.2.

Two types of acquisitions were acquired in both planes: uncorrelated image sequences for all tested cases and phase-locked image sequences for the unsteady control cases. In the first the acquisition frequency was simply set to 15 Hz and the Programmable Timing Unit (PTU) synchronized the laser and camera triggers to acquire a prescribed number of images, independently of the flow control system operation. This was performed for all tested cases, with 3000 total images acquired per case in batches of 1500 such that the seeding could be replenished between batches. For unsteady control cases, it was important to make sure that the acquisition frequency was not a multiple of the actuation frequency as that would yield partly correlated datasets, biasing the time-average. The actuation frequencies were all non-round numbers due to the need to avoid timing jitter, so a 15 Hz acquisition frequency satisfied this requirement.

On the other hand, for the phase-locked acquisitions, biasing the data in this way was precisely the goal. The cRIO controller was connected to the PTU and the jet triggering signal, with a prescribed delay added, was used to trigger the acquisition of an image pair. Per point in the actuator phase, 1500 images were acquired. For the 3D1 SF, 3D1 BM and 3D2 BM cases, 3 phase-locked acquisitions were acquired at times in the period $t/T = 0, 1/6$ and $1/2$. The reference start time of an actuation period

was delayed by 1 ms compared to the actuator trigger signal because this is approximately the delay between the command to start the jet and a jet velocity actually being measured (see the actuator characterization 4.1). Time $t/T = 0$ is therefore the moment just before the jet fires, while $t/T = 1/2$ is the moment just before it shuts off (due to a 50% duty cycle). Time $t/T = 1/6$ was selected because for BM cases this is the moment just before the first pulse finishes and for SF cases it's still of interest to capture an earlier time in the jet firing in which the starting structures are more coherent. For 3D2 SF cases, there are effectively 2 alternating periods during which either row 1 or row 2 is firing. So for these cases, only two points for each of these periods (four in total) are acquired, namely $t/T = 0$ and $t/T = 1/2$.

3.4.4. Image processing

Before the cross-correlation procedure was carried out to determine velocity fields, the raw acquired images were first pre-processed to boost the signal-to-noise ratio. Firstly, the minimum intensity over a number of subsequent snapshots was subtracted from each individual pixel. This removes a large amount of background noise and stationary reflections. To further reduce noise, each individual image is split into windows of prescribed sizes and the minimum intensity within each window is subtracted from it. Together, these two steps remove most noise, leaving clear particle images. Finally, since the brightness of the image varies across it, image regions are localized by the local intensity, again according to prescribed window sizes. Additionally, since a large portion of the FOV in plane 1 is taken up by space below the ramp in which there is no flow, a polygonal mask was added to the images, excluding most of this region from processing and leaving just a thin stripe next to the wall such that it could be properly located in the velocity fields. The results of this processing strategy are shown in figure 3.16.

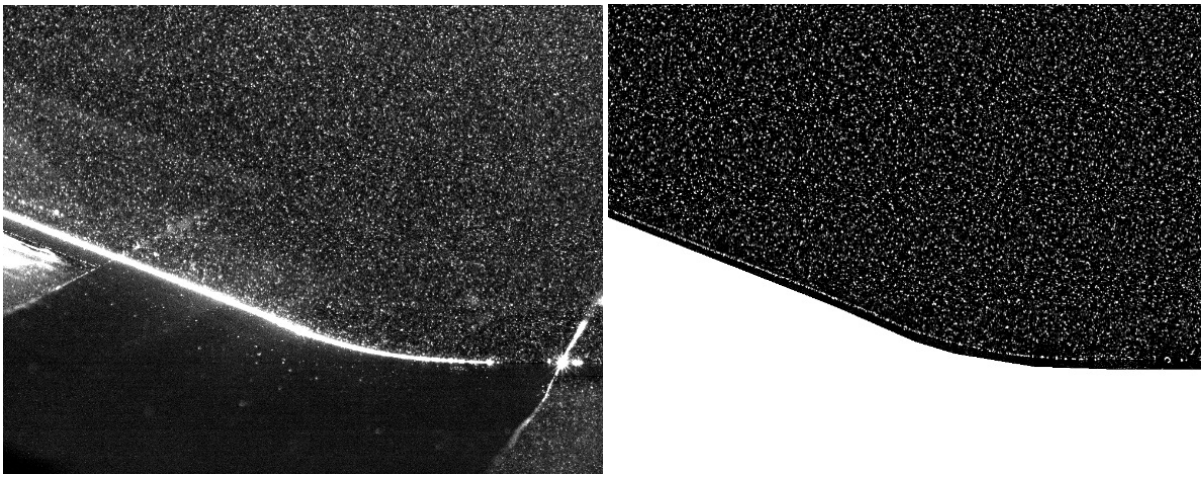

(a) **(b)**

Figure 3.16: Detail of PIV images in plane 1 before (a) and after (b) processing.

From the pre-processed images the velocity fields are obtained by the conventional cross-correlation PIV method utilizing a multi-pass procedure. The window size for the initial passes was set by relying on the adopted best practice of adopting a window 4 times larger than the largest particle displacement. The final window size was set empirically by reducing it until noise became significant at which point the size was increased by two levels for safety. A 50% overlap was adopted in all cases as well as an axisymmetric Gaussian weighting function. After each processing step, the universal outlier detection method was used to detect and remove outlier vectors. The filter region was set to 5x5px and vectors were removed if the normalized residual was > 2. The processing settings are summarized in table 3.2.

The convergence of the mean PIV velocity is shown in figure 3.17 for both components as a relative error with respect to the mean obtained with the maximum available number of samples. The point at which this is evaluated is in the shear layer region of maximum turbulent intensity where the slowest convergence is expected. The critical velocity component is the smaller V velocity and this converges after about 200 samples. The convergence of uncorrelated and phase-locked acquisitions is actually extremely similar which highlights the intensity of random turbulent fluctuation compared to the coherent

Plane	FoV	$f_\#$	dt	Initial passes	Final passes
1	500x250 mm	5.6	120 μs	2, 64x64px, 50%	2, 16x16px, 50%
2	210x150 mm	5.6	120 μs	2, 48x48px, 50%	2, 16x16px, 50%

Table 3.2: PIV velocity field imaging and processing settings. The processing pass parameters are given as: number of passes, window size and window overlap.

harmonic fluctuation caused by the actuator. In any case, there is a more than sufficient number of images for each case to achieve full convergence.

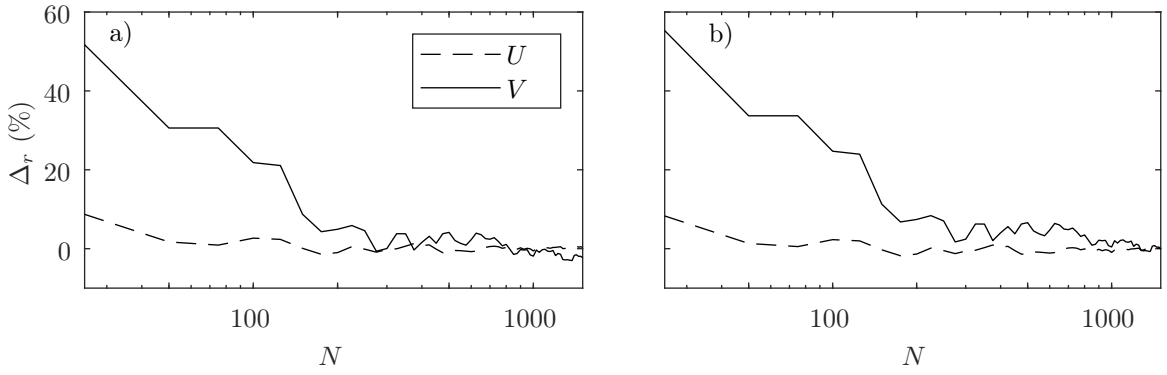

Figure 3.17: Convergence of PIV velocity components at point $x/h = 4.2$, $y/h = -0.6$ for (a) uncorrelated images and (b) phase-locked images for 3D1 LF forcing ($f = 27.78$ Hz).

3.4.5. Locating the planes and the wall

While the PIV planes were set-up as precisely as possible, there was still a fair bit of uncertainty left as the the actual location of the imaged plane. To fix this, the fact that two intersecting planes were imaged in the same conditions was leveraged to exactly determine their positions in the post-processing phase based on the fact that the same velocities should have been measured in both planes along their intersection, which can be seen marked as a thick black line in figure 3.13.

To achieve this a numerical optimization of the plane degrees of freedom was carried out with the objective of minimizing the integral difference between the two plane measurements of the velocity along the intersection. Firstly, the assumptions were that plane 1 was perfectly normal to the z axis leaving only its spanwise position as unknown. For plane 2, the only assumption was that it had no spanwise tilt, leaving it with 3 degrees of freedom. The velocity along the intersection was determined simply by interpolating the fields to the required coordinates and then projecting the resultant vectors the direction of the intersection. An initial estimate of the degrees of freedom was provided by physical measurements taken during set-up.

The degrees of freedom that were ignored for the optimization, such as the tilt of plane 1 around the y axis, were left out because the velocity measurements were far less sensitive to their variation, which would have caused issues in the optimization procedure without any significant benefits. As is, the result of the optimization procedure is a very convincing fit, shown in figure 3.18.

Another thing that had to be properly located on the PIV acquisitions of plane 1 was the tunnel wall. The usual method of using the particle wall reflections did not work because the reflections were not clear enough for the cross-correlation procedure to pick them up. So instead, the piecewise continuous ramp profile was manually fitted to stitched raw plane 1 images using the laser wall reflection as a reference (see figure 3.19).

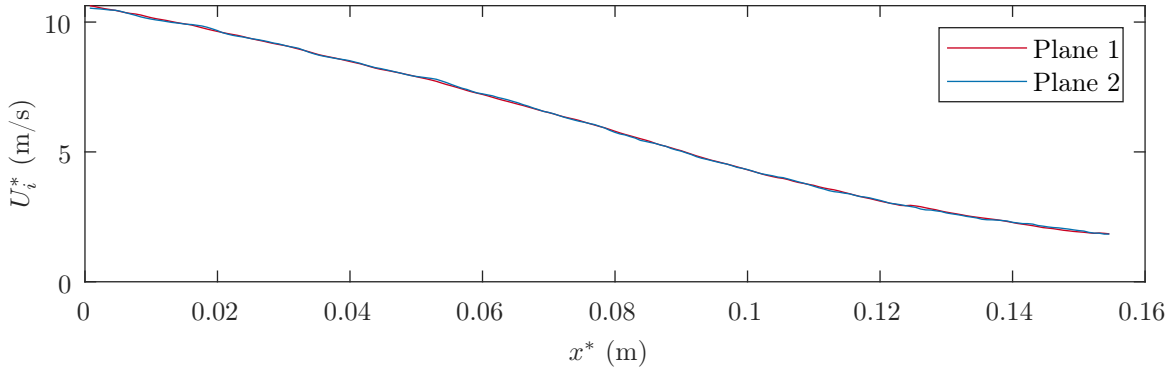

Figure 3.18: Velocity along intersection of PIV planes 1 and 2 measured in both planes after the location optimization procedure.

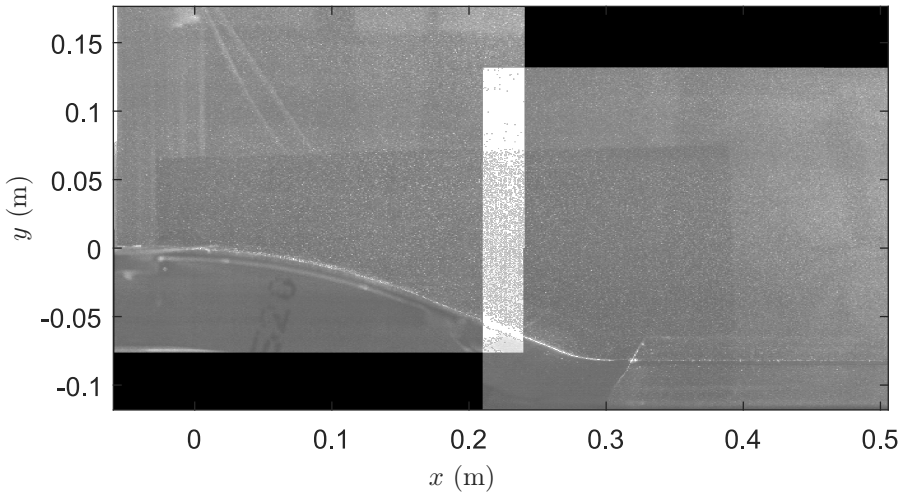

Figure 3.19: Raw stitched plane 1 images to which the ramp profile was fitted.

3.4.6. Determination of boundary layer parameters

Downstream of the start of the curved section, there are quite strong reflections present due to the laser shining at the wall, while upstream of it there is a thin near wall region which is shadowed due to the vertical position of the laser. In both cases the compromised regions are approximately 1.2 mm thick so a conservative estimate of vector validity would be $y \geq 2$ mm to account for bias in the crosscorrelation procedure. To account for this in the PIV analysis, the outlier data in this region are replaced by a quadratic fit which is zero at the wall and joins smoothly to the measured profile. For the analysis of the integral boundary layer parameters this is sufficient as this thin near wall region has very little overall impact on the integral boundary layer measures.

Attempts were made presently to determine the EIF of the tunnel flow by using the transpiration BC applied on the assembled FEM model to fit the flow measurements obtained with PIV. The wall-normal transpiration velocity on the lower tunnel wall and the ceiling was posed in the form of a curve with multiple free parameters $v_w(x, \alpha_i)$. These free parameters were then calculated by an iterative optimization procedure which aimed to minimize the difference between the calculated inviscid flow and the measured real flow in prescribed reference points. The chosen reference points ran along the top edge of the streamwise wall-normal PIV plane and were therefore quite far from the wall and within the irrotational core flow of the tunnel.

While the procedure was able to achieve good matches with the reference velocities, it did so by overfitting, yielding unphysical velocity profiles. The issues were two-fold. Firstly, the reference points were densely spaced along a very small part of the streamwise extent of the tunnel, when the transpiration

BC has strong influence both up and downstream. While the attempt was made to fix this by setting physical limits on the behaviour up and downstream based on common sense, the issue remained.

The second and more significant issue was that while the inviscid flow model was two-dimensional the actual flow turned out to be more three-dimensional than expected due to the narrow span of the tunnel, as is discussed in section 5.1. This means that a lot of the displacement effects on the velocity measured in the irrotational core flow are generated by the tunnel sidewalls and corner effects which is something that could never be mathched by a 2D model without it displaying unphysical overfitting behaviour.

In the end it was decided that the best approach would be to use the purely inviscid solution with no transpiration BCs scaled to match the top of the measured BL profiles as the EIF flow. The result of this procedure for two profiles just upstream of the ramp is shown in figure 3.20. Note how from the first profile to the second there is a significant change in the EIF profile related to the ramp suction peak. Although these profiles aren't the *exact* EIF profiles because the displacement BC hasn't been applied in their determination, it can be seen that towards the top of the measurement domain the profiles match very nicely both in slope and curvature. This is important because the flow outside of the boundary layer doesn't have a constant velocity, so if the approach of a constant inviscid reference velocity was used, the challenge would be to determine which one this was exactly.

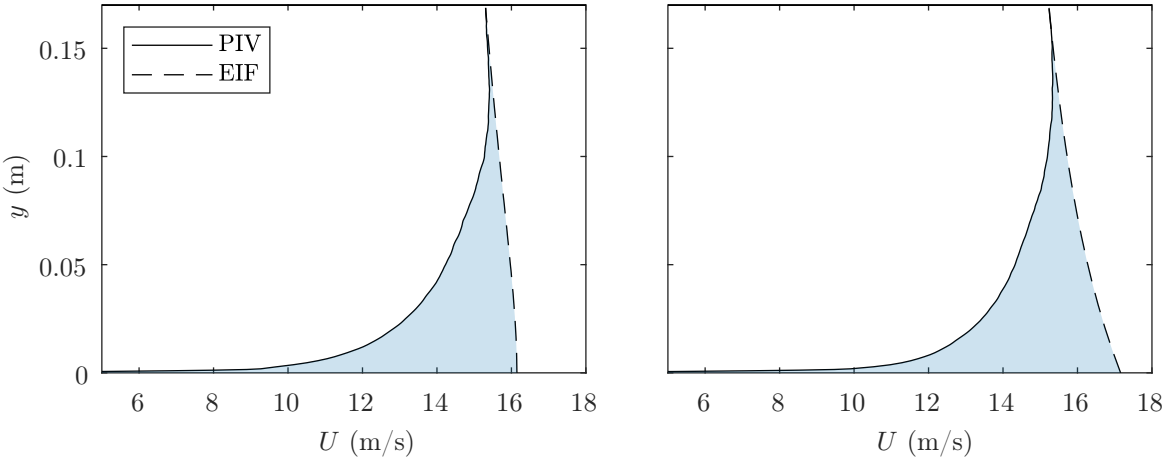

Figure 3.20: Measured PIV BL velocity profiles compared with EIF profiles at $x/h = -0.5$ (left) and $x/h = 0$ (right). Shaded area is the momentum defect.

3.4.7. Phase averaging

In the cases where the flow is actuated with an unsteady periodic perturbation, it is useful to extract from the flow fluctuation those features which are consistent across periods of actuation or in other words the harmonic flow component. As first proposed by Hussain and Reynolds 1970, the instantaneous velocity field can therefore be decomposed as

$$u = U + \tilde{u} + u' \tag{3.9}$$

where U is the mean velocity, $\tilde{u}$ is the harmonic fluctuation component and u' is the random fluctuation component. It can then be argued that this harmonic component is exclusively a consequence of actuation, while the remaining random fluctuation u' is due to turbulence.

The harmonic component is experimentally obtained by phase-averaging as given by 3.10, where T is the time period of the oscillation of interest.

$$\tilde{u}(t) = \lim_{N\to\infty} \frac{1}{N} \sum_{n=0}^{N} (u(t + nT) - U) \tag{3.10}$$

The first way in which the phase average is determined has already been mentioned and it is by phase-locking the PTU to the actuator controller. This yields exact results because each image is at exactly

the same phase. However, this requires a dedicated acquisition for each phase of interest which makes it impractical for sampling a large number of points in the period.

The second option is to use the unsynched image sequences and average those images which fall within a prescribed phase *bin*. Because the images are distributed across a non-finite phase interval, this approach results in some filtering of the results, depending on how wide the bins are. To do this, the time-in-period t/T of each acquired image needs to be known so both the actuator and laser control signals were acquired during the imaging runs in which the laser was simply running on the PTU clock at 15 Hz by a NI-dAQ board. These signals, a sample of which is shown in figure 3.21, were then processed yielding the t/T of each image. As is apparent from the unsteady control results presented in section 6.3, satisfactory results were achieved with the period split into 8 bins with widths of $\Delta t/T = 1/8$.

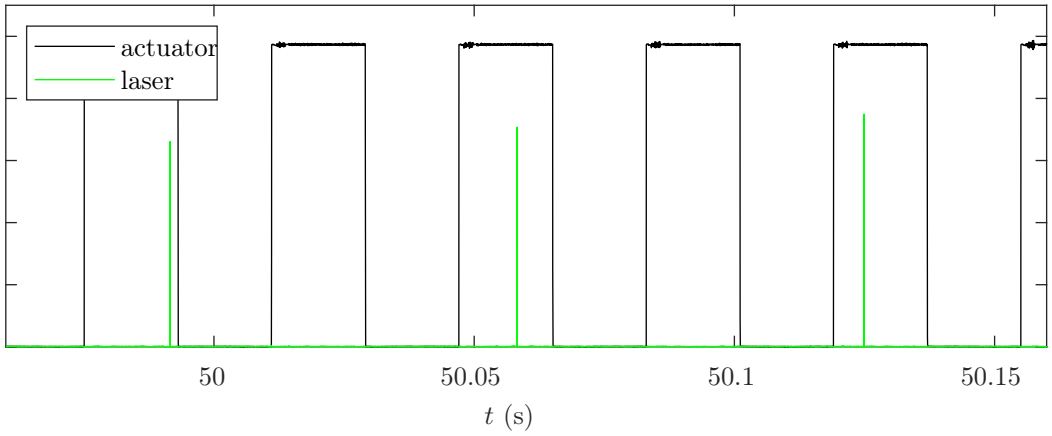

Figure 3.21: Sample of actuator and laser trigger signal acquisitions used for phase-averaging by binning.

3.4.8. Covariance and modal analysis

To extract information about coherent and energetic features in this highly turbulent flow, the statistical covariance of the velocity in different points and time instants is studied, directly and via modal decomposition, specifically *proper orthogonal decomposition*.

POD is a mathematical technique that extracts dominant patterns from a dataset, by representing high-dimensional data using a reduced set of orthogonal eigenfuctions. It is widely used in different fields and in fluid dynamics it is generally used to extract the most energetic coherent motions of the flow. A good reference for the application of POD and other modal analysis techniques in fluid dynamics is provided by Taira et al. 2017. All modal decomposition techniques involve representing the fluctuations of the velocity field as a linear combination of spatial modes Φ_j multiplied by temporal coefficients a_j as given by expression 3.11.

$$u(\mathbf{x}, t) - U(\mathbf{x}) = \sum_j a_j(t)\Phi_j(\mathbf{x}) \tag{3.11}$$

The part that differentiates between the different techniques techniques is how the decomposition is carried out.

In the case of POD, the modes result from a least-squares minimization of the difference between the modal decomposition and the actual data. A result of this is that with the same number of modes the POD decomposition can more accurately represent the data $u(\mathbf{x}, t)$ than any other modal decomposition. Mathematically, the modes and their energies are obtained as the eigenmodes and values of the covariance matrix of the data vector X, as given by 3.12.

$$XX^T\mathbf{\Phi}_j = \lambda_j\mathbf{\Phi}_j \tag{3.12}$$

The data vector X is an $m \times n$ matrix where the columns are vectors containing all velocity components in all measured points for a single snapshot.

Each plane 1 snapshot contains 147668 velocity vectors and there are 3000 snapshots for each case. The covariance matrix of the data vector would therefore be a square matrix with 9×10^{10} elements.

Performing an eigendecomposition of this matrix or even just storing it to memory is impractical. So the approach taken is instead to perform a *compact singular value decomposition* (SVD) of the X matrix. The SVD is mathematically equivalent to the definition of the POD. This decomposes the X matrix, as given by 3.13, into matrices Φ and Ψ whose columns are the eigenmodes and temporal coefficients for each mode respectively and the diagonal matrix $\sum$ which contains the singular values. The singular values are related to the eigenvalues of the covariance matrix as $\sigma_j^2 = \lambda_j$.

$$X = \Phi \sum \Psi^T \tag{3.13}$$

In the compact implementation of the SVD only those columns of Φ and Ψ corresponding to non-zero singular values are calculated. In this case the size of each snapshot vector is significantly larger than the number of snapshots so the compact approach saves a lot of time.

While the POD generally encodes the covariance of all of the measured data, it can also be useful to directly assess the covariance of a point in the flowfield with its surroundings. Specifically, this is used by many authors to establish the average size of coherent flow motions in a region of flow (Lee 2017; Wu et al. 2019). For example the normalized autocovariance of the fluctuating velocity component u' is given by expression 3.14.

$$R_{uu}(\Delta\mathbf{x}) = \frac{u'(\mathbf{x})u'(\mathbf{x}+\Delta\mathbf{x})}{u'(\mathbf{x})u'(\mathbf{x})} \tag{3.14}$$

At point $\mathbf{x}$ it will be a maximum of 1 and then generally it falls of with increasing $\Delta\mathbf{x}$. The size and shape of the region of high covariance can then be used to infer the size and shape of the average coherent structures present in the flow at point $\mathbf{x}$.

3.5. Hot wire anemometry

A constant temperature hot wire anemometer mounted on a precision traversing system is used for actuator characterization in quiescent flow surroundings and, along with PIV measurements, for baseline uncontrolled flow characterization. This section briefly covers the working principles of HWA and then describes how it was used in this research.

3.5.1. Working principles

The thin wire probe is continuously heated by an electrical circuit and placed in the flow. As the flow cools the wire, a Wheatstone bridge adjusts the voltage across the wire and thus the current flowing through it to keep it at a constant temperature. Based on the voltage applied E, the flow velocity U can be obtained from King's law 3.15, where the constants A, B and n are obtained by calibration.

$$E^2 = A + BU^n \tag{3.15}$$

Because the wire is exceedingly thin, its thermal inertia and consequently the response time of the bridge voltage to a change in flow velocity are very low so measurements can be acquired at very high frequencies. In the present study the system used is run at an acquisition frequency of 51.2 kHz thus enabling the sampling of signals up to 25.6 kHz. Furthermore, the probe measurement volume is very small so if the wire is able to be precisely positioned, then its spatial resolution and accuracy are also very good. HWA is therefore able to fill in the shortcomings of the utilized low acqusition rate PIV set-up in the characterization of the baseline uncontrolled flow. Firstly, it allows small characteristic flow time-scales to be resolved. Secondly, when mounted on a precise traversing system, it is able to accurately sample inner/overlap layers of the BL, which reflections prevent PIV from doing in this case.

Two different HW probes were used: a Dantec 55P15 boundary layer probe for the boundary layer and separation bubble measurements and a Dantec 55P11 conventional probe for the actuator characterization measurements. These were connected to an IFA 300 constant temperature anemomemeter.

3.5.2. Actuator characterization

For the actuator characterization a conventional Dantec 55P11 probe was mounted on a straight thin holder and positioned vertically above the actuator jet orifice as shown in figure 3.22a. This mounting position presents the least blockage to the jet and is therefore the least intrusive. The holder was further mounted onto a beam which was secured to a two-stage, computer controlled Zaber traverse.

The actuator characterization was carried out with the test section outside of the wind-tunnel so the calibration was performed using a calibrator (see figure 3.22b). The calibrator is connected to a pressurized air supply and has a large volume chamber ending with a smooth convergent nozzle. A differential pressure transducer is connected to the chamber and reads the gauge pressure $p_{m,c}$ within it. From that the calibration jet velocity follows as

$$U = \sqrt{2\frac{p_{m,c}}{\rho}} \tag{3.16}$$

where the density ρ is found from the ideal gas law and ambient pressure and temperature readings. This assumes that the velocity in the large pressurized chamber is negligible compared to the velocity at the orifice.

After the wire is heated to operating temperature the voltage readings are scaled such that the minimum to maximum measurement velocity corresponds to -5 to +5 V. Then voltage readings corresponding to 17 different velocities covering the specified range are taken and a 5th order polynomial is fitted to the readings. For the actuator characterization the calibration was performed for a velocity range from 0 to 40m/s.

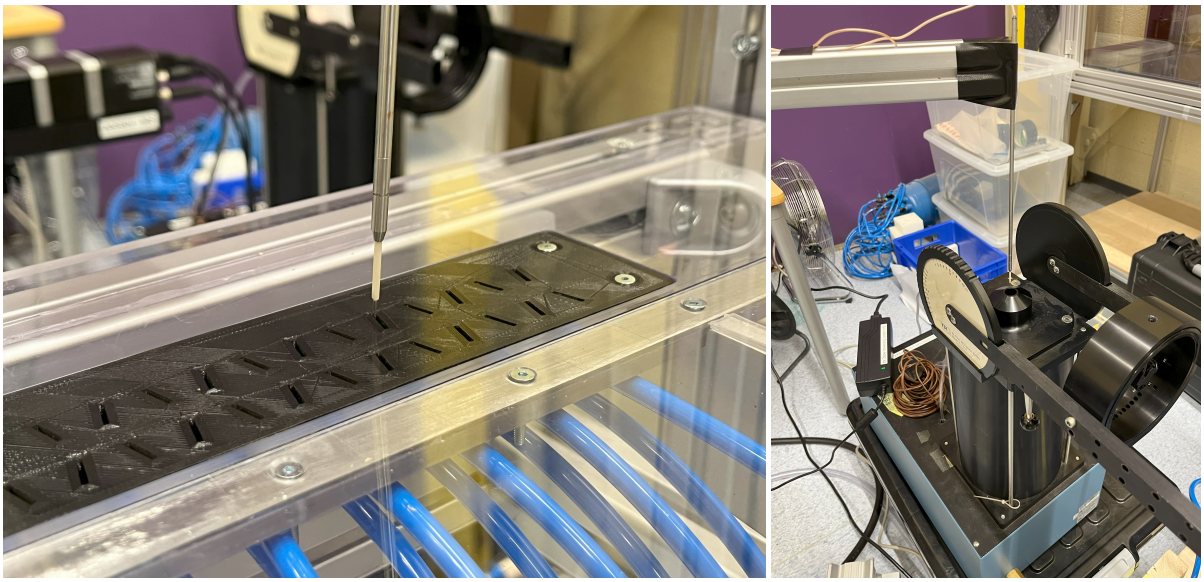

(a) **(b)**

Figure 3.22: Hot wire anemometry for jet actuator characterization: (a) acquisition, (b) calibration.

3.5.3. Boundary layer and separation bubble measurements

For HW measurements in the wind-tunnel test section, a Dantec 55P15 boundary layer probe was used, which has a kinked shape that allows it to be positioned very close to the wall. The probe was mounted on a long streamlined sting attached to the Zaber traverse via a flat steel plate. Since the ramp is approximately in the middle of this quite long test section, there was no way to reach it with the probe from the exit of the section so a floor plate in the downstream section of the tunnel had to be removed allowing access for the sting. The probe was positioned in the tunnel plane of symmetry and the sting aligned with the flow. The set-up is shown in figure 3.23.

The same calibration procedure is followed as in the case of actuator characterization, except that it was carried out in the wind tunnel rather than by using the calibrator. The probe was raised up to the level of the Prandtl-Pitot tube and then voltage measurements were taken for 17 tunnel velocities from 0 to 16 m/s and subsequently fitted.

Two groups of acquisitions were taken. Firstly, the boundary layer upstream of the ramp was traversed. Time-series of 150 s were taken in 40 logarithmically spaced points between $y = 0.25$ mm and $y = 90$ mm. To position the wire at 0.25 mm from the wall a positioning telescope (shown in figure 3.23) was used. The lens of the telescope can be very finely translated with an accuracy of 0.02 mm. The

wire is lowered slowly using the traversing system until it's close to the wall and within the telescope FOV. Visible on the telescope are then the wire and the wire reflection in the wall. By measuring and halving the distance between the wire and the reflection, the wall-normal distance is obtained and can be adjusted until the planned value is achieved.

For the measurement of the separated shear layer velocity fluctuations, the same equipment and set-up was used, apart from the positioning telescope because an extremely accurate wall-normal position was not as important. Before measurements were taken, preliminary PIV acquisitions in plane 1 were used to decide on the measurement point distribution. According to that, hot-wire time-series were taken in 32 points, arrayed in 4 vertical profiles positioned at $x = 0$, 0.26, 0.6 and 1 of the mean backflow region length, as shown in figure 3.24. The streamwise spacing of the profiles is motivated by the expected $1/x$ drop in shear layer natural frequency, which requires denser spacing upstream to capture the same change in natural frequency. The vertical spacing of the points is linear and the first point away from the wall is 5mm distant from it. The acquisition time for each point was 120s.

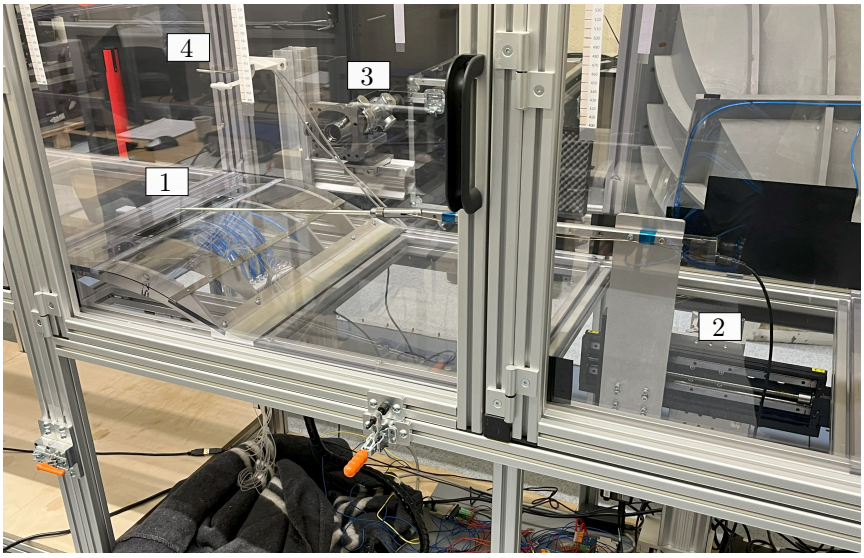

Figure 3.23: Hot wire anemometry set-up for measurement of the BL upstream of the ramp. Marked are the probe (1), traverse (2), positioning telescope (3) and the Prandtl-Pitot tube (4).

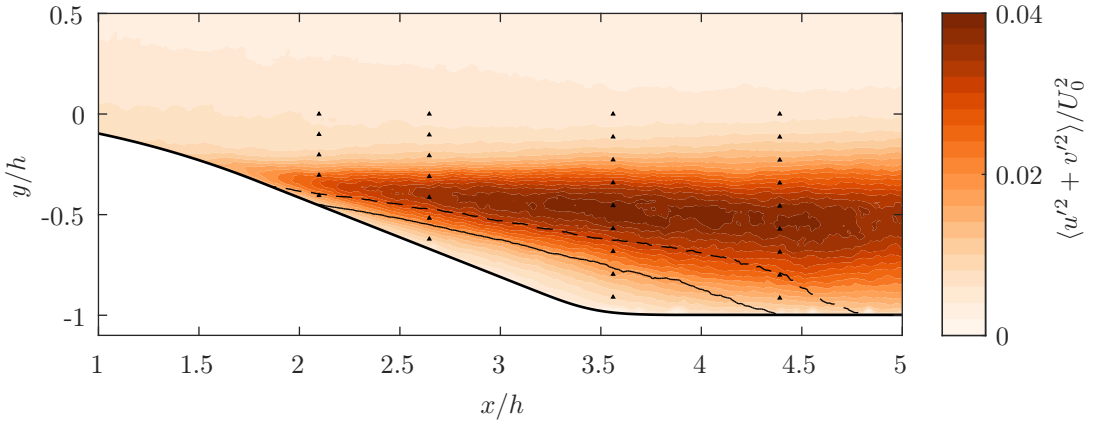

Figure 3.24: Spatial distribution of shear layer hot-wire acquisition points (▲) colored by turbulent kinetic energy. Contour lines: backflow coefficient $\chi = 0.5$ (-) and $\chi = 0.2$ (- -).

4

Preliminary control investigation

This is the first chapter presenting experimental results, specifically those of preliminary control experiments. Firstly, the results of the actuator characterization are presented, the aim of which was to validate the variance in jet velocity across the actuator and to establish the time response of the jets and their usable frequency range. Subsequently, the results of separation control parametric sweeps of actuation momentum and frequency, based on the static pressure control efficacy metric M_p, are discussed and cases of interest selected for further in-depth analysis.

4.1. Actuator characterization in quiescent surroundings

To establish the deviation between the blowing velocity between the actuator orifices, the settling tank was adjusted for a nominal steady blowing velocity of 24 m/s and both rows were then traversed in the spanwise direction with a hot-wire. The wire was positioned at 3 mm above the actuator and moved at a velocity of 0.92mm/s. The measured velocity time series was then filtered by a moving average filter kernel with the width corresponding to a wire transit distance of 1 mm. Since the width of the jet orifices is slightly larger than this, this would ensure that the estimate of jet core velocity was valid. The result is shown in figure 4.1, where the velocity is normalized with the mean peak velocity of all the jets which is $\bar{U} = 23.7$ m/s.

The mean velocity of row 2 is 13% larger than that of row 1 indicating that the flow through cavity 2 experiences smaller hydraulic losses which is not surprising because the design of cavity 1 required more agressive turning of the flow due to volume constraints (see figure 3.8). Within the rows themselves, the variation in jet velocity is ±5% within row 1 and ±7% within row 2.

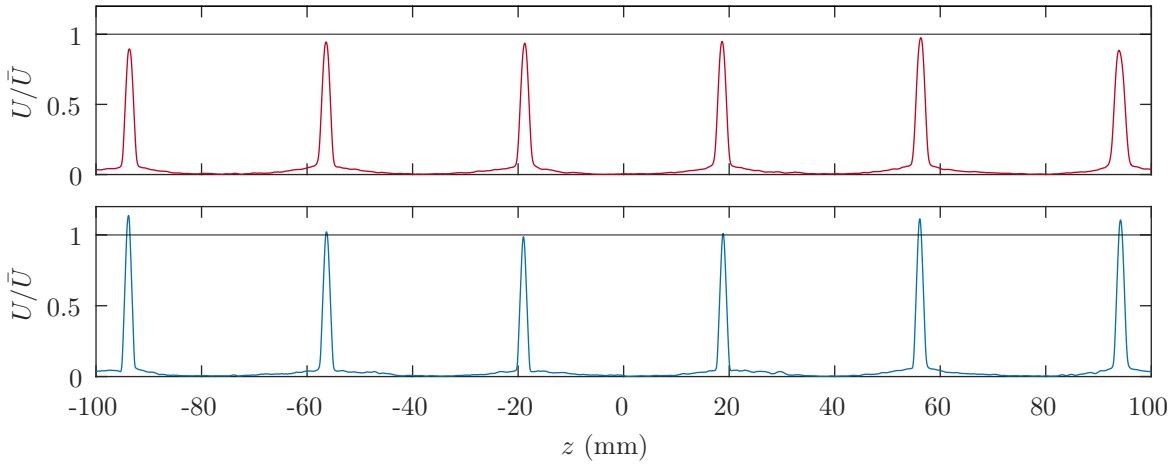

Figure 4.1: Spanwise hot-wire traverse velocity measurements of the 3D1 (*top*) and 3D2 (*bottom*) actuator rows normalized with the *overall* mean velocity and filtered with a 1mm moving mean filter.

The next stage of characterization focused on the transient response of the actuator, with the intent of establishing the characteristic timescales and usable frequency range. For this the hot-wire was positioned directly above the jet exit and actuator operated in steady operation and at frequencies from 5 to 333 Hz with a duty cycle of 50%. The acquisition time for each data point was 20 s with an acquisition rate of 51.2 kHz which allows for a precision in time-measurement of $\pm 10^{-2}$ ms.

The jet velocity is adjusted via the settling tank pressure regulator and it is this setting which is kept constant between cases. Since in all of the control experiments, the nominal jet velocity is set with the jet blowing steadily, this steady data point is acquired to provide a baseline velocity U_s against which the unsteady cases can be compared. Figure 4.2 shows an ensemble averaged period for both actuator cavity types. This data was obtained by phase-averaging 300 periods of actuation at a frequency of 15 Hz.

The opening signal is sent to the valve at time $t = 0$ ms and the closing signal at $t = 33$ ms. After an initial delay time, which includes the valve response time and the acoustic propagation time from the valve to the jet orifice and a rapid rise, the jet velocity is initially quite unsteady. At $t = 10$ ms there is another pronounced spike in the velocity followed by a further rise in velocity which ultimately stabilizes around $t = 25$ m/s. The spike at 10 ms is most likely a sign of the initial valve-opening expansion wave reflecting from the feed tank and now reaching the orifice, given the time is approximately equal to the time required for the round-trip at the speed of sound. Once the valve is shut off the velocity decays exponentially, experiencing another rebound in the process.

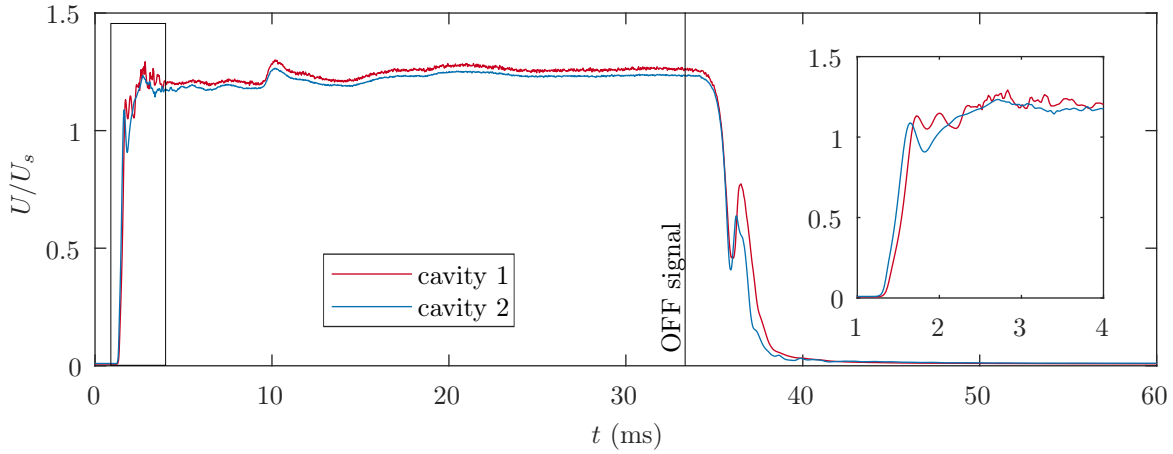

Figure 4.2: Time response of actuator jet exit velocity: average of 200 periods with actuator running at a frequency of 5 Hz.

The characteristic times for both cavity types are given in table 4.1. The start-up time τ_s is measured from $t = 0$ to when the jet velocity reaches $U/U_s = 1$, while the decay time is measured from $t = 33$ ms to when the jet velocity drops to $U/U_s = 0.1$. Interestingly, cavity 2 has a slightly faster response overall, despite having a larger chamber volume. This could be because the its flow path is less twisted overall than that of cavity 1.

Cavity	delay time τ_d (ms)	start-up time τ_s (ms)	decay time τ_r (ms)
1	1.25	1.66	5.1
2	1.25	1.60	4.6

Table 4.1: Actuator operating parameters for steady, single frequency and burst modulated actuation.

Another thing to note here is that the jet velocity, prior to shut-off, stabilizes at a higher velocity than U_s. The reason this happens is that the flow rate through the pressure regulator of the tank is dependent on the pressure in the tank. So when the actuator is commanded to drive a higher flow rate it will do so at a lower velocity because the pressure in the tank will drop until the regulator is able to supply the required flow rate. The time-scale in which this happens is longer than the frequencies

at which the actuator is driven so an unsteady actuation with a 50% duty cycle results in a higher jet velocity because the average flow rate is nominally half that of the steady blowing case.

Figure 4.3 shows how the effective blowing, mean and minimum velocity of the period change as the frequency is increased. The effective blowing velocity is the mean velocity achieved during the ON part of the period. At around $f = 100$ Hz, the jet pulse of the previous period does not have sufficient time to decay until the start-up of the following pulse and so the minimum jet velocity starts to rise quickly. This rise happens in two sudden phases, because the decay itself happens in two phases with a rebound in between them. The first velocity of note is 111 Hz at which the first sudden growth phase starts, which is slightly slower for cavity 2 because of its faster decay. The second phase starts approximately after 250 Hz.

As the decay takes up more of the period, the total actuation flow rate also increases which registers as an increase in mean velocity and leads to a decrease in maximum velocity because of previously explained mechanisms related to the feed system. Ultimately, with increasing frequency, the jet velocity experiences less oscillation and tends to a value only slightly lower than the blowing value, as the air in the system is unable to respond quickly enough to the switching of the valve. From these results it is apparent that a frequency of 111.11 Hz is the maximum actuation frequency at which the jets still have time to shut-off and is therefore an upper limit of the usable frequency range for the present requirements.

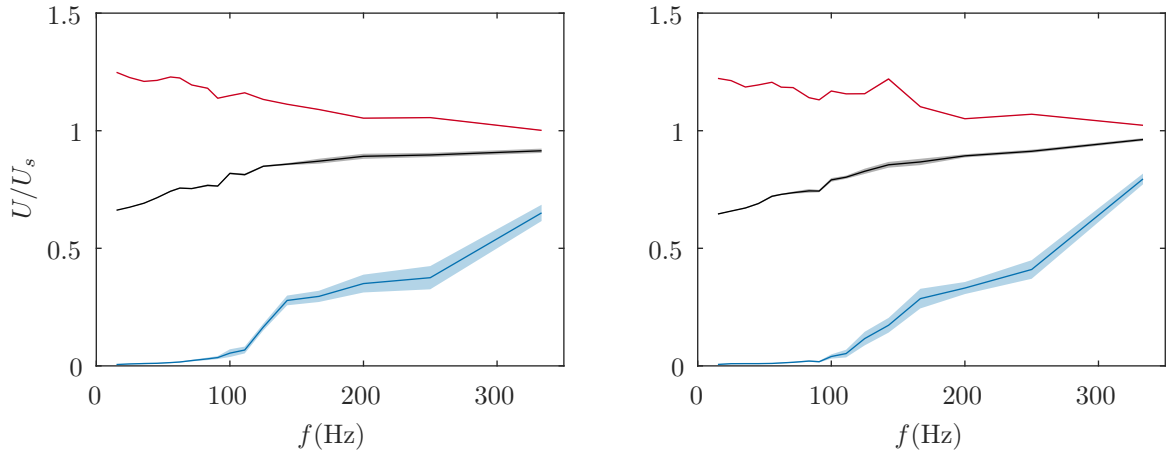

(a) 3D1 - Downstream row **(b)** 3D2 - Upstream row

Figure 4.3: Frequency response of the jet actuators. The top, middle and bottom lines represent the effective blowing, mean and minimum velocities of a blowing period and their standard deviations. The velocity is normalized with the steady state value U_s.

The preceding discussion shows that despite a nominal duty cycle of DC = 50%, the total actuator mass flux of unsteady blowing, while lower, is *not* exactly half that achieved in steady blowing, which is clear from the mean U/U_s given in figure 4.3. Firstly, this is because of the finite jet response times, which cause the "effective" duty cycle to increase with increasing frequency. Secondly, as already explained, the nature of the feed system is such that a lower mass flux will be accompanied by a higher tank pressure and consequently higher jet velocity. This means that even at low frequencies of actuation, when the effective duty cycle is approximately 50%, the mass flux is still higher than half of that achieved in steady blowing.

Besides the actuation mass flux, another variable of interest is the actuation mean momentum flux, given by expression 4.1 where the period is represented by T.

$$\langle U^2 \rangle = \frac{1}{T} \int_t^{t+T} U^2 dt^* \tag{4.1}$$

This value is important for the determination of the nominal actuator momentum coefficient. The ratio of the unsteady to the steady actuation momentum flux is shown in figure 4.4. It is approximately 80% in the range of usable frequency values, for both cavities.

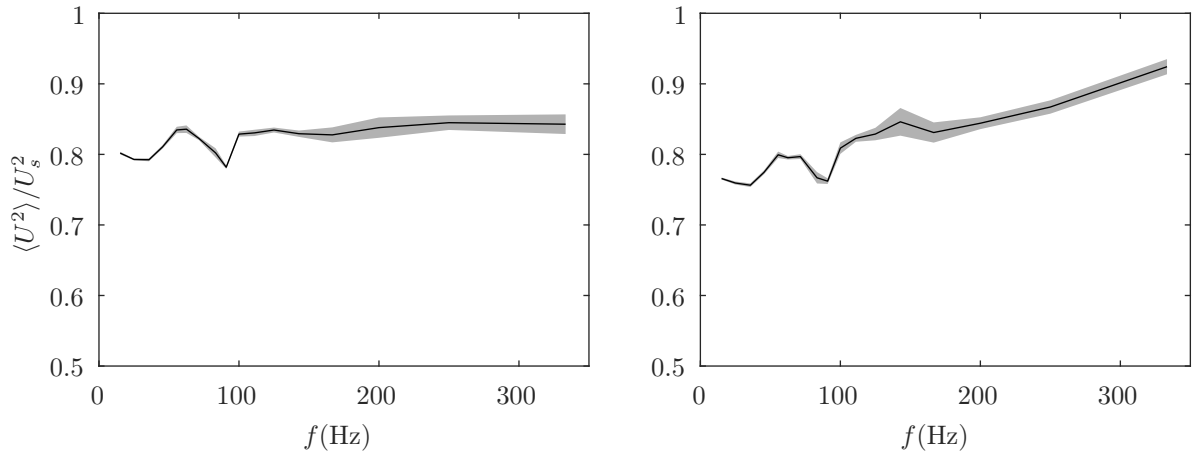

(a) 3D1 - Downstream row

(b) 3D2 - Upstream row

Figure 4.4: Mean momentum flux of unsteady blowing depending on frequency with 1 standard deviation marked.

4.2. Actuation momentum sweep

With the actuator characterized in quiescent surroundings now the focus is turned onto the preliminary separation control experiments, beginning with the actuation momentum sweep. The reference free-stream velocity was $U_0 = 15$ m/s. The sweep was performed with steady actuation using a single (downstream) row of actuators only, changing the velocity ratio VR from 0.4 to 2.4 in increments of 0.4. The jet velocity is set by regulating the feed pressure in the jet supply and using a small Pitot probe above the jet exit with no crossflow. This is important to keep in mind because the actual jet exit velocity during operation is unknown. What is cited in this work is therefore a *nominal* value. The actual value achieved with the tunnel running is affected firstly due to the interaction with the crossflow and secondly, because the static pressure just above the actuators is lower than atmospheric (see figure 3.11).

The resulting pressure distributions and the values of the metric M_p are shown in figure 4.5. For all cases, the metric is shown as the difference to the value of the metric in the uncontrolled case $M_{p,0}$. A negative ΔM_p therefore indicates a reduction in the extent of flow separation.

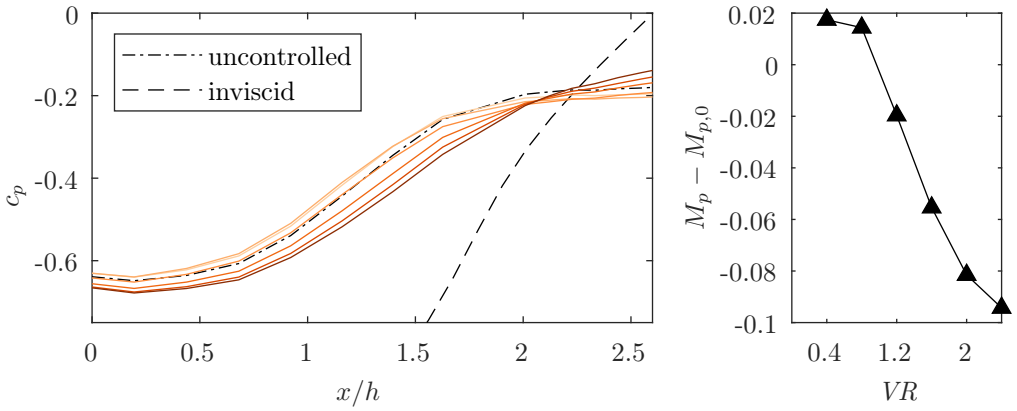

Figure 4.5: Control effectiveness actuation momentum sweep: (*Left*) static pressure coefficient profile comparison with lightest to darkest lines corresponding to the velocity ratio range from 0.4 to 2.4 in increments of 0.4 and (*Right*) difference in control effectiveness metric between actuated M_p and uncontrolled baseline $M_{p,0}$.

Actuation with $VR < 1$ reduces the depth of the ramp suction peak and the pressure in the separation

bubble, both of which are clear indicators that the extent of separation is increased. Only above $VR = 1$ does the control start having a positive effect. Given the lack of PIV at multiple VR, no explanation can be offered as to the reasons for this, but similar results have been observed in the case of round pitched VGJs (Selby et al. 1992).

As the size of the separation bubble is reduced along with its displacement effect on the flow, the pressure upstream drops as the flow curvature increases which is followed by a steeper recovery and increased pressure. The point around which this inversion of effect happens agrees very well with the crossing point of the uncontrolled and inviscid cases, which supports the choice of metric. Ultimately, there is an elimination of the constant pressure separated zone which doesn't mean that separation is completely eliminated, only that the bubble is reduced so much that it's no longer captured by the limited pressure taps.

For all further experiments a nominal $VR = 1.6$ was adopted given that this is, according to the data shown here, approximately at the inflection point in the trends where the improvements with increasing jet velocity start to diminish. To form the actuation momentum ratio C_μ, as discussed in section 2.2.1, the momentum deficit of the boundary layer to the equivalent inviscid flow at the actuator location is used as the reference crossflow momentum. The C_μ is therefore defined as given by 4.2, where $w_a = 6\lambda_j = 225$ mm is the width of the actuated span and A_j is the total area of the 6 jets.

$$C_\mu = \frac{U_j^2 A_j}{w_a \int_0^\delta (U_i^2 - U^2)\, dy} \tag{4.2}$$

In the current set-up, steady blowing at a velocity ratio of $VR = 1.6$ corresponds to a nominal momentum coefficient of $C_\mu = 0.023$. For reference and comparison to other studies, a commonly utilized C_μ definition is given by

$$C_\mu = \frac{U_j^2 A_j}{U_0^2 w_a \delta_{99}} \tag{4.3}$$

According to this definition the presently selected value would be $C_\mu = 0.006$, which is approximately equal to the weakest perturbation magnitude tested by Mohammed-Taifour and Weiss 2021 on the case of a pressure-induced turbulent separation bubble. The momentum coefficient of unsteady control cases will be discussed after the frequency sweep presented in the next section, from which specific control cases of interest will be selected.

4.3. Actuation frequency sweep

With a chosen nominal $VR = 1.6$ for further study, attention is turned to unsteady actuation. The actuators are run at a duty cycle of $DC = 50\%$ and the frequency is changed from a lowest value of 5 Hz to a highest value of 500 Hz. This data was post-processed in real time so initially sparse frequency points were acquired after which additional points were added in regions of high gradients. The results given by the M_p metric are shown in figure 4.6, where the effectiveness of steady actuation is marked by a horizontal line.

As already mentioned, due to time constraints the acquisition time per data point was 120 s in this sweep, which left noise in the data. From four 10-minute acquisitions which were taken during PIV runs, the standard deviation of the determined metric due to non-converged measurements was estimated to be 0.002. Figure 4.6 shows on the marked points the 3σ confidence interval based on this estimate. It's clear that the measured noise is approximately of this scale showing that it's most likely a product of unconverged measurements. However it is also clear that the global trends in the curve are statistically significant and can be trusted. Those trends clearly indicate that there exists an optimal acutation frequency range, which is from approximately 15 to 30 Hz ($St_h = 0.08 - 0.16$), in which the metric M_p is improved with respect to steady blowing to the same degree as if the jet velocity in steady actuation was increased by 25 percent. Above this range and past approximately 100 Hz the effectiveness hovers around that of steady actuation.

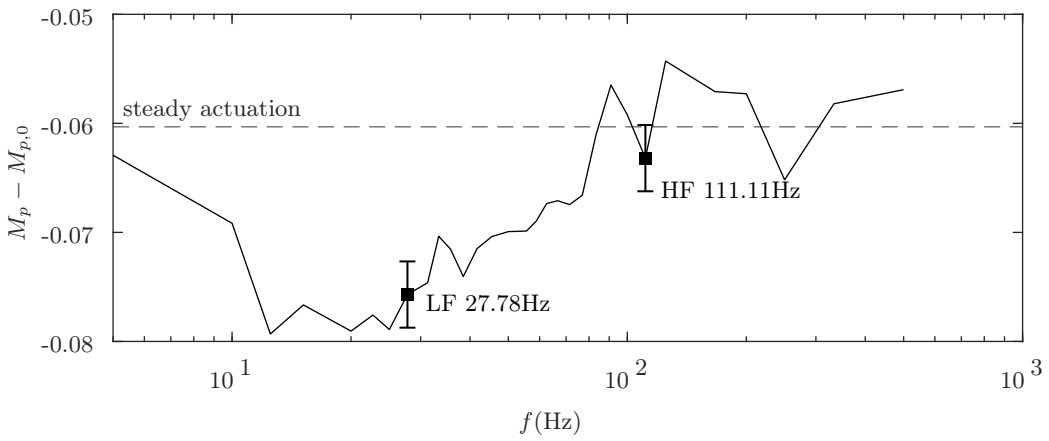

Figure 4.6: Control effectiveness frequency sweep for actuation with a duty cycle $DC = 50\%$ and a velocity ratio $VR = 1.6$. (■) frequencies selected for further study: low frequency LF and high frequency HF.

Based on these results, two single frequency cases and a burst modulated case are chosen for further detailed investigation:

- low frequency (LF) - $f_l = 27.78$ Hz
- high frequency (HF) - $f_h = 4f_l = 111.11$ Hz
- burst modulation (BM) - $f_m = f_l = 27.78$ Hz, $f_c = 3f_l = 83.33$ Hz

Along with steady blowing, each of these actuation strategies is tested in both 3D1 and 3D2 modes (see section 3.1.2 for an explanation), yielding a total of 8 tested control cases. The relevant operating parameters for each case are given in table 4.2. According to figure 4.4, a constant factor of 0.8 is applied to the momentum ratio of the single frequency control cases, while the burst modulated case has an additional 2/3 factor due to being composed of 1 inactive and 2 active periods at the carrier frequency $f_c = 83.33$ Hz.

Actuation mode	f (Hz)	VR	U_j (m/s)	C_μ (%)
steady (S)	-	1.6	24	2.3
low frequency (LF)	27.78	1.6	24	1.8
high frequency (HF)	111.11	1.6	24	1.8
burst modulation (BM)	27.78, 83.33	1.6	24	1.2

Table 4.2: Control cases selected for detailed analysis and their nominal operating parameters. Values of C_μ are determined from jet velocity measurements in quiescent surroundings.

5

Uncontrolled flow characterization

Before moving on to the PIV analysis of the controlled cases, this chapter presents an analysis of the uncontrolled separating turbulent flow in the test section which provides a baseline against which the effects of control are assessed. The nominal tunnel velocity is $U_0 = 15m/s$ at the location of the Prandtl-Pitot probe shown in figure 3.4.

Firstly, the mean flowfield and the extent of the separation bubble are analyzed. Then development of the boundary layer upstream of detachment and the separated shear layer downstream of detachment are discussed, with spectra of both presented. Finally, the spatial nature of the flowfield is analyzed using statistical methods.

5.1. Mean flow

The mean streamwise velocity field of the flow in the streamwise, wall-normal plane 1 is shown in figure 5.1 overlayed with streamlines.

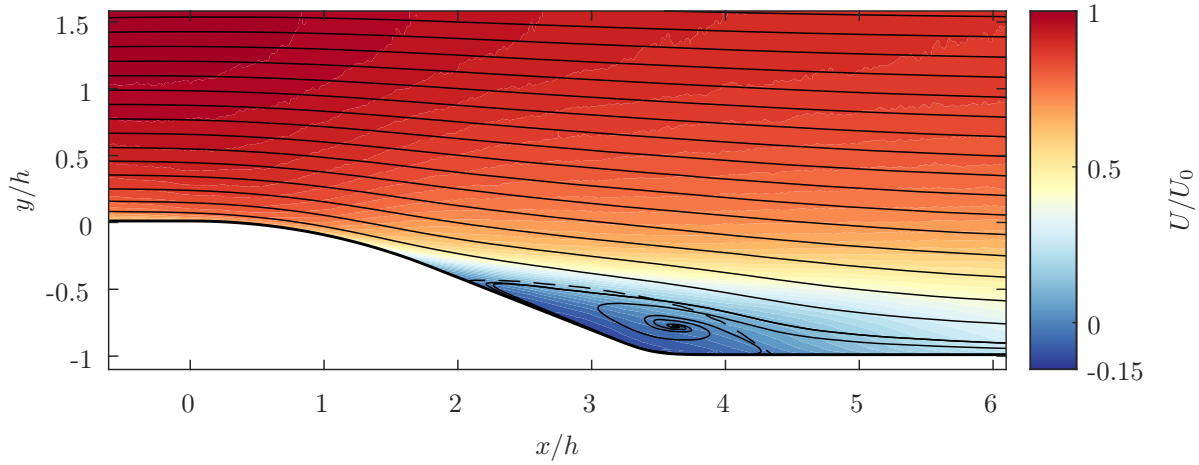

Figure 5.1: Contour plot of mean streamwise velocity with overlayed mean streamlines for the uncontrolled flowfield in plane 1 (*solid*) and the $\Psi = 0$ curve (*dashed*).

Also shown is the $\Psi = 0$ curve, which is determined by integrating the streamwise velocity profile in y and finding the zero-crossing if it exists.

$$y(x, \Psi = 0) = \left\{ y : \int_0^y U(x, y')dy' = 0 \right\} \tag{5.1}$$

As such it represents the wall-normal distance with zero net volume flux and intersects the wall in the locations of TD and TR where the mean streamwise velocity is 0. In a purely two-dimensional flow, this would represent the dividing streamline between the recirculation bubble and the external

flowfield, however in this case due to end-effects of the experimental set-up, there is spanwise flow and the recirculation region is not exactly closed as seen in the streamline pattern. Nevertheless, $\Psi = 0$ is used as indication of the size of the separation bubble as it's most directly related to the obstruction experienced by the flow.

Besides the apparent flow separation and the accompanying recirculation region there are a few other features to note. Far from the wall the velocity drops relatively linearly as the cross-sectional area of the tunnel increases. Close to the wall upstream of detachment, the flow first accelerates due to the curvature of the wall towards the pressure minimum and then decelerates in the pressure recovery region until finally detaching.

The backflow coefficient field of the uncontrolled flow is shown in figure 5.2. Marked are also the locations of detachment and reattachment, as well as the $\Psi = 0$ and $U = 0$ contour lines. Due to the smoothly curved ramp, the detachment is not fixed and happens intermittently at approximately half the streamwise distance down the ramp. As in most other separation studies, the region of intermittent reattachment is larger than that of detachment. Note that the $\Psi = 0$ and $U = 0$ contours begin and end in the same location and because the $\Psi = 0$ curve is found to generally be less noisy due to being further from the wall, this is what is used when referring to separation bubble size.

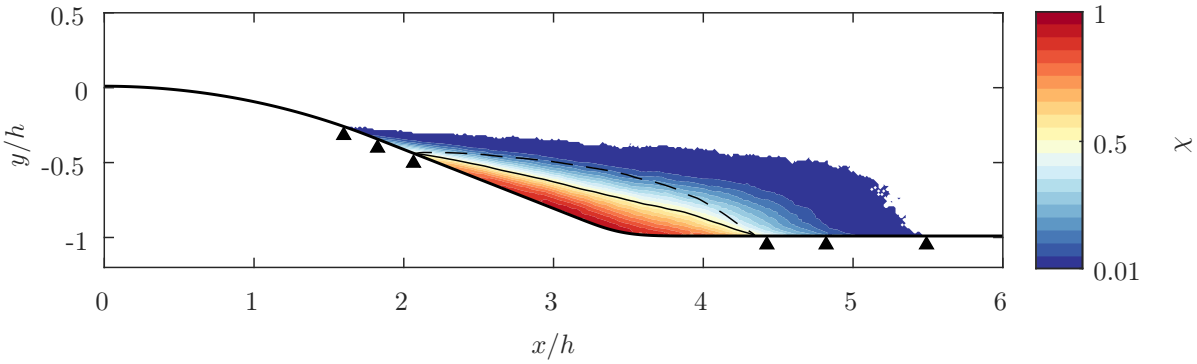

Figure 5.2: Contours of backflow coefficient χ. Solid line: $U = 0$, dashed line: $\Psi = 0$, markers: locations of ID, ITD, TD, TR, ITR and IR in order.

As already noted, the recirculation region isn't formally recirculating as it is open on the downstream end, which indicates that there are non-zero components of out-of-plane velocity. An investigation of this can be done via the continuity equation based on the fact that this is a low velocity, incompressible flow. A non-zero net mass flux of a control surface in the xy plane necessitates the same mass flux to be flowing towards or away from the plane, appearing as a source or sink respectively.

$$\frac{\partial U}{\partial x} + \frac{\partial V}{\partial y} = -\frac{\partial W}{\partial z} \tag{5.2}$$

This *continuity residual* is shown in figure 5.3. Given that the calculation involves finite differences of noisy PIV data, Gaussian smoothing is applied to the end result.

To interpret this data, take into account that this PIV plane runs approximately along the symmetry plane of the tunnel which means that the assumption of $W \approx 0$ can be made. A positive value of W_z then means that the flow is diverging from the PIV plane, while a negative value means it's converging towards it. The flow far from the separation region has a slight component of velocity towards the symmetry plane. This is due to the growth of the boundary layers on the sidewalls of the tunnel which are also under APG.

Then around the point of detachment, the flow diverges from the plane. PIV plane 2 runs exactly through this region and the mean velocity fields acquired in it are shown in figure 5.4. The significant three-dimensionality of the flow is immediately clear. These velocity fields indicate that within the measured field-of-view, the bubble cross-section is largest in the tunnel symmetry plane and reduces away from it. This difference in blockage across the span would explain why the flow diverts away from the symmetry plane around the point of detachment. At the same time, a larger separation in $z = 0$ is expected to result in a lower bubble pressure such that there is a spanwise pressure gradient within the bubble driving flow towards $z = 0$, which is indeed seen slightly downstream around the point of

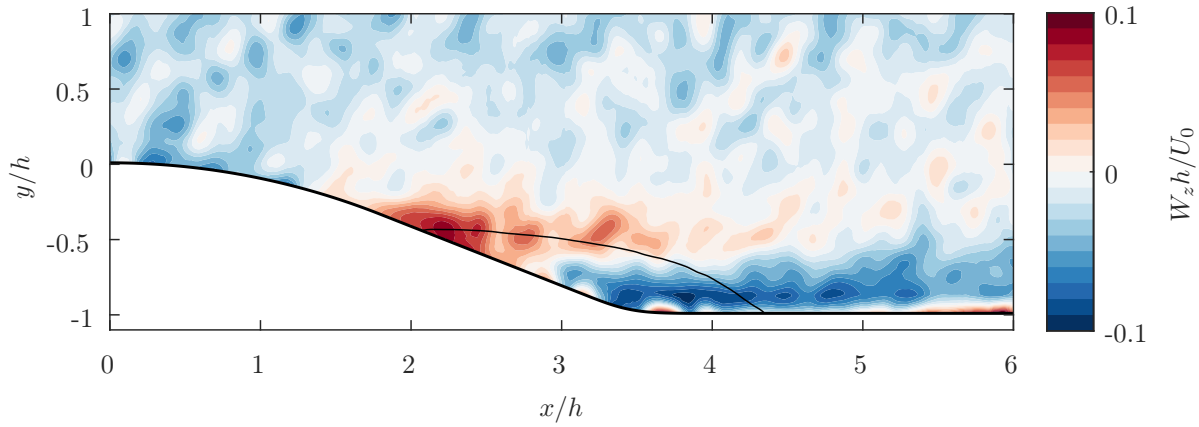

Figure 5.3: Contour plot of the mean out-of-plane velocity gradient $W_z = \frac{\partial w}{\partial z}$ in plane 1.

reattachment. Ultimately, the net massflux in the bubble is towards $z = 0$ as the streamline pattern in figure 5.1 clearly exhibits a source topology.

It's natural to conclude that the 3D nature of the flow is related to the finite span of the ramp and the theory as to the exact effect is built from tuft visualizations and comparison with other such separations of limited aspect ratio (Mohammed-Taifour and Weiss 2021; Simmons et al. 2022). Separation happens earliest in the corner between the tunnel sidewalls and the ramp as the merged boundary layers have the highest momentum deficit. This separation rapidly increases the displacement thickness at the ends of the ramp, inwashing and providing pressure gradient relief to the as yet unseparated neighboring flow by effectively reducing the area expansion. The effect drops off towards the tunnel symmetry plane which therefore experiences a stronger adverse pressure gradient and earlier separation. Besides the effect on pressure gradient, another contributor to the uneven separation might be the fact that adding a spanwise component to the flow effectively sweeps the ramp reducing the wall curvature experienced by the flow, also positively impacting attachment. This is ofcourse not realized in the symmetry plane where the flow is two-dimensional by definition.

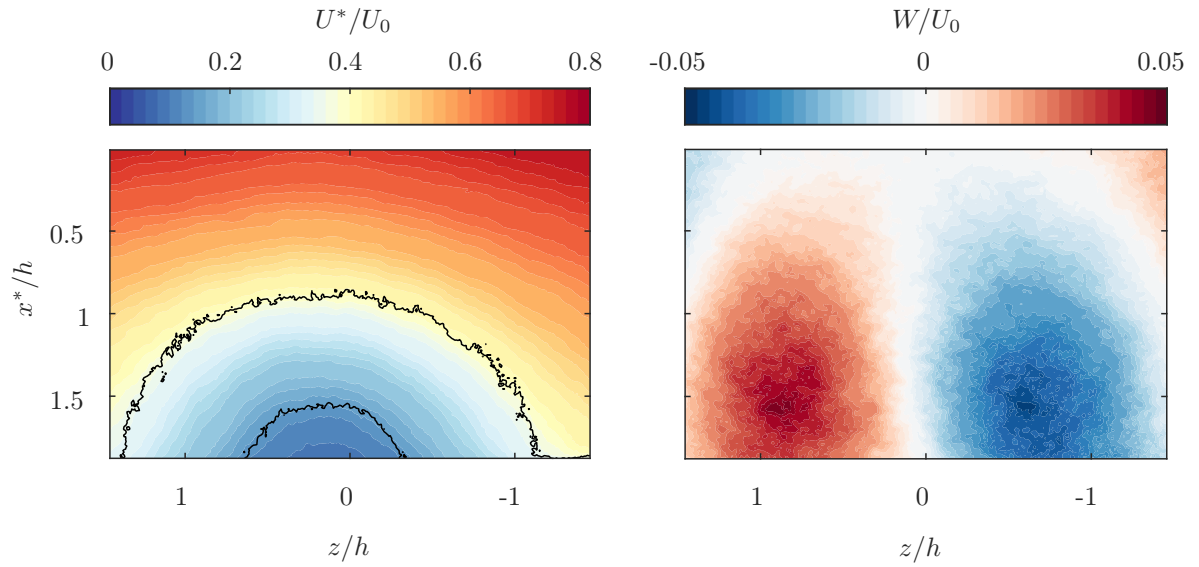

Figure 5.4: Contour plots of mean streamwise (*left*) and spanwise (*right*) velocity in plane 2. Solid contour lines indicate $\chi = 0.01$ and $\chi = 0.2$.

5.2. Boundary layer upstream of detachment

The integral parameters and outer scales of the boundary layer upstream of separation were studied from PIV acqusitions in plane 1. Meanwhile, in order to accurately resolve the inner and temporal scales of the incoming boundary layer, it was traversed by a hot-wire at a streamwise position 2 cm upstream of the actuators ($x/h = -0.88$) in 40 points, logarithmically spaced from a wall-normal coordinate of 0.25 mm to 90 mm with a measurement time of 150 s per point at an acquisiton frequency of 51.2 kHz. This position was selected because it lies upstream of actuator and ramp joint surface irregularities which have a local effect on the inner and overlap layers reducing the generality of the measurements.

The HW inner-scaled mean velocity and TKE profiles are given in figure 5.5. The overlap layer is sufficiently resolved to fit the log law to it, following Clauser's chart method in which the friction velocity u_τ is the single free fitting parameter and the fitting is done using a nonlinear least squares approach to points which are deemed to lie in the overlap region. This is 7 points in total spanning $y^+ = [68, 170]$. For reference, all of the important boundary layer parameters upstream of the ramp are given in table 5.1. The turbulence kinetic energy profile indicates an inner peak at $y^+ = 15$ and a relatively long tail in the outer boundary layer.

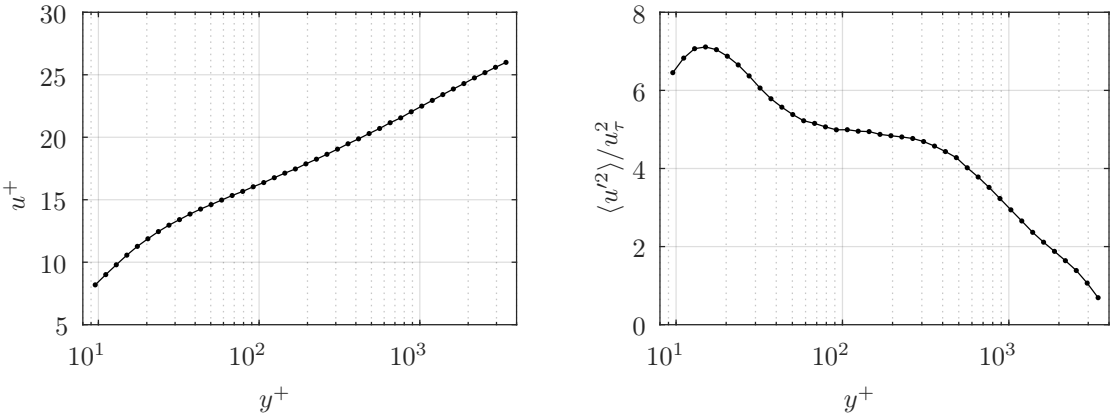

Figure 5.5: Inner-scaled (a) mean velocity and (b) turbulence kinetic energy profiles of the uncontrolled flow upstream of actuator in wall units.

nominal U_0 (m/s)	δ_{99} (mm)	δ^* (mm)	θ (mm)	δ_ν (μm)	u_τ (m/s)	H	Re_θ	Re_τ
15	120	14.0	11.1	26.2	0.57	1.27	11160	4580

Table 5.1: Parameters of the uncontrolled turbulent boundary layer upstream of the ramp.

Figure 5.6 shows the viscous and equivalent inviscid velocity profiles in the region upstream and just past the point of detachment. The development of the BL parameters, determined in relation to the EIF, and the static pressure are shown in figure 5.7. The displacement thickness rises rapidly and monotonically as separation is approached, while the momentum thickness first increases and then flattens out just after detachment. The shape factor has a pronounced rise at the beginning of the curved ramp section ($x/h = 0$). This could physically be a consequence of the sudden change in wall curvature but it could also be down to PIV or EIF error. It then follows a relatively linear growth until detachment begins at which point the growth accelerates. Transient detachment ($\chi = 0.5$) occurs at a shape factor of $H_{sep} = 2.01$ which is on the lower end of the range of experimental values reported by Cebeci and Bradshaw 1977. This is most likely a consequence of the relatively high wall curvature which tends to have this effect, as noted by Simpson 1996.

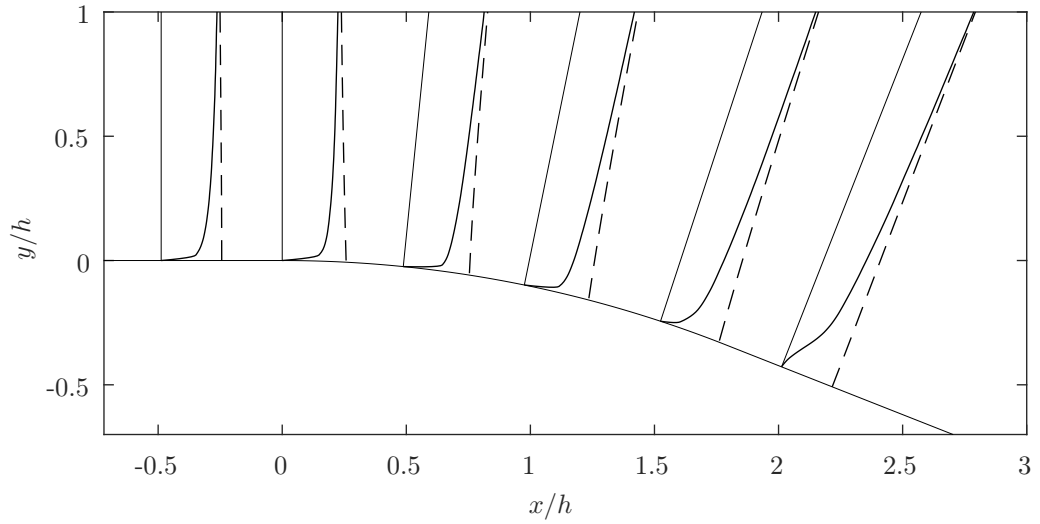

Figure 5.6: Boundary layer velocity profiles upstream of detachment (solid line: real viscous flow measured by PIV, dashed line: calculated equivalent inviscid flow).

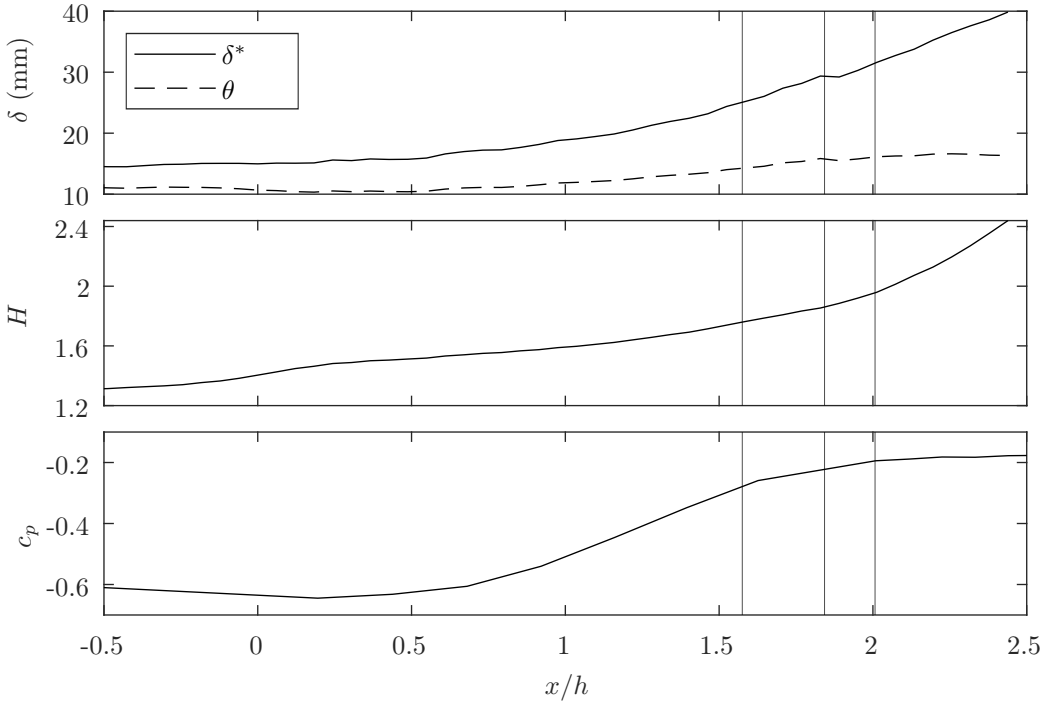

Figure 5.7: Development of the boundary layer up to detachment (top: displacement and momentum thickness, middle: shape factor, bottom: pressure coefficient, vertical lines: ID, ITD and TD in order).

5.3. Shear layer downstream of detachment

As the flow near the wall is retarded by the imposed APG the point of maximum shear moves away from the wall (see figure 5.8). This inflection point in the profile is a necessary (but not neccesarily sufficient) condition for inviscid instability to develop according to Rayleigh's criterion. In the present flow, the appearance of an inflection point in the profile coincides with the movement of the maximum in velocity fluctuation away from the wall, marking the beginning of flow instability. This happens at $x/h \approx 1.6$ which also corresponds to the point at which intermittent detachment begins.

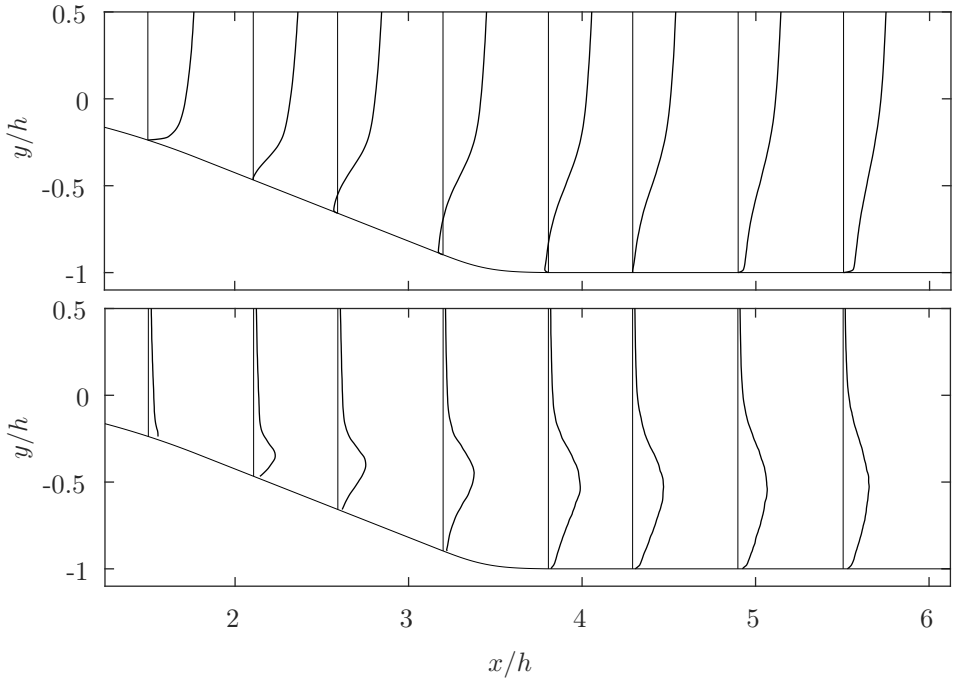

Figure 5.8: (Top) Streamwise velocity profiles downstream of detachment (dashed line: locus of maximum velocity variance). (Bottom) Profiles of velocity variance $\langle u'^2 + v'^2 \rangle$.

The trajectory of the shear layer can be understood as the line joining the points of maximum vorticity of the flow velocity profiles which also in this case and more generally corresponds to the point of maximum turbulent kinetic energy. Asymmetrical entrainment and shear layer structure growth means that this trajectory doesn't correspond to any mean flow streamline. In the case of a wall-bounded flow such as this, this difference is accentuated by the fact that entrainment of the low velocity stream bounded by the wall turns the flow towards the wall.

The convection velocity of shear layer structures is widely reported to be the mean shear layer profile velocity $(U_{max} + U_{min})/2$. This, along with the convection velocity along the shear layer trajectory measured in this case are shown in figure 5.9. The fact that the measured convection velocity starts lower and tends to the predicted value suggest that only a portion of the incoming boundary layer vorticity takes part in the initial shear layer instability, which is evidence of the development of a Morris and Foss 2003. These authors term this the *sub-shear layer* and posit that it's a general feature of turbulent separations because in TBL vorticity is heavily concentrated near the wall. In this case, considering the large size of the boundary layer with respect to the separation bubble, there isn't sufficient development length for the initial sub-shear layer to grow into the full shear layer encompassing all of the initial boundary layer.

The vorticity thickness of the shear layer is given by 5.3.

$$\delta_\omega = \frac{U_{max} - U_{min}}{\left(\frac{dU}{dy}\right)_{max}} \tag{5.3}$$

In the region of the sub-shear layer, the "high-speed" stream velocity U_{max} is taken to be the *effective* outer velocity of the sub-shear layer. The development of δ_ω is shown in figure 5.9. Over the backflow region the vorticity thickness increases linearly at a rate of $d\delta_\omega/dx = 0.26$. Browand and Troutt 1985 give this rate for free turbulent shear layers to be equal to $0.17R$ where R is the velocity ratio. In this case over the separation bubble the velocity ratio is $R \approx 1.25$ which gives a growth rate of 0.21. The measured growth rate is slightly larger than this which was to be expected as the low-speed stream in this case is a turbulent recirculation region.

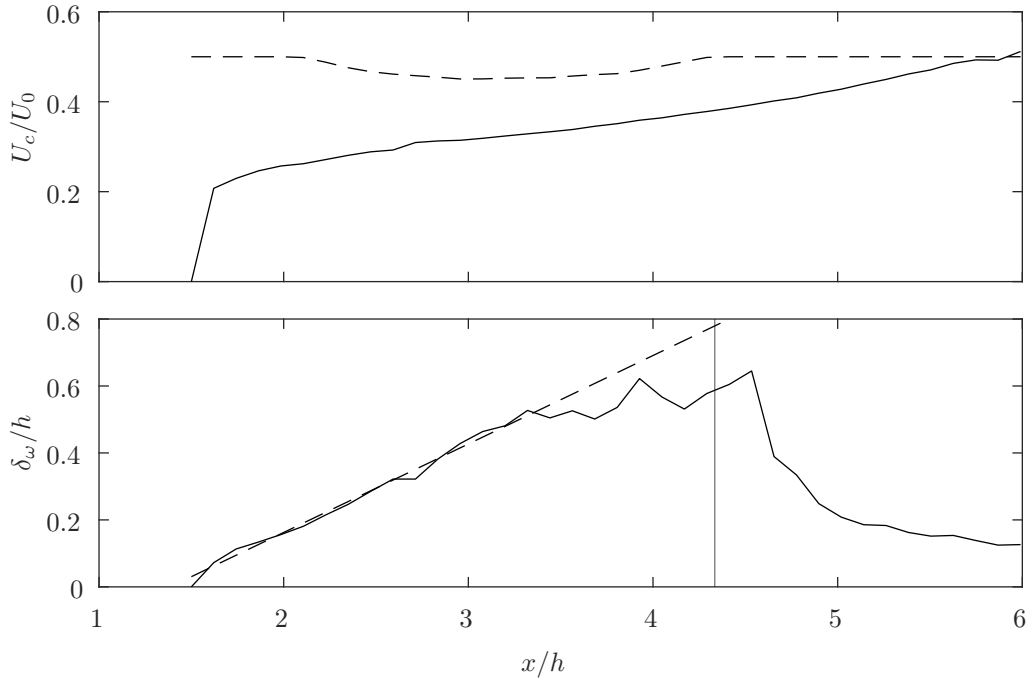

Figure 5.9: (Top) Convection velocity U_c along the locus of maximum vorticity in the shear layer (solid) and mean profile velocity $(U_{max} + U_{min})/2$ (dashed). (Bottom) Development of the vorticity thickness δ_ω with the vertical line marking TR.

5.4. Spectral analysis

The inner-scaled 2D premultiplied power spectra of the velocity fluctuations in the boundary layer upstream of the ramp are shown in figure 5.10 as a function of wall-normal distance and the streamwise fluctuation wavelength λ^+. This is obtained through the frozen flow hypothesis by assuming that the temporal fluctuations are produced by frozen flow structures with a constant convection velocity equal to the mean velocity at a given y such that $\lambda^+ = \frac{U}{\delta_\nu f}$. To reduce noise in the spectra, they were ensemble averaged with ensembles containing 2^{15} points and overlapping 50%. Finally, a 6% bandwith kernel moving filter was applied to smooth the data. On the same plot, the tested actuator operating frequencies are shown.

Two physical peaks are pronounced in the spectra: an inner peak at $y^+ = 15$ related to the near wall cycle and an outer peak at $y^+ \approx 200$. With increasing wall distance a shift of energy to larger wavelengths is apparent indicating the increase in size of the prevailing structures. A significant amount of the outer peak energy is contained within the large scale outer layer structures (Hutchins and Marusic 2007a). In outer scaling here it is found at approximately $y/\delta = 0.06$ and $\lambda_x/\delta = 4$ which is similar to values reported by Hutchins and Marusic 2007a for ZPG ($y/\delta = 0.06$ and $\lambda_x/\delta = 6$) with the exception that the streamise wavelength seems to be reduced. This is not unexpected as APGs have been found to reduce the streamwise organization of vortices that lead to the formation of large scale log layer structures (Lee 2017).

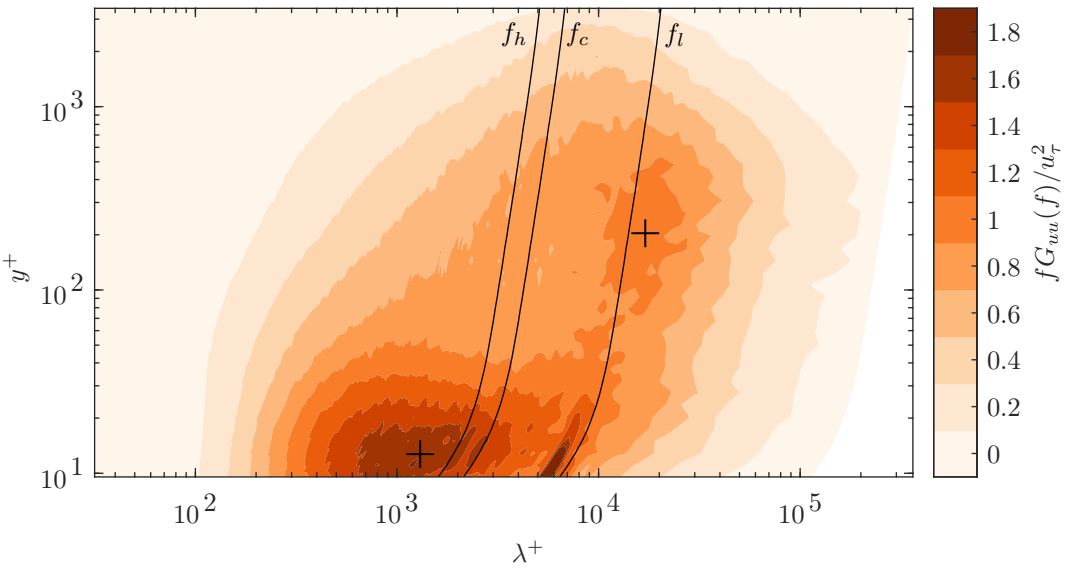

Figure 5.10: 2D premultiplied power spectra of the velocity fluctuations measured in the turbulent boundary layer 2cm upstream of the actuator. Physical peaks marked by black crosses and selected actuation frequencies shown by solid lines.

There is another peak apparent in the spectra in the near-wall region with $\lambda^+ \approx 6000$ or a frequency $f \approx 32$ Hz. This is ascribed to oscillation of the hot-wire sting. Near the wall the gradient of flow velocity is largest so even a small movement of the hot-wire normal to the wall results in large measured velocity oscillations. Furthermore, since the flow velocity near the wall is small, the oscillation velocity measured due to the relative motion of the wire becomes a significant component of the total measurement. Using a larger ensemble size to increase frequency resolution it becomes apparent that there are actually two nearby peaks (see figure 5.11a). The sting is cantilevered as shown in figure 5.11b and most flexible in horizontal and vertical flexion. These 2 DOF yield two similar but distinct eigenfrequencies.

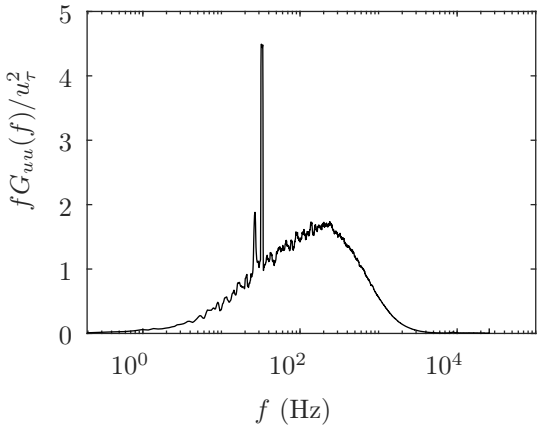

(a)

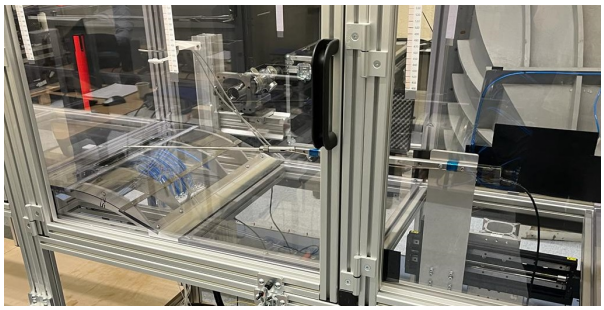

(b)

Figure 5.11: (a) Premultiplied power spectrum of the BL velocity fluctuation at $y = 0.25$ mm with the sting eigenfrequencies apparent. (b) Hot-wire probe sting during upstream boundary layer measurement.

Figure 5.12a shows the shear layer spectra in points along its trajectory along with a slice through the upstream boundary layer spectrum (figure 5.10) through the outer peak with the tested actuation frequencies shown for reference. There is a clear trend of downstream increase in total fluctuation energy and, towards reattachment, a single clear, though relatively broadband, peak emerges in a frequency range of $St_h \approx 0.08 - 0.2$ (15-34 Hz) centered at $St_h = 0.14$ (26 Hz). No other peaks, even

broadband ones are noted. Importantly, note that the initial actuation frequency sweep (see figure 4.3) has indicated that the range of most effective actuation frequencies for this flowfield corresponds exactly to this detected broadband peak. The mechanisms underpinning this relationship will be thoroughly investigated in the next chapter 6.

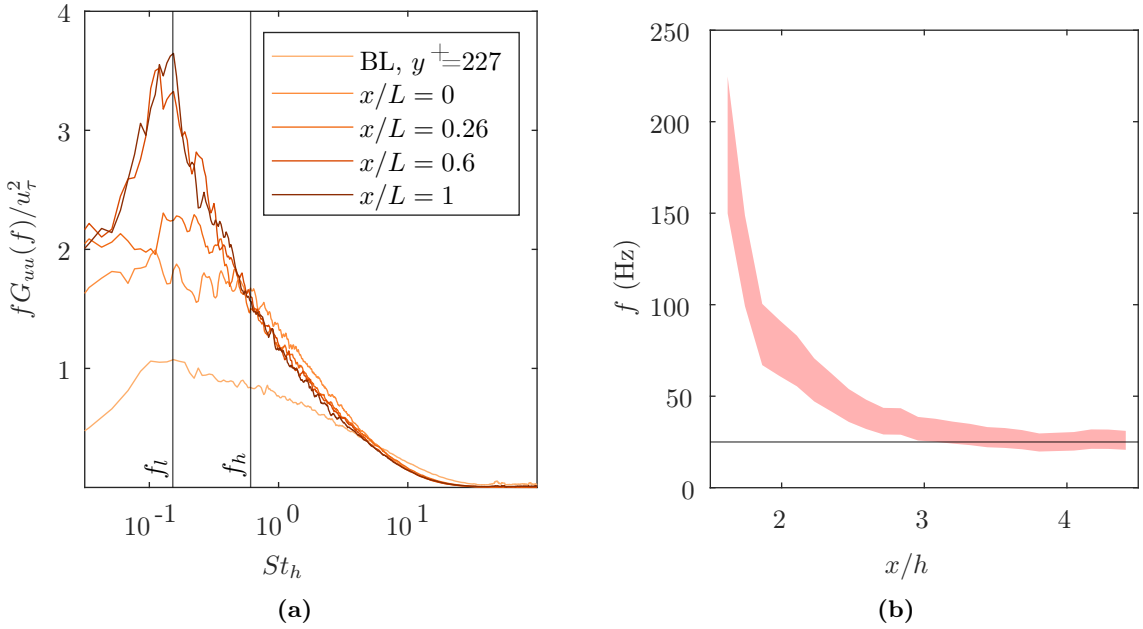

Figure 5.12: (a) Premultiplied power spectra of the velocity fluctuation at multiple points along the separated shear layer as well as in the upstream boundary layer at the wall-normal coordinate of the outer peak with selected actuation frequencies shown. (b) Measured dominant separation bubble frequency (horizontal line) compared with the reported mixing layer natural frequency $St_{\delta_\omega} = f\delta_\omega/U_s = 0.2 - 0.3$.

The nature of the flow unsteadiness related to the identified spectral peak is not completely clear. While the total energy is significantly higher, it's apparent that the measured peak corresponds very closely to the broadband outer peak measured in the upstream boundary layer. This suggests that the dominant unsteadiness measured in the bubble could be driven by the high and low momentum structures in the incoming boundary layer, which is not hard to believe considering the commensurate scale of the bubble and the boundary layer structures. Previous studies have demonstrated this mechanism in multiple flows with pressure-induced separation, for example for an incompressible forward facing step flow (Pearson et al. 2013) and for a compressible shock-induced separation ahead of a compression ramp (Ganapathisubramani et al. 2007). The mechanism itself is easy to understand since an instantaneously lower shape factor will allow the boundary layer to sustain a higher pressure rise before separation and vice versa. The motion of the detachment line then also has an effect on the reattachment point through viscous-inviscid coupling, which would explain how the turbulent fluctuations present in the boundary layer are amplified over the separation bubble.

On the other hand, a separated shear layer with its inflectional velocity profiles is inviscidly unstable. Because of this, the dominant spectral peak is generally ascribed to Kelvin-Helmholtz driven vortex shedding. And in the present case the measured dominant frequency correlates reasonably well to shedding frequencies reported for similar turbulent separation bubbles, which are in the range $St_h \approx 0.08 - 0.2$. As further validation, for free turbulent mixing layers the dominant frequency has been reported as a function of convection velocity and vorticity thickness to lie in the range $St_{\delta_\omega} = f\delta_\omega/U_c \approx 0.2 - 0.3$ (Wu et al. 2019). Based on the previously determined convection velocity $U_c(x)$ and vorticity thickness $\delta_\omega(x)$, this is shown in figure 5.12b along with the experimentally determined peak ($f = 26.25$ Hz, $St_h = 0.14$) marked by a horizontal line, and the excellent agreement in the final shedding frequency with the present experimental measurements is clear.

With that said, as the shear layer grows linearly, its dominant frequency is expected to drop

approximately as $1/x$, before stabilizing at the shedding frequency when the shear layer growth becomes constrained by the wall. In the acquired measurements, although the BL and $x/L = 0$ spectra show a bit more high frequency content, the broadband peak is located at the same frequency along the entire shear layer and there are no indications of higher frequency peaks corresponding to early shear layer instabilities. This doesn't mean that the Kelvin-Helmholtz instability mechanism isn't at work and could be down to the fact that the point of detachment varies with streamwise position, span and time such that measuring at a fixed point in space doesn't capture any coherent oscillation. Downstream, these early instabilities grow and coalesce into a global oscillation of the bubble which is then easier to detect.

Ultimately, it seems that the similarity of the vortex shedding frequency and the frequency of fluctuation in the outer layer of the incoming boundary layer is somewhat of a coincidence stemming from the similar scale of the ramp and boundary layer. The presented spectra, scaled with the reference velocity and ramp height, are very similar to those obtained by others for similar geometries with $\delta/h \approx 1$ and turbulent boundary layers, for example Zhong and Zhang 2013, displaying only a single broadband peak in the same range. As already noted, most of these studies ascribe this unsteadiness to Kelvin-Helmholtz driven vortex shedding, without a detailed characterization of the upstream boundary layer unsteadiness. But it seems most probable that both mechanisms contribute to the measured unsteadiness, given their commensurate scales. Furthermore, given that the separation line is free to move, the two mechanisms are likely strongly coupled via the APG oscillation connected to the motion of the separation line.

5.5. Spatial flow structure

To further investigate the nature of the flow unsteadiness, attention is turned towards its spatial structure starting with a proper orthogonal decomposition. The energy distribution among the modes is given in figure 5.13 and the curl of the first 6 modes is shown in figure 5.14. The energy distribution among the modes is very broadband. The first mode contains around 12% of the total fluctuation energy and corresponds to a breathing (contraction and expansion) of the bubble. The following modes present waves of gradually decreasing wavelength and energy content, giving indication of the turbulent energy cascade process underpinning these results. Additionally, given the high turbulence intensity of the BL, there is no clear indication of a convective shedding mode pair with similar energies.

In comparison, for the case of separation from a *sharp-edged* ramp, Ramírez Vázquez 2022 obtained in the same test section and with similar flow conditions a much more concentrated energy distribution among the POD modes with the first mode containing 26% of the total fluctuation energy. This suggests that the extra degree-of-freedom in the point of detachment reduces the overall coherence of the flow.

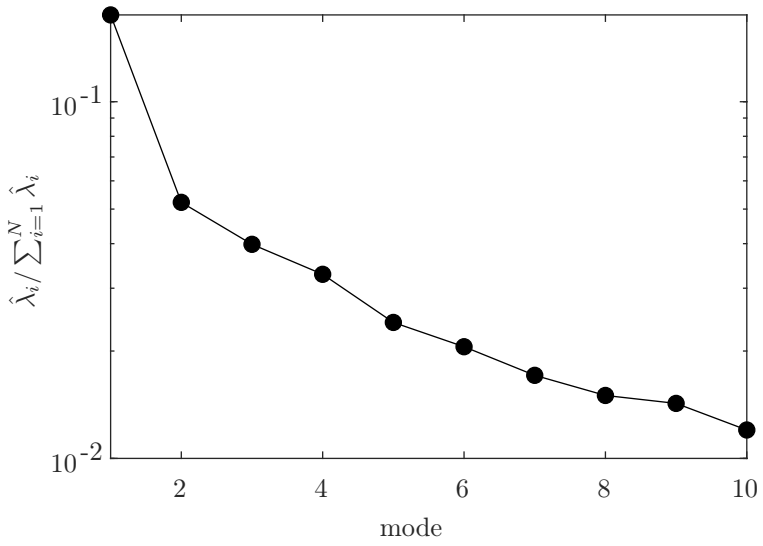

Figure 5.13: Relative energy content of the first 10 POD modes for uncontrolled flow in plane 1.

To investigate this further, a two-point autocorrelation of vertical velocity fluctuation v' is calculated for multiple points along the shear layer. Figure 5.15 shows contour lines corresponding to a correlation

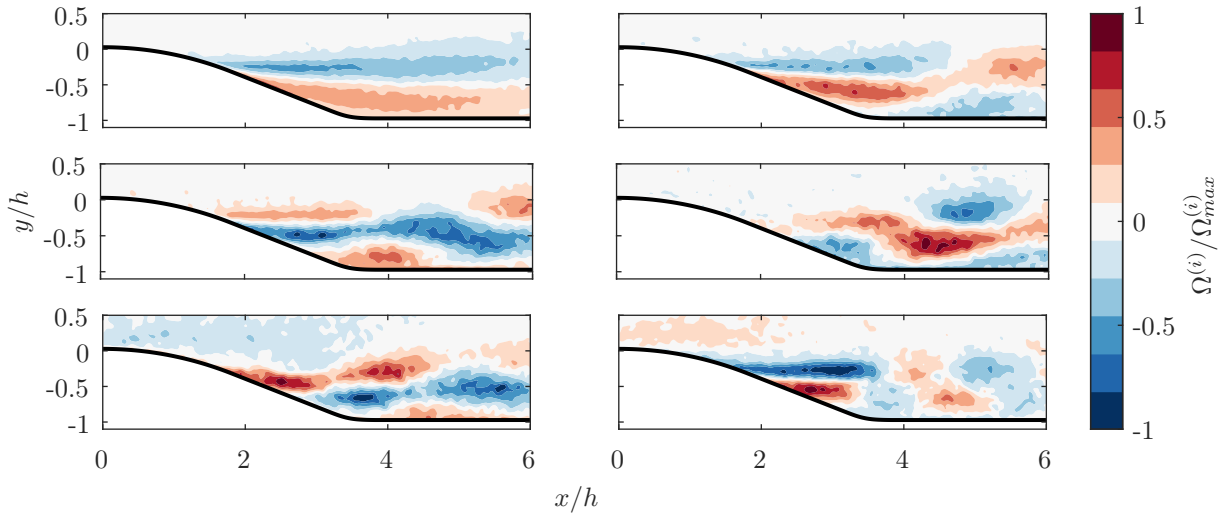

Figure 5.14: POD - curl of the first 6 modes of the uncontrolled flow in plane 1.

value of 0.5. This is taken to be a *significant* correlation such that the contour lines can be viewed as representing the size of the coherent shear layer motions. It is important to note that this value is arbitrary and as such cannot be used to infer the absolute size of structures, however the assumption is that by comparing consistently across different points in space, the relative change in structure size can be obtained.

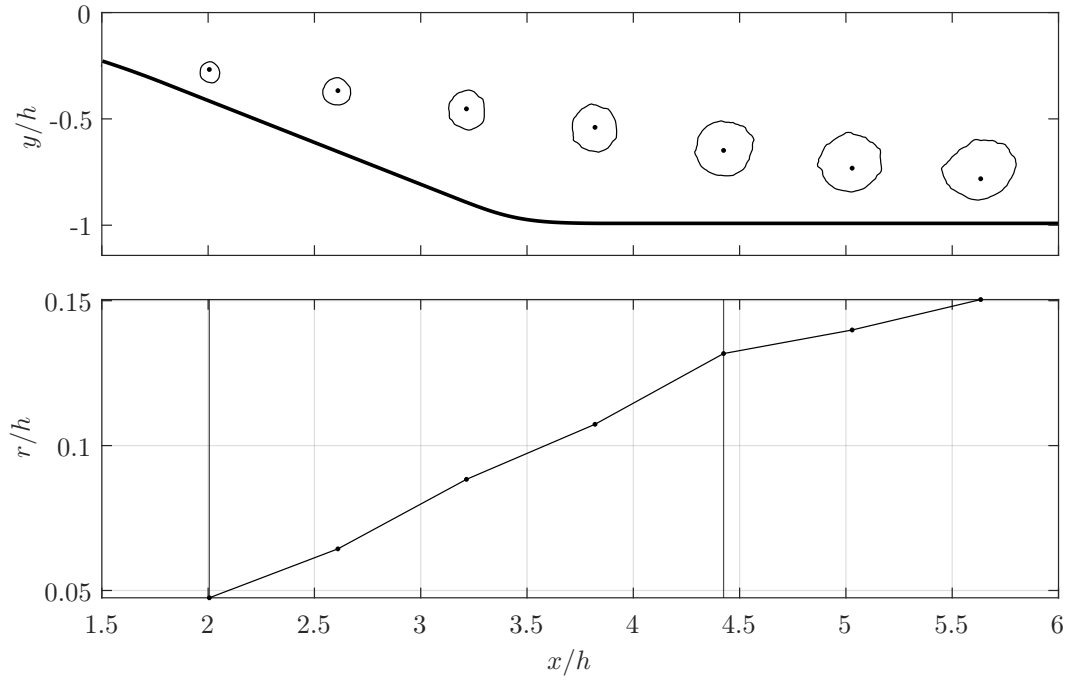

Figure 5.15: Two-point autocorrelation of vertical velocity v for points along the shear layer: (Top) contour lines of $R_{vv} = 0.5$, (Bottom) effective radius of closed contours representing structure size. Vertical lines show the location of detachment and reattachment.

The same figure then also shows how the effective radius of the area enclosed by those contour lines evolves downstream. Above the region of backflow the structures grow approximately linearly, stabilizing at reattachment. Overall, this growth in size follows exactly the trend of vorticity thickness, indicating again how the natural frequency of the shear layer, being the passage frequency of shear layer structures,

drops as their size increases.

While the nominal flowfield and the inviscid KH mechanism are two-dimensional, the dominant flow structures are not due to the high degree of spanwise variation of the flow induced by the incoming BL turbulent structures. Figure 5.16a shows the two-point autocorrelation of streamwise velocity in the wall-parallel plane 2 for 3 different points along the plane of symmetry. The coherent motions of the flow are streamwise elongated and relatively narrow in the spanwise direction. There is no evidence of coherent spanwise rollers which are often observed in 2D separation studies. The first point shown is positioned upstream of detachment and it shows convincing evidence of a burst/sweep pattern accompanying the oscillation of the detachment line. An upstream motion of the detachment line at a given spanwise location reduces flow curvature upstream, reducing the streamwise velocity. In this incompressible flow such a retardation produces an upwards and sideways burst which consequently causes the regions on the left and right of the burst to experience sweeps of flow towards the wall, pushing the point of detachment downstream.

The downstream development of the spanwise length scale l_z, determined as the width of the region with $R_{uu} > 0$, is shown in figure 5.16b. From the start of incipient detachment the length scale increases rapidly, while before and after it remains relatively stable. Prior to detachment, the spanwise wavelength is approximately 0.35δ which agrees with the reported scale of large log layer structures in turbulent boundary layers in APG (Lee 2017). After detachment the spanwise wavelength stabilizes quite quickly, while the size in the wall normal direction continues to grow linearly as already discussed.

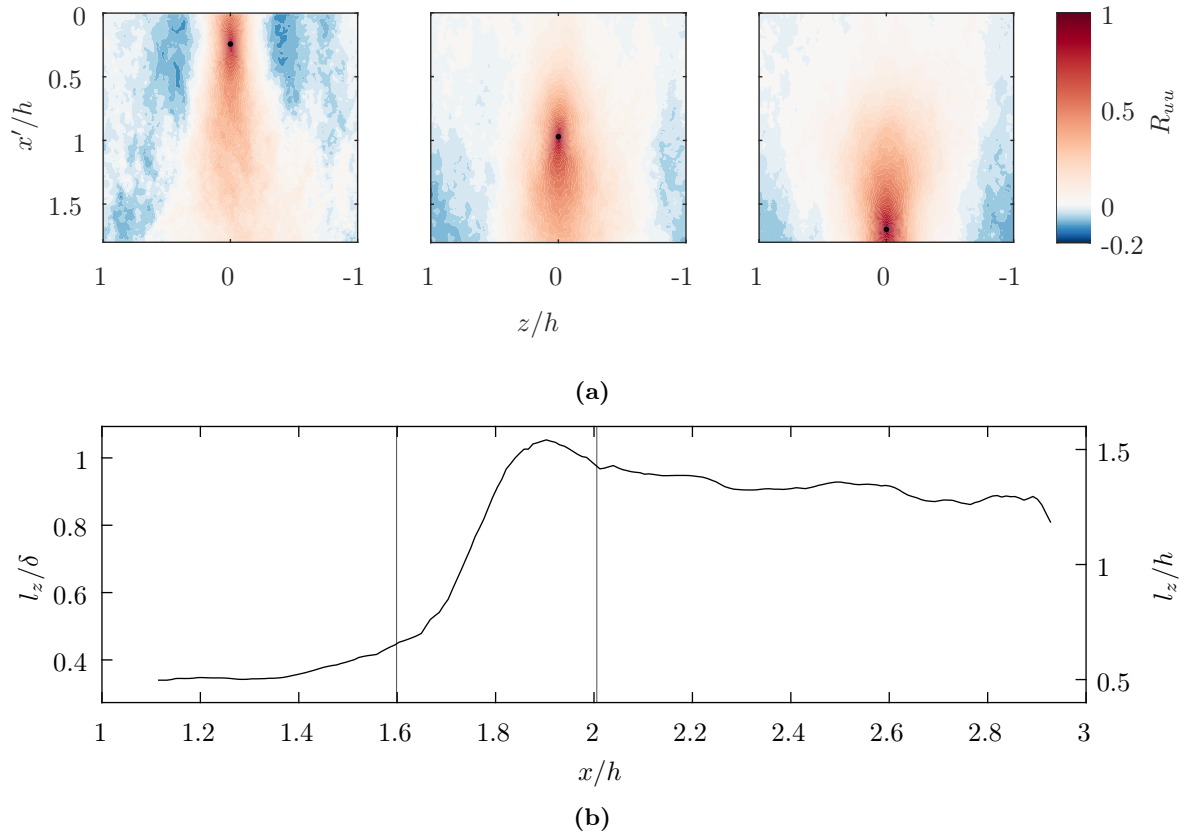

Figure 5.16: (a) Contour plot of the two-point autocorrelation of streamwise velocity fluctuation R_{uu} in plane 2 for 3 points along the plane of symmetry marked by (•). (b) Development of the structure spanwise length scale ($l_z(x) = z : R_{uu} = 0$). The vertical lines mark the locations of ID and TD.

6

Controlled flow characterization

This chapter presents and discusses the results of the PIV investigation of the controlled cases of which there are 8 including steady (S), low single frequency (LF), high single frequency (HF) and burst modulation (BM) for each of the 2 actuation strategies 3D1 and 3D2 (see table 4.2). All of the controlled cases use a nominal velocity ratio of 1.6, which is set in quiescent surroundings with the jet in steady operation and the nominal tunnel velocity is $U_0 = 15$ m/s.

Firstly, an overview of the time-averaged performance of the cases is presented and analyzed which outlines the key performance trends to be explained by the ensuing detailed flowfield analysis. The steady blowing cases are then investigated, providing a structural image of the jet-crossflow interaction and its role in separation control. Finally, the effects of unsteady actuation and their frequency sensitivity are analyzed.

6.1. Performance overview

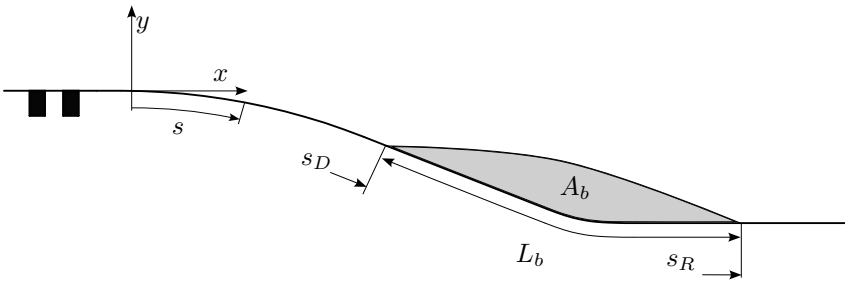

Figure 6.1: Schematic of ramp profile with marked coordinate system, actuator position and recirculation bubble dimensions. Drawing proportions are to scale.

The intent in this section is to compare and discuss the integral performance of all of the studied actuation cases. To do this, firstly PIV derived performance metrics are established. From acquisitions in plane 1, of primary interest are geometrical data relating to the flowfield, namely the positions of detachment and reattachment and the cross-sectional area and shape of the separation bubble. These are illustrated along with the ramp profile, actuator positions and coordinate system in figure 6.1. These metrics are unambiguous and deterministic but they don't directly relate to any potential performance benefit.

Momentum flux data meanwhile has a more direct interpretation in terms of performance, as this is ultimately what determines system forces like lift, drag or pressure drop. In this regard, a valuable metric from acquisitions in plane 1 is the *momentum flux deficit* of the boundary layer downstream of reattachment, given by equation 6.1, where U_i is the velocity profile of the equivalent inviscid flow.

$$P_d = \int_0^\delta (U^2 - U_i^2) dy \tag{6.1}$$

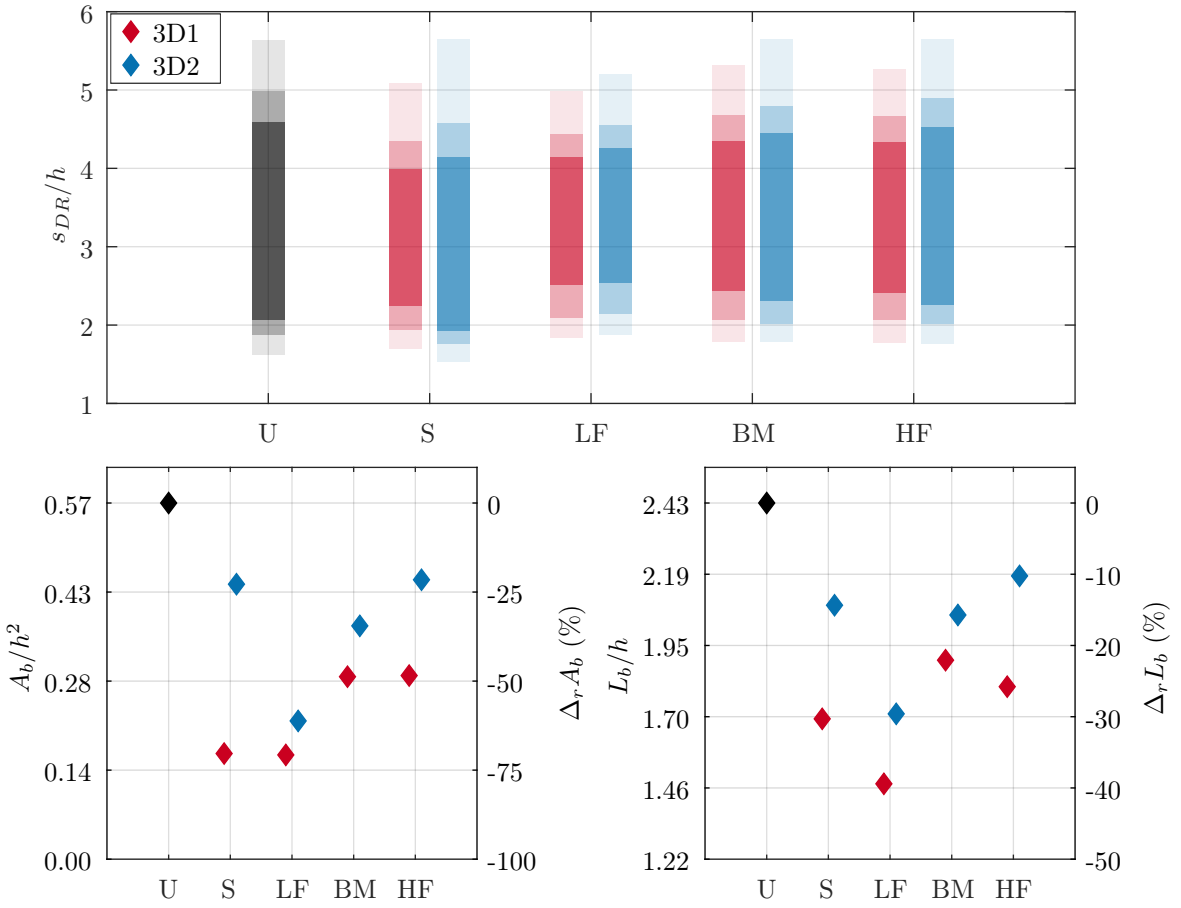

Figure 6.2: Control performance - bubble geometry metrics. (*Top*) Streamwise wall coordinate of detachment and reattachment. Color opacities represent ID, ITD and TD. (*Bottom left*) Recirculation bubble cross-sectional area in plane 1. (*Bottom right*) Recirculation bubble length along the wall in plane 1.

The perturbation applied to the flow by the actuators is three-dimensional by design. So as a streamwise flow section at a single spanwise coordinate, plane 1 cannot be assumed to faithfully represent the state of the flow across the span. This is especially true for the recirculation bubble size and shape, as the plane is directly in a region of very large spanwise gradients, which is apparent from the analysis in section 6.2. Furthermore, the plane runs through the jet wakes, which was done to be able to measure the trajectory of the wake, but it also means that there will be a strong "local" effect measured due to the wake, which might skew results. For the BL at the downstream edge of plane 1 this is expected to be less problematic as these spanwise variations are already mixed out to some degree.

This is where the streamwise momentum flux in plane 2 plays an important role. Since a delay in separation and a reduction in the size of the separation bubble will lead to an increase in this measure, it is argued that it can be used to indicate the state of separation across the span. This metric has been utilized in other studies to assess actuator performance, for example by Scholz et al. 2005. The integral streamwise momentum flux P_2 is therefore defined as given by expression 6.2, where L_2 is the length of plane 2, and the results are shown in figure 6.3. The integration is carried out along a span of 2 perturbation wavelengths λ_z, which equals $z_{int} = [-0.91, 0.91]h$, such that only the part of the actuated span which is quasi-periodic is considered. Note that the wavelength λ_z is equal to twice the actuator spacing λ_j.

$$P_2 = \int_{-\lambda_z}^{\lambda_z} \int_{L_2-L_i}^{L_2} U^{*2} dx^* dz \tag{6.2}$$

The maximum pointwise error in momentum due to uncaptured out-of-plane flow is estimated from the

flow direction measured in plane 1 and is $< 3\%$ but is significantly smaller across the rest of the plane. It is therefore safe to assume the streamwise momentum measured in plane 2 to be representative of the actual streamwise momentum.

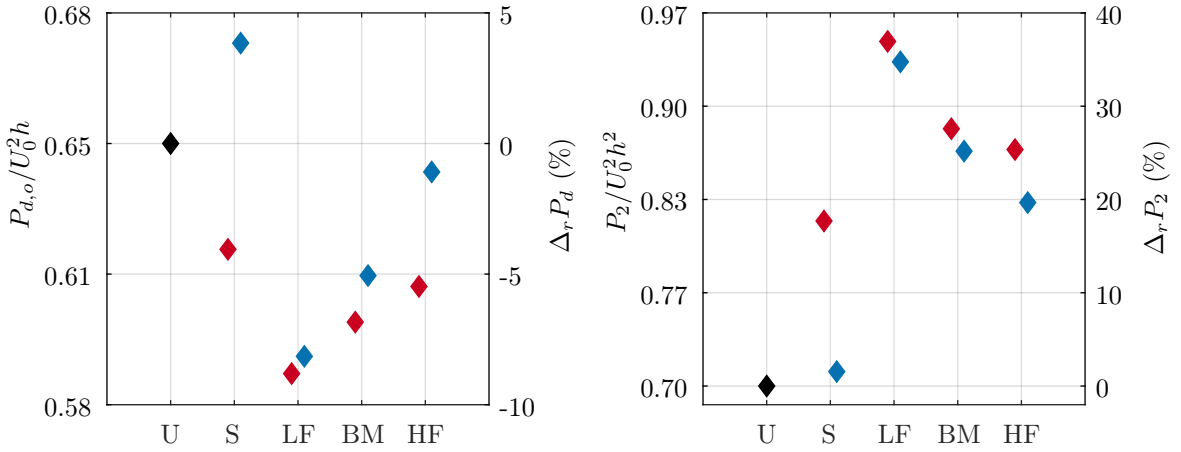

Figure 6.3: Control performance - momentum metrics. (*Left*) Streamwise momentum deficit in the boundary layer at the downstream edge of plane 1. (*Right*) Integrated streamwise momentum in plane 2.

The first thing to note from the results is the large difference in effect between the 3D1 and 3D2 steady actuation cases which is apparent in all considered metrics. In the ideal case of a truly periodic actuator array along an infinite span, the differences between the two cases should be minimal and only down to the slight offset in actuator streamwise position. In fact, from the actuator characterization (figure 4.1) it is clear that with the same manifold feed pressure the upstream row actually has a slightly higher jet velocity than the downstream row and would thus be expected to outperform it, which is opposite to what is observed. As investigated in section 6.2, 3D effects and the fact that the inverted upstream row of actuators has only 2 common downwash regions, compared to the downstream 3, lead to the observed difference. This is important to note as a shortcoming of this experiment as it likely adds bias to the measured performance of 3D2 unsteady cases.

Firstly the single row 3D1 cases are considered. The first important finding is that, according to the momentum metrics, unsteady actuation outperforms steady actuation, even with a nominally smaller total momentum input (see table 4.2). Furthermore, LF forcing at a frequency commensurate with the dominant natural frequency of the separation bubble, is the best actuation tested, yielding an almost doubling of the improvements in momentum metrics achieved by steady blowing. HF forcing meanwhile, yields a much smaller improvement compared to steady blowing, being essentially comparable. These results agree with the findings of the preliminary actuation frequency sweep presented in section 4.3, validating the pressure derived metric used there. Furthermore, these results agree with virtually all unsteady separation control studies (Greenblatt and Wygnanski 2000).

BM forcing with a long period corresponding to LF, falls in terms of performance between the LF and HF cases. This is an interesting result because out of all the tested cases, this injects the least mass and momentum into the flow, so achieving this level of performance can be considered a good result. However, other studies have seen even better results with this forcing approach, noting a negligible performance difference between single frequency and burst modulated control signals at the same frequency (Abdolahipour et al. 2022).

The separation geometry metrics echo to some degree the momentum metric finding, with the notable exception that the size of the bubble cross-section in plane 1 is very small for steady blowing, smaller than for HF and BM cases. Furthermore, while detachment happens earlier than for unsteady cases reattachment happens a lot earlier. As will be shown in section 6.2, this is misleading, because in this case the mean flowfield demonstrates a significant amount of spanwise variation. For the unsteady blowing cases, the mean flowfields are significantly more two-dimensional in nature due to the inactive part of the periods in which the flow recovers from the imposed 3D perturbation. So using these geometrical metrics to compare between the unsteady blowing cases is thought to be less questionable.

Regarding the 3D2 alternating actuation cases, for the same operating conditions, they underperform

conventional single row actuation. Comparing between the cases they demonstrate the same trends as the 3D1 cases with the best performance achieved by LF actuation, the worst by HF and BM slotting between the two. Interestingly the differences between the cases are more pronounced than for 3D1 actuation strategy. So 3D1 and 3D2 LF cases achieve very similar results while there is a significant difference in performance with the HF cases.

6.2. Steady actuation

This section investigates the steady blowing case to establish the mean topology of the jet-crossflow interaction and how it leads to suppression of separation. First 3D1 actuation is considered after which the cause for the very poor performance of 3D2 steady blowing is investigated.

6.2.1. Downstream actuator row (3D1)

The change in the streamwise velocity field in plane 1 achieved by 3D1 steady blowing is shown in figure 6.4. This reveals the trajectory of the jet structure as a low momentum streak, positioned slightly off the wall which indicates a *detached* flow topology, as expected for a velocity ratio of 1.6. Directly above the actuator there appears to be no wake, although there is a low velocity region just upstream of it. This is a consequence of there being no PIV seeding in the jet flow. The seeding in the crossflow mixes with the jet flow quickly, within 2 actuator lengths downstream, so the wake trajectory can be traced from that point on.

Note the three-dimensionality of the flow apparent in the streamline pattern and the difference between the $\Psi = 0$ curve and the actual dividing streamline, which never actually connects to the wall. This indicates that the forward flow downstream of the reverse flow region actually comes from out-of-plane causing the strong increase in forward momentum measured in the plane. This is explained by acquisitions from plane 2.

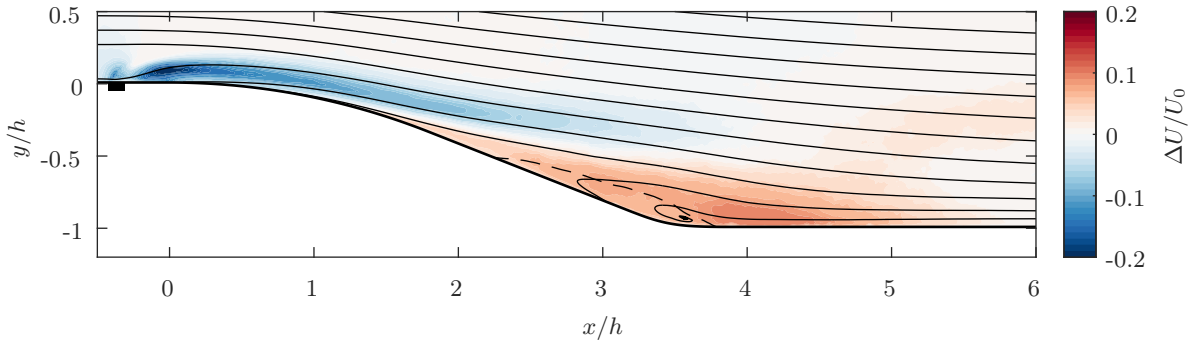

Figure 6.4: Steady actuation PIV in plane 1: difference in streamwise velocity between controlled and uncontrolled flow overlayed with streamlines. Dashed line: $\Psi = 0$.

The mean streamwise velocity field in PIV plane 2 and it's difference to the uncontrolled field is shown in figure 6.5 with the actuator spanwise positions marked by black squares. It bears pointing out that although the flowfield is extremely three-dimensional due to the nature of the applied control, it is relatively quasi-periodic and unlike for the uncontrolled flow, tunnel end effects don't seem to be that significant within the actuated span. Plane 2 lies below the trailing jet wakes at all points but they are still clearly visible in plane 2 by the low streamwise momentum imprints they leave. One can immediately notice, although the jet wakes curve as they move downstream, that they are slightly more tightly spaced than the actuators themselves. This is likely a product of the global inwash due to the increase in displacement thickness on the sidewalls of the tunnel.

Upstream of detachment between each of the actuators the streamwise velocity is increased with respect to the baseline, significantly between diverging actuators and slightly but noticeably between converging ones. In part this is just a consequence of the blockage introduced by the jets which causes the flow between them to accelerate, but this alone does not transfer flow energy towards the wall and would not explain a delay in separation. The more important feature is the artificial ejection and sweep pattern which this institutes and which does replenish momentum in the near wall flow.

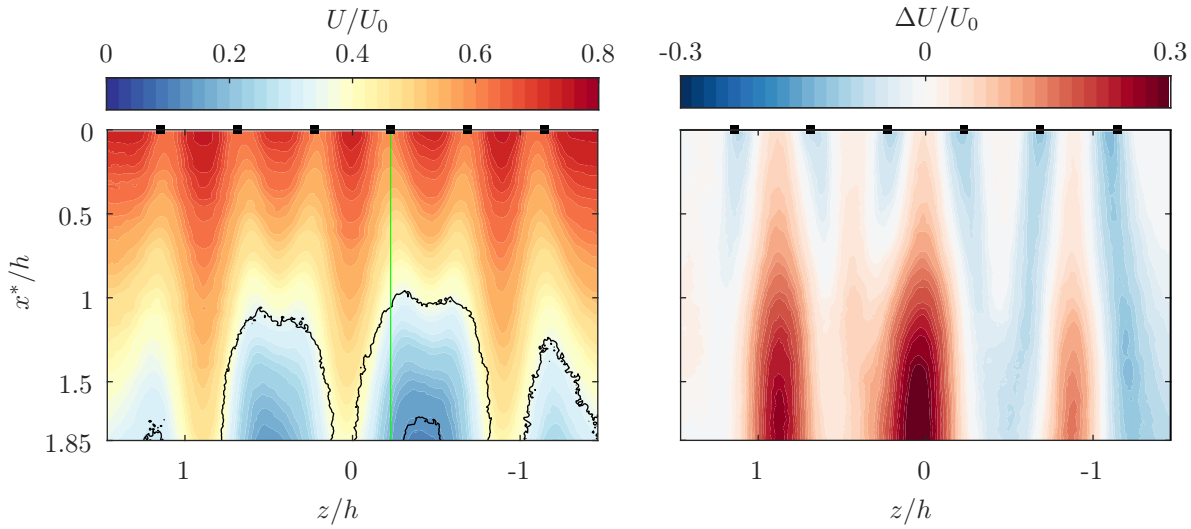

Figure 6.5: Mean streamwise velocity in plane 2 with 3D1 steady actuation: (*Left*) absolute velocity with contour lines indicating $\chi = 0.01$ and $\chi = 0.2$ and (*right*) velocity relative to uncontrolled field. Plane 1 position marked by green line.

This is confirmed by assessing the continuity residual, in this case the partial derivative $V^*_{y^*}$. At its upstream spanwise edge, plane 2 is positioned only 7 mm away from the wall and there is still no reverse flow. Therefore it is safe to make the assumption that along this edge V^* $V^*_{y^*}$, such that regions of negative $V^*_{y^*}$ indicate flow towards the wall and vice-versa. This is shown in figure 6.6. There are 3 regions of significant downwash between diverging actuator pairs and 2 regions of much weaker downwash between the converging pairs. Note that although every care was taken to minimize tilt of plane 2, due to the high wall-normal gradients at the location of the upstream edge of plane 2 even a low tilt still results in noticeable asymmetry.

Drawing on the results of other authors, such as Scholz et al. 2005, it is inferred from these flowfield features that in the time-averaged sense the jet-crossflow interaction in this case is generating a spanwise array of weakly lopsided trailing CRVPs as illustrated below the downwash plot in figure 6.6. For higher orifice skew angles the CRVP becomes effectively a single dominant vortex, as seen in the results of Scholz et al. 2005 who test a skew angle $\beta = 45°$, which would be expected to produce a pattern of alternating downwash and upwash (high and *low* momentum streaks) at the upstream edge of the plane. So in this case with a $\beta = 15°$, there are still clearly relatively balanced vortex *pairs* in play. Note that these aren't coherent vortices in the instantaneous flowfields, only features apparent in mean fields.

From observing the downstream half of plane 2, it's clear that in regions of high downwash separation is signficantly delayed, while in weak downwash regions the momentum at the downstream edge of plane 2 is relatively similar to the uncontrolled case. The flowfield as imaged in this plane therefore describes an alternating sweep/ejection pattern with a spanwise wavelength equal to twice the actuator spacing. A key feature of 3D actuation is that although the high momentum downwashing sweeps seem thin, this flow spreads laterally out into the nearby neighbouring low momentum ejection regions where detachment happens earlier. The downwashed momentum is therefore distributed more uniformly across the span than this single cut-plane would suggest. This is apparent from the high momentum forward flow observed just downstream of the reverse flow region in plane 1 (see figure 6.4) which is in fact flow from the central sweep spreading laterally out from $z = 0$.

Because of unequal downwash, the trajectories of the jet wakes bordering a strong downwash region curve away from each other. Eventually this leads to wakes interacting, which could be further negatively contributing to separation in those spanwise locations. To accomodate this spanwise motion, vortex generators are generally placed such that those with common downwash orientation are placed closer together, something which was not done here to allow for 3D2 experiments with alternating actuation.

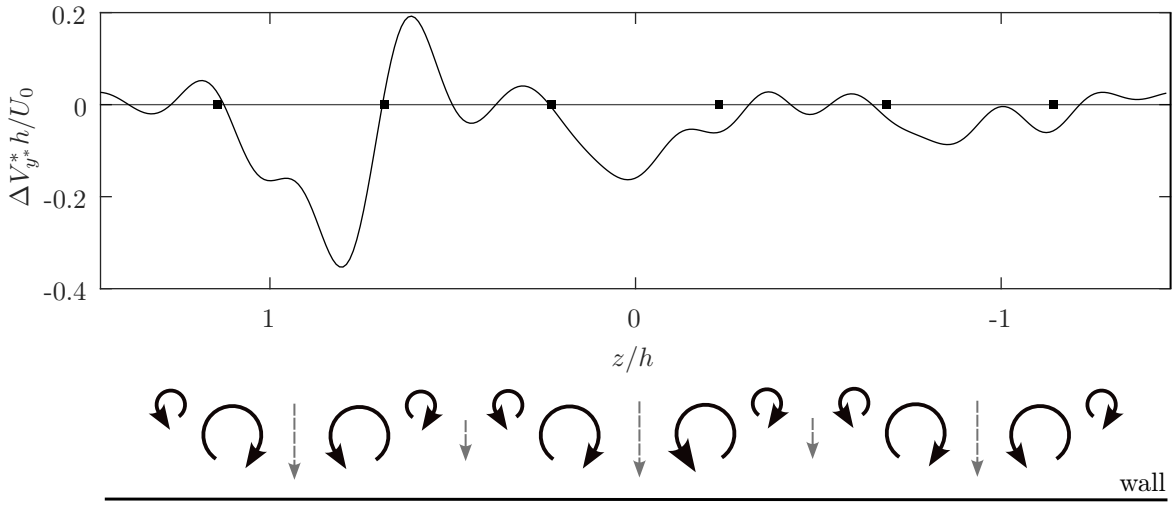

Figure 6.6: Change in wall-normal velocity derivative $V^*_{y^*}$ along the upstream edge of plane 2 with 3D1 steady actuation determined from continuity analysis and an appropriate time-averaged vortical model based on JCIF. Grey dashed arrows indicate downwash magnitude.

6.2.2. Upstream actuator row (3D1)

There are two key factors which are thought to contribute to 3D2 steady blowing severely underperforming 3D1. Firstly, the downstream row of actuators has 3 strong and 2 weak downwash regions, while the inverted upstream row has 2 strong and 3 weak downwash regions. With a large array, this would produce negligible differences in the global performance, but with this number of actuator pairs, 1 more strong downwashing pair is likely to have a significant impact on the net momentum transfer.

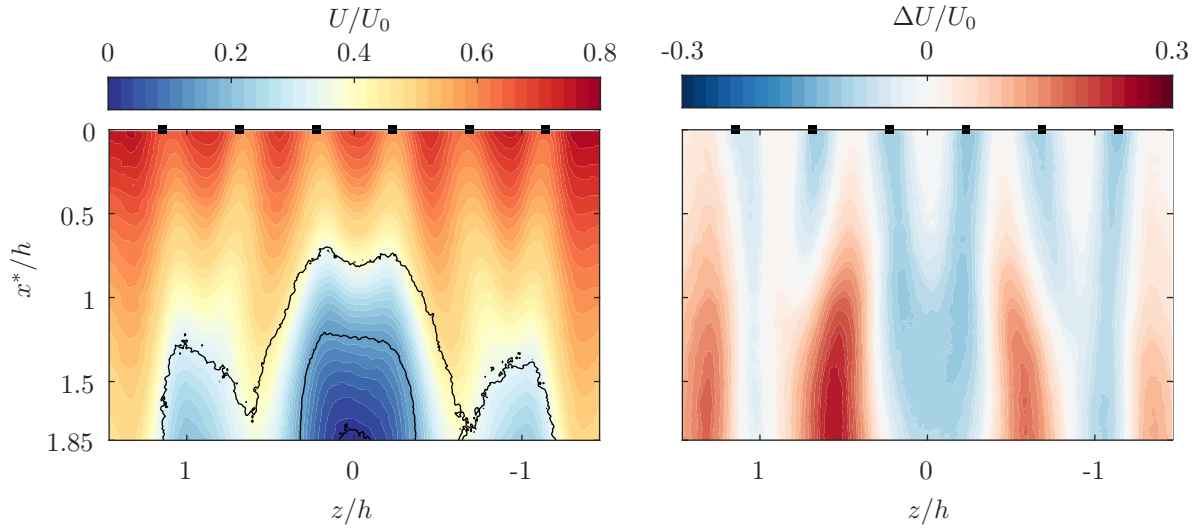

Figure 6.7: Mean streamwise velocity in plane 2 with 3D2 steady actuation: (*Left*) absolute velocity with contour lines indicating $\chi = 0.01$, $\chi = 0.2$ and $\chi = 0.5$ and (*right*) velocity relative to uncontrolled field.

Secondly, it was shown that the uncontrolled bubble is thickest in the tunnel centreline (see section 5.1). 3D1 steady blowing produces a strong downwash exactly along this line suppressing separation in this region, producing a more quasi-2D flowfield, while 3D2 does the exact opposite. This can be seen in the mean velocity field in plane 2 given in figure 6.7. The blockage along the centreline here is so severe that the diversion of the jet wakes around it is very noticeable. Furthermore, the bubble is tall

enough that there is reverse flow in plane 2, which is only seen in this case. This will then strongly bias metrics measured in plane 1, which runs through this region, and due to such a pronounced change in flow topology, will affect the momentum metric in plane 2 as well. Here we also note that in spite of this, a similar strong upstream move of the reattachment point is observed as for 3D1 actuation, and for the same reason. In this case the spanwise flow is towards the centreline from the two high momentum strips bordering the central bubble.

6.3. Unsteady actuation

As the performance overview showed, unsteady actuation has outperformed steady actuation in all metrics. Furthermore, actuation at a frequency commensurate with the natural frequency of the separation bubble has yielded the best performance out of all the actuation strategies tested. This section investigates the flow mechanisms involved, starting with the 3D1 cases and then briefly touching on 3D2 actuation.

6.3.1. Single row acutation (3D1)

The time-averaged streamwise velocity in plane 1 and 2 for LF and HF forcing is shown in figure 6.8. Compared to steady blowing the flow is more two-dimensional and, as is apparent from plane 1, the recirculation bubble now presents quite a well defined, almost closed region, which is significantly reduced compared to the baseline uncontrolled flow. The BM case is qualitatively the same as those shown here and differs quantitatively in a way which has been described by the metrics presented in the performance overview so they are not plotted here.

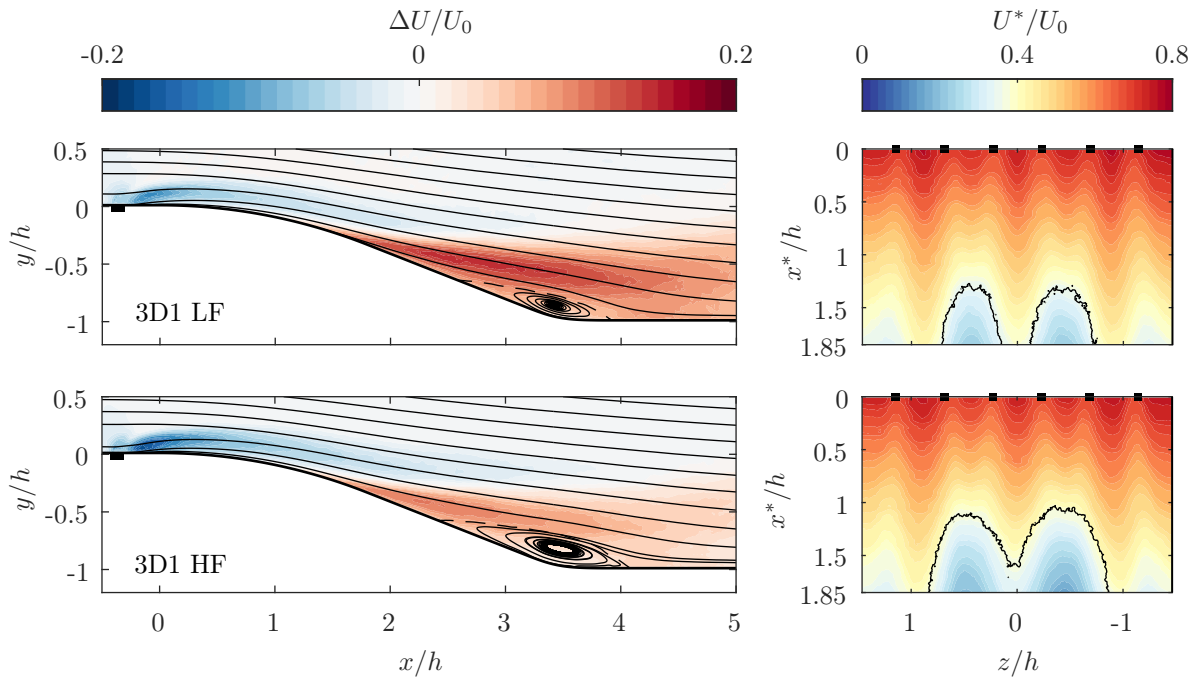

Figure 6.8: Mean streamwise velocity for 3D1 LF (top) and HF (bottom) actuation cases. Left: relative to uncontrolled flow in plane 1 with streamlines and $\Psi = 0$ overlayed, right: absolute in plane 2 with $\chi = 0.01$ contour line.

In separation control studies with fixed points of separation, the general finding is that actuation at the proper frequency is able to accelerate the growth of the shear layer structures, increasing entrainment from the recirculation region thereby reducing its extent (Bhattacharjee et al. 1986). This is observed as an increase in the turbulent activity of the shear layer. This is not found to be the case presently, as is clear from the TKE in plane 1 for the controlled and baseline cases shown in figure 6.9. Instead, the turbulent activity of the shear layer is found to be proportional to the size of the bubble so a stronger control effect correlates to weaker, not amplified shear layer turbulent fluctuation. This agrees with the

results of other pressure-induced separation bubble studies, most notably that of Mohammed-Taifour and Weiss 2021, in which the authors draw from these findings the conclusion that a modification of shear layer dynamics is not the primary separation control mechanism at play.

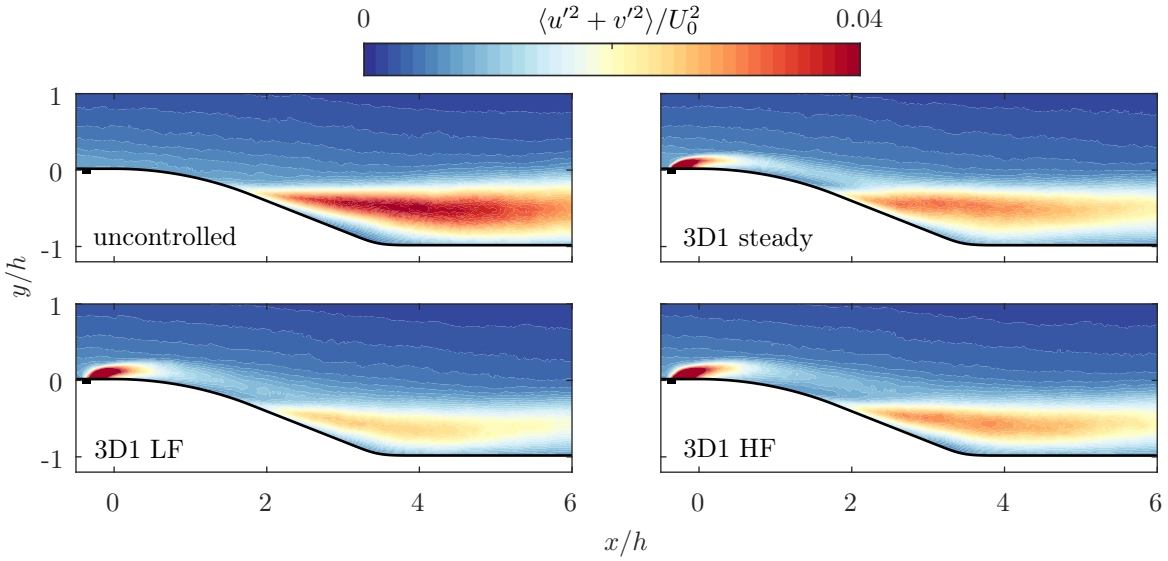

Figure 6.9: Variance (turbulent kinetic energy) in plane 1 for uncontrolled and 3D1 steady, LF and HF cases.

For further analysis, a triple decomposition is carried out on the velocity fields using a phase-averaging approach. The harmonic fluctuation energy $\tilde{k}$, determined as the variance of the phase-averaged velocity, is shown in figure 6.10 as a proportion of the total fluctuation kinetic energy. At its maximum, directly behind the jet, the harmonic energy does not pass 50% of the total TKE, which speaks to the turbulence intensity of the incoming boundary layer as the intensity of the perturbation introduced into the flowfield by the jets is only of similar magnitude.

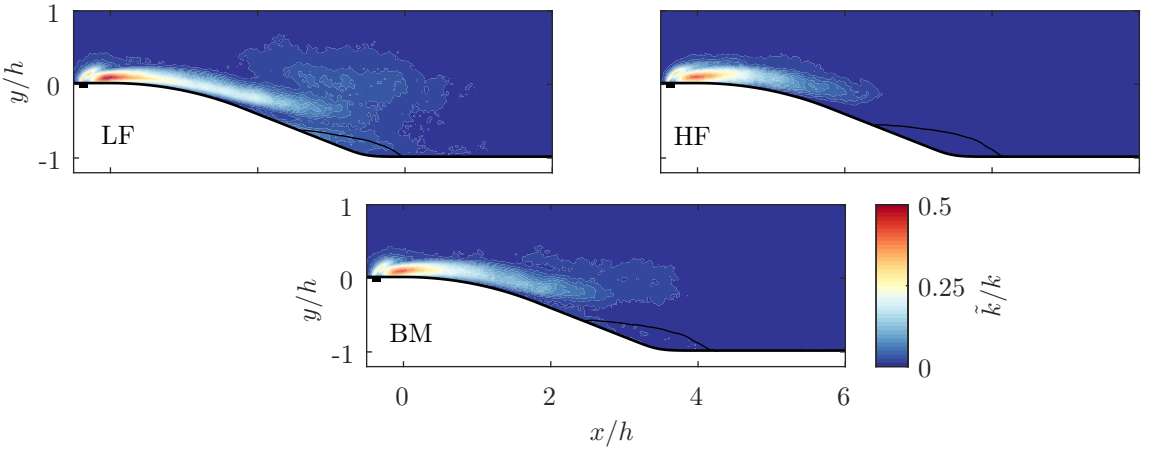

Figure 6.10: Ratio of harmonic kinetic energy $\tilde{k}$ and total turbulent kinetic energy k for 3D1 unsteady control cases.

Notably, while for HF forcing there is no apparent harmonic response downstream of detachment and outside of the jet wake, for LF forcing there is significant harmonic content present throughout the separation bubble, slightly downstream of it and quite far away from the wall. BM sits between these two cases, showing some harmonic response around the point of detachment but none through the downstream region of the bubble. These results indicate that actuation at a frequency close to the natural fluctuation frequency of the bubble is able to *phase-lock* the bubble oscillation to the applied

control. Note however that even for LF forcing, what is here considered a significant harmonic content amounts to no more than $\tilde{k}/k \approx 0.2$ at the point of detachment, which again shows how strong the turbulence of the tested boundary layer is compared to the introduced perturbation.

Figure 6.11 shows how exactly the bubble geometry changes through the actuation period for all 3D1 cases. The lines indicate data which has been phase-averaged by binning the period into 8 bins yielding approximately 370 images per bin. The markers meanwhile indicate phase-locked data, with 1500 images per acquisition. Interestingly, although a bit noisy, the binned data shows a satisfying degree of agreement with the phase-locked data. The results echo those related to harmonic fluctuation energy $\tilde{k}$, showing the HF case to be quasi-steady while LF forcing causes a significant oscillation of the bubble geometry all the while keeping it smaller than in the other cases. BM shows some oscillation around the point of detachment but very little otherwise. Notably, both LF and BM forcing exhibit a smooth slow downstream move of the point of detachment followed by a sudden rebound upstream, that actually closely coincides with the point of minimum bubble area.

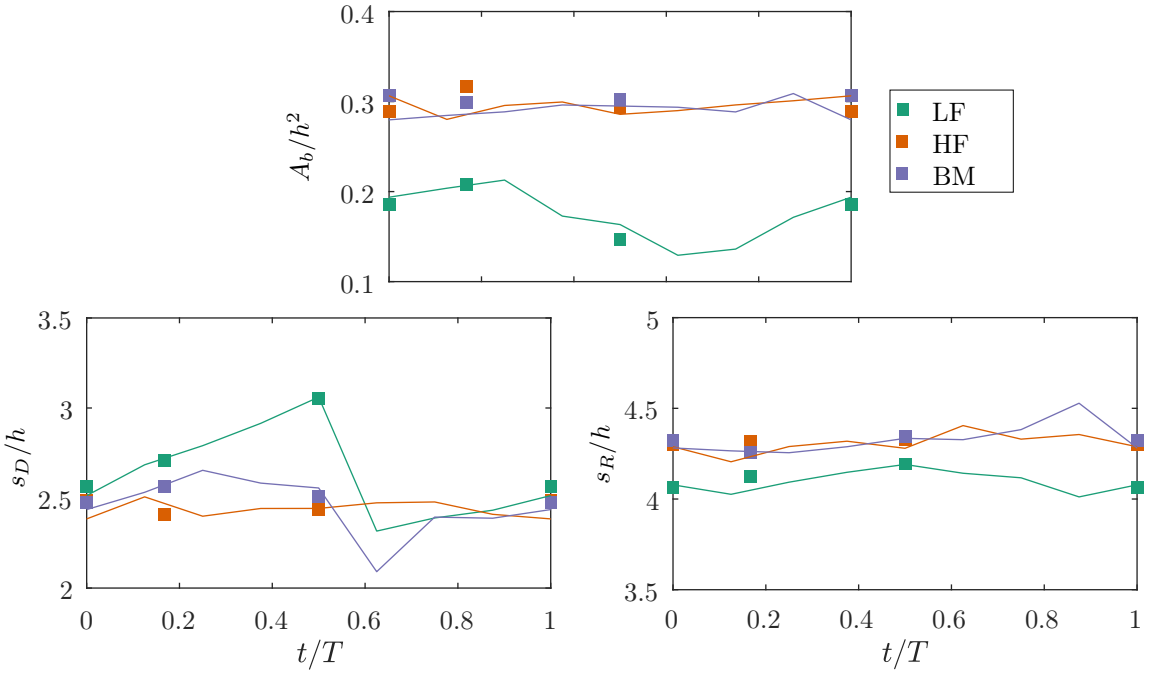

Figure 6.11: Phase evolution of bubble size A_b and point of detachment/reattachment s_D/s_R (lines: phase-averaged by binning, markers: phase-locked acquisitions).

The detachment point reacts a lot more than the point of reattachment to periodic control (they are plotted in the same scale), indicating that most of the separation suppression comes from a separation delay enabled by momentum transfer to the wall upstream of separation. This is another indication that the main control mechanism is not a modulation of the shear layer dynamics, as that generally results in significant periodic oscillations of the reattachment point driven by the strongly varying entrainment rate from the bubble, such as in the study of Wu et al. 2022. This could however be a feature of differences in the experimental set-up, as the reattachment is somewhat forced in the present case by the detached flow impinging on the downstream tunnel wall, with the region of intermittent detachment being almost as large as that of reattachment. The case studied by Mohammed-Taifour and Weiss 2021 is similar in this regard and reports similar observations, much like for the shear layer turbulent activity findings.

As before, plane 2 data is useful because plane 1 cannot be used in directly comparing the cases across phase and span. Furthermore, since plane 1 runs through the jet wakes, it provides no information on the downwash regions between the jets. Figure 6.12 shows the phase-averaged response of the streamwise velocity U^* to LF and HF actuation at the upstream and downstream spanwise edges of plane 2. For reference, the upstream edge sits approximately halfway between the actuators and the point of detachment and is very near the wall at $y \approx 7$ mm. The downstream edge meanwhile is in the immediate vicinity of the recirculation bubble upstream edge. The former is therefore used as an

indicator of the upstream BL actuation response, while the latter serves as an indirect indicator of separation delay. The left plots show the time and phase-averaged velocity profiles at both plane edges, while plots on the right show the phase-averaged velocity response in the central strong downwash region ($z = 0$) on both edges.

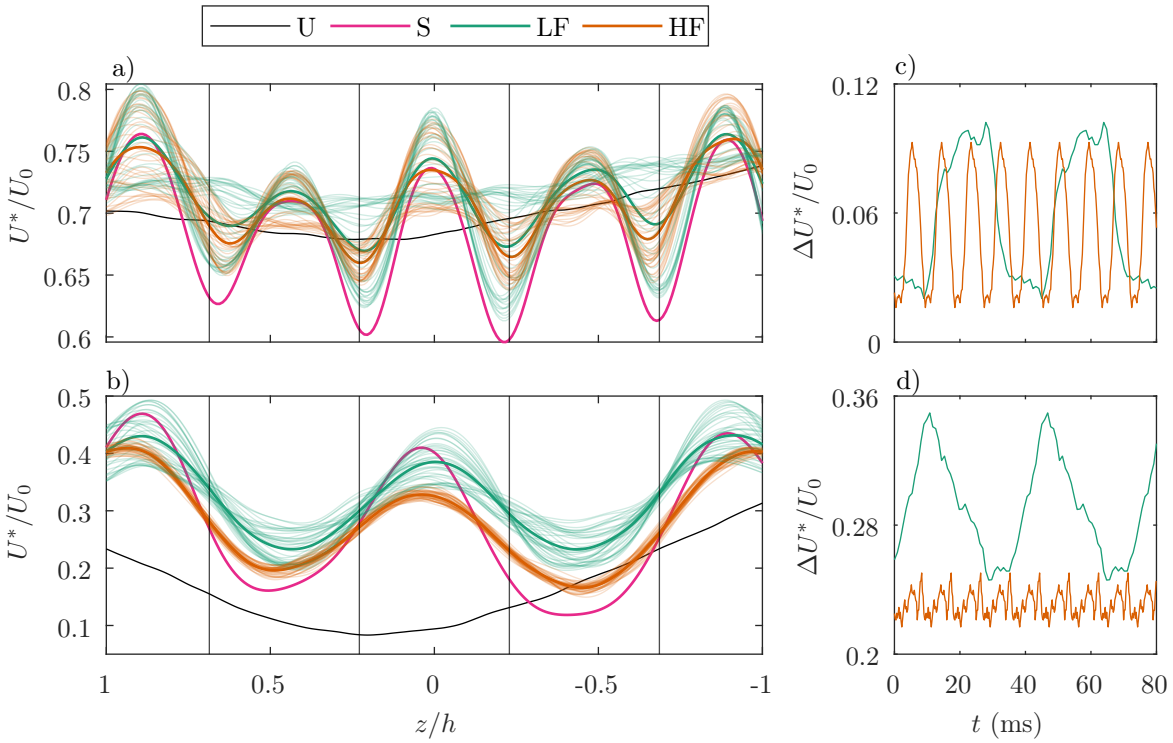

Figure 6.12: Streamwise velocity U^* in plane 2 for steady and 3D1 LF and HF control. Time and phase averaged velocity profiles at (a) upstream and (b) downstream edges of plane 2 edges (thick line: time average, thin lines: phase average). Phase-averaged velocity response at $z = 0$ on the (c) upstream and (d) downstream edge given as difference to uncontrolled.

The streamwise momentum in the upstream BL exhibits a very rapid temporal response (figure 6.12a/c) for both LF and HF forcing, even quite similar in terms of amplitude and rise and decay times. The only notable difference is that in LF forcing, the pulses are long enough that a steady value is reached and maintained for a portion of the pulse prior to decay. So while the response is not instantaneous, it is rapid enough that even HF forcing produces a full oscillation. Near detachment on the other hand (figure 6.12b/d), while LF forcing still produces a significant oscillation between a state similar to that achieved by steady blowing and a relatively relaxed 2D state, HF forcing produces an essentially quasi-steady sweep/ejection pattern showing very little coherent oscillation. So while it was already apparent that the actuated flowfield has the frequency response of a low-pass filter, now it's clear that the separation bubble is the main source of "inertia" in the flowfield with the dominant response time τ_b. Comparatively, downwash is induced rapidly in the upstream BL by the jets.

Mohammed-Taifour and Weiss 2021 further pursued this matter by studying the transients following an abrupt actuation start and stop. This allowed them to actually measure the bubble response time to be lower than the spectral peak associated to the shedding mode and actually related to the low frequency breathing mode which has not been detected in this work. Presently, due to a lack of transient measurements, a bubble response time cannot be accurately determined, but it can be estimated from the measured frequency response. Firstly, based on purely empirical reasoning, if the actuation was carried out at a time scale larger than τ_b, one would expect to see an oscillatory response that asymptotically approaches the two steady state extremes. The triangular LF temporal response (figure 6.12d) therefore suggests that τ_b is of similar order or larger than the time scale of LF actuation and therefore also the spectral peak of the unforced bubble.

A more mathematical proof of this is obtained if, in a first approximation, the bubble is modeled as

a first order dynamical system with a sinusoidal input, that produces the classic low-pass filter Bode plot with a horizontal and declining asymptote intersecting at the cut-off frequency $f_{co} = 1/\tau_b$. For this model system, the ratio of the bubble response amplitudes in the LF and HF cases is given by expression 6.3.

$$\frac{A_l}{A_h} = \frac{\sqrt{1 + 4\pi^2 f_h^2 \tau_b^2}}{\sqrt{1 + 4\pi^2 f_l^2 \tau_b^2}} \tag{6.3}$$

As the bubble cut-off frequency f_{co} is reduced to the level of f_l or below, the amplitude ratio A_l/A_h tends to a value of f_h/f_l. In this case both actuation frequencies lie in the declining asymptote region of the Bode plot. In the data presented in figure 6.12, in the regions between the actuators this ratio is indeed measured at approximately $f_h/f_l = 4$ which suggests accordingly that f_{co} is close to or lower than the LF actuation frequency f_l.

A common feature of all unsteady actuation cases, including the ones not shown here, is a more spanwise uniform flowfield compared to steady blowing. Since this occurs irrespectively of the magnitude of coherent bubble oscillation as evidenced by HF forcing, it has to be the result of the oscillation between the active blowing period and the inactive relaxation period in the upstream boundary layer (figure 6.12a). The consequence of this is a more a spanwise uniform momentum distribution in the boundary layer which ultimately leads to a more spanwise uniform separation delay (figure 6.12b). It is also noteworthy that LF and HF show a very similar spanwise variance in the time average, meaning this effect is unrelated to frequency. However, because BM forcing exhibits an even lower spanwise variance (see figure A.1), it's likely this is related to the effective duty cycle, which for BM is 0.33. This is natural to expect since an increased inactive portion of the period will lead to a more 2D time-averaged effect.

Another thing to note is that the jet wake signatures in plane 2 have higher momentum in the unsteady cases, not just in the time-averaged sense but also during the active blowing phase. This is not related to the jet structure but rather to its trajectory. As seen in figure 6.13, the unsteady blowing cases achieve higher penetration into the crossflow resulting in a jet trajectory higer above plane 2, which explains why their signature in the plane is weaker.

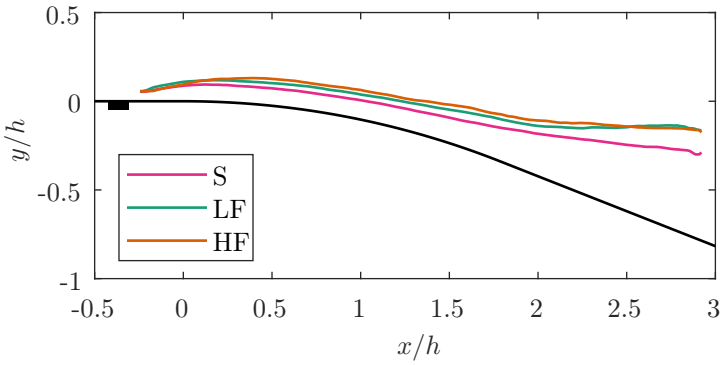

Figure 6.13: Time-averaged jet trajectory for 3D1 control cases. Determined as the minimum in the streamwise velocity profile.

For HF forcing, which achieves similar time-averaged downwash between actuators as steady blowing, the raised jet trajectory and the lateral momentum transfer from areas with downwash in the upstream BL are plausible explanations for the slight performance benefit identified with respect to steady blowing. However, LF forcing has been shown to significantly outperform all other actuation strategies and these factors cannot be the sole explanation since they are relatively similar between LF and HF cases.

In the time-averaged sense LF achieves higher streamwise velocities than HF across most of the span at the upstream edge and across the entire span at the downstream edge of plane 2. Interestingly, the similar spanwise variance between the two cases means the offset between them is relatively constant across the span, including in both strong and weak downwash regions and directly downstream of the actuators. This strongly suggests that the flow feature driving it is itself a spanwise uniform high momentum flow feature, unlike the actuation structures produced during active blowing periods. In fact, the spanwise profiles of figure 6.12a show that during active blowing the peak streamwise momentum values achieved between the actuators are relatively similar between the LF and HF cases. The important

difference between the cases is actually seen during the inactive relaxation periods. In the LF case, the BL relaxes to a relatively two-dimensional state with the same spanwise profile shape as the uncontrolled flow but crucially, a higher streamwise momentum. This is indicative of a high momentum sweep occuring across the span between actuator pulses. Because of this, during the inactive period LF retains a much higher momentum value in the downwashing regions between actuators and rises to a much higher value downstream of the actuators.

To further characterize this, phase-averaged velocity fields for four points in the period of LF actuation are shown in figure 6.14. The first three points are phase-locked acquisitions while the last point has been obtained by binning. The same plots for the HF and BM cases are provided in figures A.2 and A.3 in the appendix.

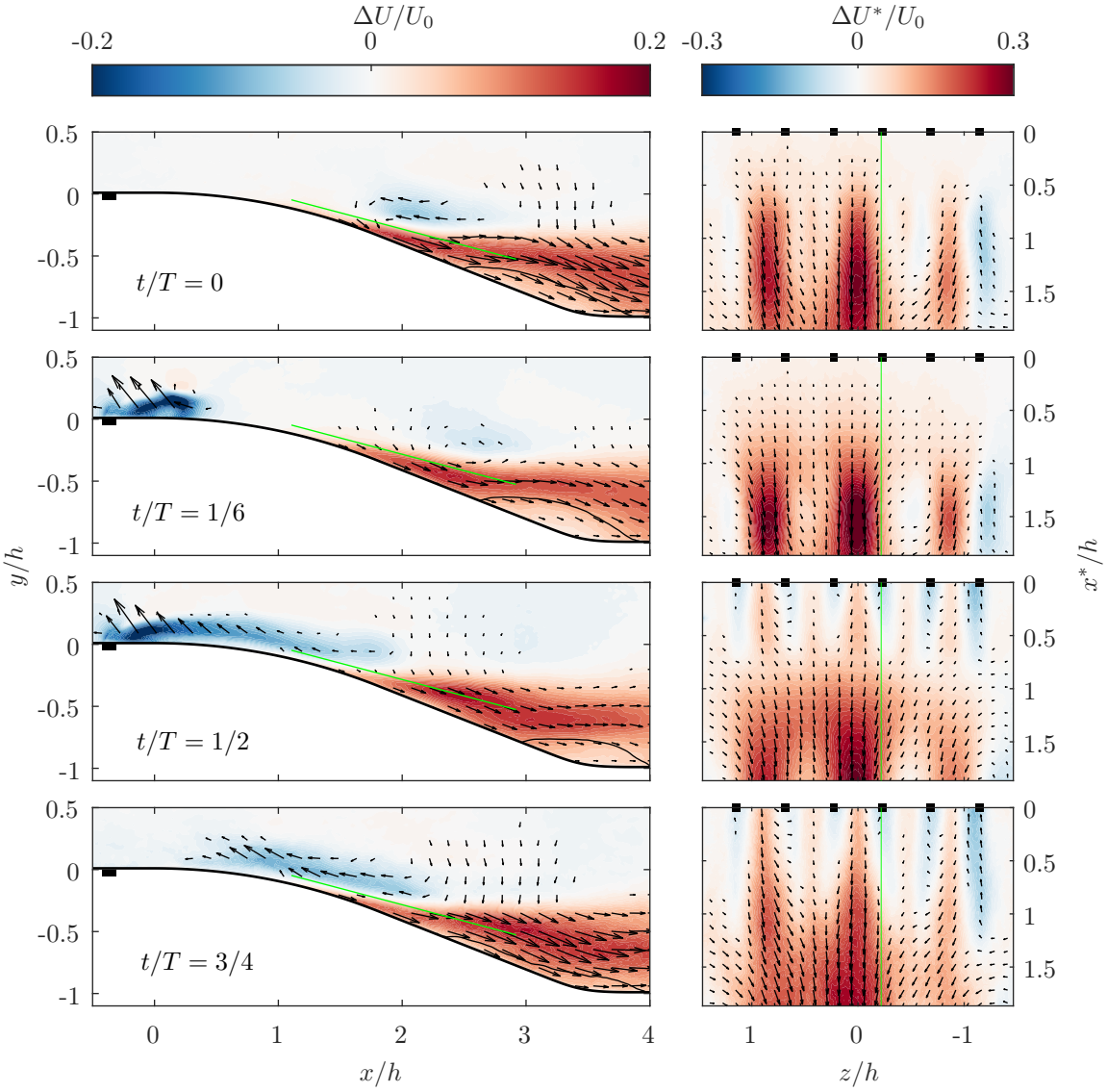

Figure 6.14: Phase averaged velocity fields for 3D1 LF forcing shown relative to the uncontrolled baseline. Green lines: PIV plane intersection.

From around $t/T = 0$ to $t/T = 1/6$ the structure of the previous actuation period stretches across the entire length of the bubble and just before it passes, the bubble becomes very similar to that observed in steady actuation. The peak streamwise momentum at the downstream edge of plane 2 is achieved at the end of this phase (at $t/T \approx 0.3$) in the strong downwash regions. After the passage of this and until the arrival of the next structure the flowfield relaxes to a more 2D shape. This process is marked by a relatively significant high momentum spanwise uniform sweep. The detachment point is pushed to

its most downstream point (at $t/T = 0.5$) and shortly thereafter rebounds suddenly upstream. In the process the bubble takes a thin elongated form reaching the smallest area (in plane 1) of the period at $t/T = 0.75$ just as the head of the next actuation structure, which is visibly more pronounced than the rest of the structure, reaches the bubble. This is also the point in the period when the smallest spanwise variance in velocity is achieved at the downstream edge of plane 2, just before the 3D sweep/ejection pattern starts forming again repeating the process.

As already suggested by the spanwise profiles in figure 6.12, the spanwise uniform high momentum sweep between pulses is not observed in the HF forcing case. It is however observed with BM forcing (see figure A.1 in the appendix), although it is in that case weaker. This is a clear indication that the time scale of sweep formation is longer than $\tau_h = 1/f_h$, with the separation of actuation structures in the case of HF forcing being simply too short for it to occur. As such this is thought to be related to the transient relaxation of the bubble (occuring at bubble time scales τ_b) from a 3D state with significantly increased net downwash to the uncontrolled state, which is cut short by the next actuation pulse. The key feature of this sweep is that it leads to a *net increase* in downwash over the ramp, not just a prolonged decay. A potential explanation for this behaviour is that while the jet structures are essential to inducing downwash over the ramp, they are at the same time wakes with very low streamwise momentum. The passage of a row of actuation structures is therefore followed by a temporary drop in blockage over the ramp which combined with the slow decay in induced downwash could reasonably be expected to yield a transient net increase in streamwise momentum.

The outlined difference in flow dynamics between the cases has an interesting effect on the BL momentum deficit downstream of the ramp. As expected, the time-averaged BL profiles in figure 6.15 show how increasing control effectiveness reduces the "wake" of the ramp thus reducing the momentum deficit of the measured boundary layer with respect to the EIF.

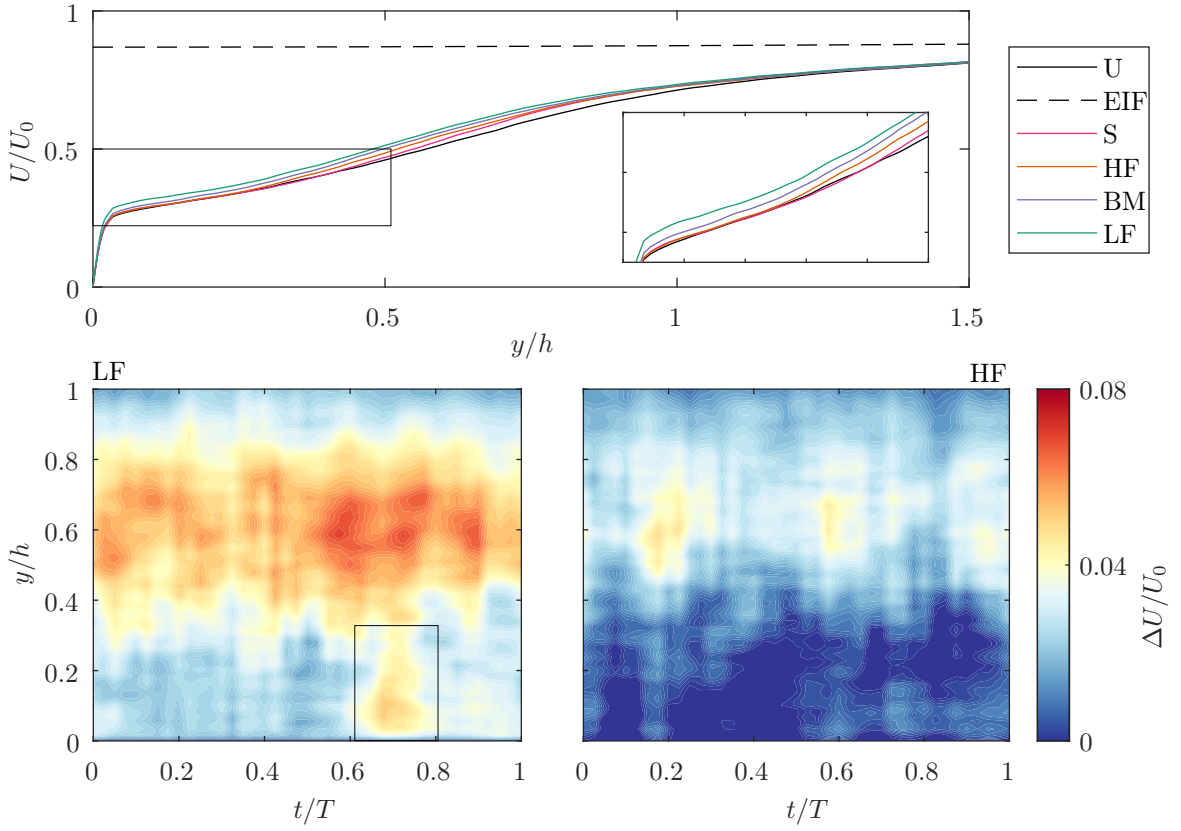

Figure 6.15: Effect of 3D1 unsteady actuation on BL downstream of reattachment at $x/h = 6.25$: (*top*) comparison of uncontrolled and 3D1 time-averaged profiles, (*bottom*) phase-averaged BL velocity as difference to uncontrolled for LF and HF cases.

However, of particular interest here is how LF and BM forcing increase the flow momentum across

the entire BL height, including in the very near wall region ($y/h < 0.3$), where neither steady nor HF forcing have any effect. Ofcourse, BM forcing has a much weaker effect than LF, but topologically similar nonetheless. Specifically, as discussed above, when forcing at time-scales comparable to that of the bubble there is a point in the actuation period where the sweep between active periods convects over the bubble and the bubble takes an extremely thin elongated form. Consequently, high momentum is transferred all the way to the wall which is visible in the BL velocity-phase plot for LF forcing in figure 6.15 at $t/T = 0.6 - 0.8$.

While the discussed sweep is spanwise uniform in the phase-averaged sense, instantaneously it is dominantly made up of streamwise elongated structures, largely the same as those observed in the uncontrolled flow. This is shown by the autocorrelation of the streamwise velocity for LF actuation at $t/T = 1/6$ in figure 6.16. The spanwise length scale l_z is also similar to uncontrolled flow $l_z \approx 0.33\delta$ and is relatively constant across the span. What variance there is, is uncorrelated to the perturbation spanwise wavelength, so this instantaneous structure seems to be purely a function of the incoming boundary layer turbulence.

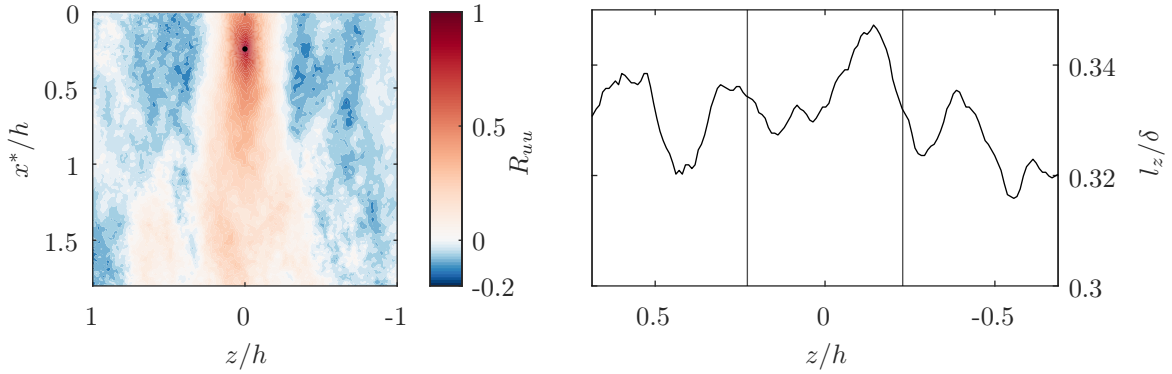

Figure 6.16: Autocorrelation of streamwise velocity fluctuation for 3D1 LF actuation at $t/T = 1/6$: (*left*) contours, (*right*) spanwise length scale across the span. Actuator locations marked by vertical lines.

6.3.2. Alternating row actuation (3D2)

The alternating 3D2 actuation cases display all of the features identified in the preceding section as contributing to the observed effects of unsteady forcing and specifically the timescales at which it is applied. This is why 3D2 LF actuation again clearly outperforms 3D2 BM and HF in that order. These are:

- increased periodic oscillation of the bubble in phase with actuation when forcing is applied in the dominant natural frequency range,
- high momentum sweeps, spanwise coherent in the phase-averaged sense, between the passage of actuation structures when forcing at f_l and
- reduced shear layer activity with a reduction in separation bubble size.

But what remains of interest is why, while 3D2 LF produces virtually the same performance as 3D1 LF, there is a large performance difference in the case of HF forcing.

This is best explained by again considering the streamwise velocity U^* at the downstream edge of plane 2, shown for all unsteady cases in figure 6.17. All 3 actuation methods produce a time-averaged velocity profile that matches the uncontrolled profile in shape and if not for tunnel end effects, this would tend to a spanwise constant velocity. For the LF case, there is sufficient time in the actuation period for the sweep/ejection pattern to form for both actuation pulses. Ultimately the result of this is that in the time-averaged sense 3D2 outperforms 3D1 in the ejection regions of 3D1 by about the same amount that it underperform in the sweep regions, yielding overall a similar performance.

Meanwhile, 3D2 HF produces a quasi-steady response just like 3D1. However, in the 3D1 case this quasi-steady response is a sweep/ejection pattern similar to steady blowing, with the sweeps bringing a lot of high momentum into the entire bubble. The 3D2 case meanwhile produces a spanwise invariant time averaged effect while never actually forming strong momentum sweeps because each pulse actively

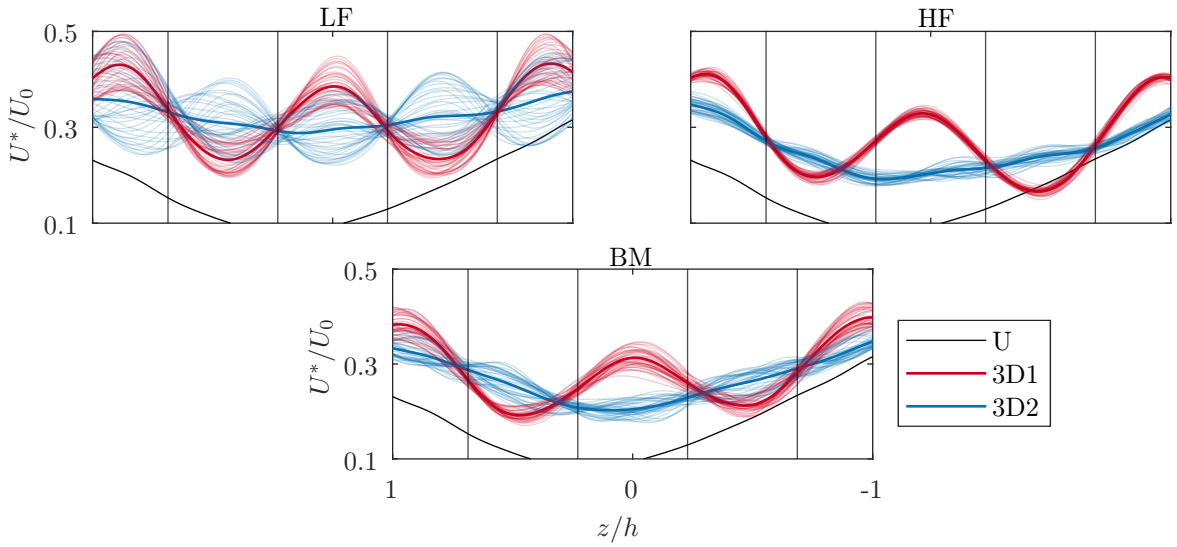

Figure 6.17: Streamwise velocity U^* at downstream edge of plane 2 for 3D1 and 3D2 unsteady cases. Thick line: time average, thin lines: phase average.

interferes with the preceding one. There is never enough time given to the separation bubble for a global adjustment of pressure and velocity fields that would lead to a significant increase in downwash. Clearly this severely limits the net momentum improvement in the bubble as the 3D2 HF case significantly underperforms compared to 3D1 HF.

As a reminder, the main concept behind the alternating 3D2 actuation strategy was the alternating BM forcing case, which aimed to leverage the inertia of the separation bubble to produce a quasi-2D actuation acting at the lower modulation frequency and in so doing strengthen the modulation of the shear layer while retaining the benefits of 3D actuation. In the present case, as it turns out the shear layer modulation does not play a significant part in separation suppression, so this cannot be fully answered. However, what is shown is that high frequency alternation (in relation to the bubble timescales) of the *intended* actuation sweep/ejection pattern prevents it from ever being fully formed, thus nullifying one of the key features of 3D actuation. So while a quasi-2D effect is achieved, a significant amount of performance is lost.

7

Conclusions and Recommendations

This research project has developed an array of pulsed vortex generating jets and successfully applied it to control separation of a high Reynolds number turbulent boundary layer over a curved backwards facing ramp. A thorough investigation of the controlled flow in various operating modes was carried out. Parametric sweeps of actuation momentum and frequency were performed to determine optimum operating parameters. Select cases of interest were then analyzed in detail using 2D-2C PIV in 2 planes relying on phase averaging to identify coherent actuation structures. To provide a basis for understanding features observed in the controlled flow, the baseline uncontrolled flow and the actuator were characterized independently, the actuator being tested in quiescent surroundings. Conclusions following from the discussion of results in the preceding chapters are summarized here. They are separated into those pertaining to the baseline uncontrolled flow and those pertaining to separation control.

7.1. Uncontrolled flow

The flow was found to be relatively three-dimensional owing to the limited aspect ratio of the separation ramp. Away from the sidewalls, the separation bubble was found to be thickest along the plane of symmetry, where separation happened at approximately halfway down the ramp, at the end of the curved ramp shoulder. The upstream boundary layer was found to have a large wake, owing to the sustained adverse pressure gradient imposed on it even before the ramp. An investigation of the BL parameters showed that detachment occurs at a shape factor of $H_{sep} = 2.01$. This is around the middle of the range reported by Cebeci and Bradshaw 1977 which shows that separation was dominantly driven by an adverse pressure gradient rather than curvature.

Due to the high near wall concentration of vorticity in the separating TBL, evidence of sub-shear layer development was observed, where only a near-wall portion of the boundary layer vorticity participated in the initial shear layer instability and roll-up. The bubble length was sufficiently small compared to the momentum thickness of the separating boundary layer, that the developing shear layer never fully envelops the boundary layer.

Hot wire spectra taken along the separated shear layer showed an increasing amount of turbulent kinetic energy contained around a relatively broadband peak at $St_h \approx 0.08 - 0.2$. The measured frequency agrees well with results reported for other similar separations and even for turbulent mixing layers, where it is reported as the vortex shedding frequency. In this case, an investigation of the flow spatial structure showed no spanwise coherent motions, with the dominant unsteadiness being a pattern of streamwise elongated sweeps and ejections corresponding to known features of the large streamwise motions of the TBL.

The outer peak in the spectrum of the incoming boundary layer, related to the passage of these structures, was found to correspond to the spectral peak of the separation bubble and predicted well by assuming a KH mechanism. This suggests that there is a strong coupling between the turbulent dynamics of the upstream BL and the separation bubble which isn't surprising considering they are of similar scales.

7.2. Controlled flow

With successful separation control, the static pressure profile measured along the wall tends towards a hypothetical inviscid flow. Higher adverse pressure gradients are sustained leading to an overall larger pressure recovery. As the viscous displacement thickness and in particular the separation bubble are reduced, the streamline curvature on the upstream portion of the ramp is increased which lowers the pressure of the ramp suction peak. This behaviour is leveraged to define a static pressure based control effectiveness metric which is used for control parameter sweeps.

An actuation momentum sweep was performed for the case of steady blowing and showed that actuation below a crossover velocity ratio $VR \approx 1$ actually worsened separation. With an increase in VR past this value the performance initially quickly improved and then showed signs of tailing off. From what is known about jet-crossflow interactions, for $VR < 1$ the jet is severely affected by the crossflow momentum and the resultant flowfield regime very sensitive to small changes in the boundary conditions. The results suggest that, at least for steady blowing, this regime is not conducive to separation delay. For all further control study a value of $VR = 1.6$ ($C_\mu = 2.3\%$) was selected, as this was found closest to an inflection point in the performance trend of the steady blowing momentum sweep.

Further investigation of steady blowing indicates that separation delay and a reduction in the bubble size is driven by downwash between the jet wakes bringing high momentum towards the wall. Diverging actuator pairs produce strong downwash regions where separation is significantly suppressed (sweeps), while converging actuator pairs produced weak downwash regions where the effect on the detachment point compared to the uncontrolled flow was negligible (ejections). However, even in weak downwash regions the reverse flow region is still significantly affected because the high momentum flow from sweep regions flows laterally into neighbouring ejection regions.

Unsteady forcing was found to achieve better or comparable results to steady actuation depending on frequency, while nominally requiring less input momentum ($C_\mu = 1.2 - 1.8\%$), confirming widely reported results. A frequency sweep of actuation with a 50% duty cycle showed a clear optimum actuation frequency range of $St_h = 0.08 - 0.16$, which corresponds to the dominant frequency range of the uncontrolled separation bubble. At frequencies higher than this range the control effect slowly tended to the steady actuation levels of performance. An analysis of the phase-averaged flow dynamics showed that forcing at frequencies in the range of the uncontrolled bubble spectral peak (LF) produces a strong harmonic bubble response in phase with actuation, while forcing at a frequency 4 times higher (HF) yields a quasi-steady effect on the bubble. Since the boundary layer upstream of the bubble is found to respond rapidly to actuation, this low-pass filtering behaviour is attributed to the bubble itself.

The resonant behaviour achieved by forcing at the natural bubble time scales is associated with the occurence of high momentum sweeps, spanwise uniform in the phase-averaged sense, between actuation pulses which lead to the observed control performance benefits. They are thought to occur because of a combination of two factors: the delayed decay of induced downwash over the ramp and the passage of low streamwise momentum jet wakes. The former is simply the transient bubble relaxation from a high net downwash state towards an uncontrolled state, which is interrupted by the next actuation pulse. Regarding the latter, while the jet structures are fundamental to the separation control process, having low streamwise momentum cores they introduce blockage into the ramp flow. Therefore just after the passage of the previous row of structures, there is still high residual downwash on account of the bubble response time but also a sudden drop in blockage which combine to produce a high momentum sweep across the ramp span.

Unlike what is often reported in the case of geometry-induced separation control, no evidence has been found that modulation of the shear layer development contributes significantly to the measured performance, even though the measured frequency sensitivity would suggest it. Firstly, improved control and a reduction in the size of the separation bubble was correlated with reduced rather than increased turbulent activity in the separated shear layer. Secondly, the location of detachment varied with control significantly more than that of reattachment, which is notably different to cases where the shear layer is significantly modulated.

These findings illustrate certain implications for engineering applications. The absolute best separation control performance can be achieved by unsteady actuation at frequencies close to the natural frequencies of the flow. However, this performance benefit over steady or higher frequency actuation is produced by amplification of flow unsteadiness which then necessarily results in strong and relatively coherent oscillation of loads. If this is an issue then steady or higher frequency forcing will be prefered. For high forcing frequencies, around 4 times larger than the natural flow frequency and above, the overall

effect becomes very similar to that of steady actuation, both in terms of performance and unsteadiness. In these cases the choice of optimal actuation strategy comes down to other system parameters. For example, while high frequency forcing uses less massflow, it requires a continuous power supply to operate the valves.

The proposed 3D2 actuation strategy in which two inverted actuator rows are alternately fired with the aim of producing a quasi-2D effect yielded unsatisfactory results. Although a high-frequency alternation did generate a quasi-2D effect, it hindered the formation of the characteristic sweep/ejection pattern associated with 3D actuation. As a result, the performance of the actuators was significantly limited. Simultaneously, since the modulation of flowfield shear layer instability was determined to be an insignificant control mechanism in the current scenario, no potential impacts of this two-dimensionalized perturbation on it have been identified.

7.3. Recommendations

Questions left unanswered during this research and follow-up questions are summarized here as recommendations for future work and are split into those relating to the actuator design and operation and those relating to experimental methodology.

7.3.1. Actuator design and operation

The postulated mechanism by which high momentum spanwise uniform sweeps occur between actuation pulses should be further investigated. This would require firstly transient measurements, in which a periodic control input is impulsively started and stopped. This would yield flow dynamics related only to the upstream or downstream actuation structures respectively, taking the influence of the other out of the equation. Notably, the heads (starting structures) of the incoming actuation structures have been identified by some to be of high importance (Zhong and Zhang 2013). Since no clear induced downwash is seen downstream of the head at $t/T = 1/6$, it does not seem to be the case presently, but transient measurements could shed further light on this. Furthermore, more actuation frequencies should be investigated with PIV to assess how the sweep is affected.

This research strongly focused on actuation frequency and timing, while the impacts of jet velocity were only tested in a preliminary sweep of steady blowing with no flow visualization techniques. It would therefore be useful to do this, particularly focusing on the crossover range of velocity ratios around $VR = 1$ and to assess how these trends are impacted by unsteady actuation.

Including VGJ design parameters in the explored parametric space would be of interest. In particular, this would involve assessing the impact of spanwise jet spacing on performance. As discussed in the context of actuator design (section 3.1.2), the initial jet spacing set in the design was too low and negatively impacted separation. Between that and infinite spacing there is bound to be an optimum and it would be interesting to see where this optimum is in relation to the spanwise length scale of the large structures of the TBL.

Future investigation could also look into expanding this system with sensors, implementing either feedforward of feedback control. In feedforward control hot film sensors could be placed upstream of the jets to detect large streamwise elongated high or low momentum regions in the incoming boundary layer and then the input actuation momentum adjusted depending on the spanwise location by adjusting pulse durations. This could lower the required momentum input for the same control effect by utilizing the natural sweep/ejection pattern occuring in the TBL.

In the present work, the modulation of the shear layer instability was not found to have a significant impact on separation control, much like for other work done on pressure-induced separations. It would then be of interest to test the alternating actuation strategy, which demonstrated a weaker but definitely more two-dimensional effect than the conventional non-alternating strategy, on a geometry-induced separation for which shear layer modulation is generally cited as the main control mechanism and for which 2D actuation is considered more optimal.

7.3.2. Experimental methodology

For a future investigation it would be desirable to solve some of the experimental shortcomings of this research. Chief among these is increasing the span, and consequently aspect ratio, of the separation ramp while maintaing the same height or even increasing it in relation to the boundary layer thickness. This could be done in the present section by moving the ramp upstream. Furthermore, if two inverted rows

of VGJs are being tested the number of jet pairs should be increased as much as possible to minimize the relative difference in the number of strong/weak downwash regions.

It is apparent from the present results that for such a highly 3D flow perturbation streamwise planes at multiple spanwise locations would be desirable. A good approach would be to use three streamwise, wall normal planes, with one running along a jet wake (like plane 1 in this work) and two positioned in the middle of the strong and weak downwash regions. It would also have been beneficial to increase the streamwise extent of the wall parallel plane all the way to the end of the separation bubble.

Finally, while wool tufts were used during the set-up of this experiment and particularly the adjustment of the ceiling, proper image sequences of the tufts weren't acquired. This would be a cost effective and fast way of assessing both the topology of the baseline flow, particularly the three-dimensionality, as well as the effects of control. To make sure that high quality data was collected, fluorescent micro-tufts should be used. They would be distributed across the ramp and imaged from the same camera position used for the wall parallel PIV plane in this research.

References

Abdolahipour, S., Mani, M., & Shams Taleghani, A. (2022). Experimental investigation of flow control on a high-lift wing using modulated pulse jet vortex generator. *Journal of Aerospace Engineering*, *35*(5).

Adrian, R. J., Meinhart, C. D., & Tomkins, C. D. (2000). Vortex organization in the outer region of the turbulent boundary layer. *Journal of Fluid Mechanics*, *422*, 1–54.

Adrian, R. J. (2007). Hairpin vortex organization in wall turbulence. *Physics of Fluids*, *19*(4), 041301.

Alberty, J., Carstensen, C., & Funken, S. A. (1999). *Remarks around 50 lines of Matlab: short finite element implementation* (tech. rep.).

Amitay, M., & Glezer, A. (2002). Role of actuation frequency in controlled flow reattachment over a stalled airfoil. *AIAA Journal*, *40*(2), 209–216.

Aram, S., & Mittal, R. (2011). Computational study of the effect of slot orientation on synthetic jet-based separation control. *International Journal of Flow Control*, *3*(2-3), 87–109.

Barros, D., Borée, J., Noack, B. R., Spohn, A., & Ruiz, T. (2016). Bluff body drag manipulation using pulsed jets and Coanda effect. *Journal of Fluid Mechanics*, *805*, 422–459.

Bhattacharjee, S., Scheelke, B., & Troutt, T. R. (1986). Modification of vortex interactions in a reattaching separated flow. *AIAA journal*, *24*(4), 623–629.

Bidan, G., & Nikitopoulos, D. E. (2013). On steady and pulsed low-blowing-ratio transverse jets. *Journal of Fluid Mechanics*, *714*, 393–433.

Browand, F. K., & Troutt, T. R. (1985). The turbulent mixing layer: geometry of large vortices. *Journal of Fluid Mechanics*, *158*, 489–509.

Brown, G. L., & Roshko, A. (1974). On density effects and large structure in turbulent mixing layers. *Journal of Fluid Mechanics*, *64*(4), 775–816.

Brunn, A., & Nitsche, W. (2006). Active control of turbulent separated flows over slanted surfaces. *International Journal of Heat and Fluid Flow*, *27*(5), 748–755.

Cambonie, T., & Aider, J. L. (2014). Transition scenario of the round jet in crossflow topology at low velocity ratios. *Physics of Fluids*, *26*(8).

Castillo, L., Wang, X., & George, W. K. (2004). Separation Criterion for Turbulent Boundary Layers Via Similarity Analysis. *Journal of Fluids Engineering*, *126*(3), 297–304.

Cattafesta, L. N., & Sheplak, M. (2011). Actuators for active flow control. *Annual Review of Fluid Mechanics*, *43*, 247–272.

Cebeci, T., & Bradshaw, P. (1977). *Momentum transfer in boundary layers*.

Choi, H., Jeon, W. P., & Kim, J. (2008). Control of flow over a bluff body. *Annual Review of Fluid Mechanics*, *40*, 113–139.

Clauser, F. H. (1956). The turbulent boundary layer. *Advances in applied mechanics*, *4*, 1–51.

Coles, D. (1956). The law of the wake in the turbulent boundary layer. *Journal of Fluid Mechanics*, *1*(2), 191–226.

Coles, D. (1969). Computation of turbulent boundary layers. *In AFOSR-IFP Stanford Conference, CA*.

Compton, D. A., & Johnston, J. P. (1992). Streamwise vortex production by pitched and skewed jets in a turbulent boundary layer. *AIAA Journal*, *30*(3), 640–647.

Cossu, C., Pujals, G., & Depardon, S. (2009). Optimal transient growth and very large-scale structures in turbulent boundary layers. *Journal of Fluid Mechanics*, *619*, 79–94.

Dacome, G. (2021). *Delft-Aerospace TBL flow characterization*.

Dacome, G., & Baars, W. J. (2023). Private communication.

Dandois, J., Garnier, E., & Sagaut, P. (2007). Numerical simulation of active separation control by a synthetic jet. *Journal of Fluid Mechanics*, *574*, 25–58.

Debien, A., Aubrun, S., Mazellier, N., & Kourta, A. (2014). Salient and smooth edge ramps inducing turbulent boundary layer separation: Flow characterization for control perspective. *Comptes Rendus - Mecanique*, *342*(6-7), 356–362.

Debien, A., Aubrun, S., Mazellier, N., & Kourta, A. (2015). Active separation control process over a sharp edge ramp. *9th International Symposium on Turbulence and Shear Flow Phenomena, TSFP 2015*, *1*.

Delery, J. M. (1994). Aspects of vortex breakdown. *Progress in Aerospace Sciences*, *30*(1), 1–59.

Diaz-Daniel, C., Laizet, S., & Vassilicos, J. C. (2017). Wall shear stress fluctuations: Mixed scaling and their effects on velocity fluctuations in a turbulent boundary layer. *Physics of Fluids*, *29*(5), 55–102.

Dimotakis, P. E., & Brown, G. L. (1976). The mixing layer at high Reynolds number: large-structure dynamics and entrainment. *Journal of Fluid Mechanics*, *78*(3), 535–560.

Durst, F., & Tropea, C. (1983). Flows over two-dimensional backward - facing steps. In *Structure of complex turbulent shear flow* (pp. 41–52). Springer.

Eaton, J. K. (1980). *Turbulent flow reattachment: an experimental study of the flow and structure behind a backward-facing step*. Stanford University.

Eroglu, A., & Breidenthal, R. E. (2001). Structure, penetration, and mixing of pulsed jets in crossflow. *AIAA journal*, *39*(3), 417–423.

Ersoy, S., & Walker, J. D. (1985). Viscous flow induced by counter-rotating vortices. *Physics of Fluids*, *28*(9), 2687–2698.

Fric, T. F., & Roshko, A. (1994). Vortical Structure in the Wake of a Transverse Jet. *Journal of Fluid Mechanics*, *279*, 1–47.

Gad-el-Hak, M., & Bushnell, D. M. (1991). Separation control: Review. *Journal of Fluids Engineering*.

Ganapathisubramani, B., Clemens, N. T., & Dolling, D. S. (2007). Effects of upstream boundary layer on the unsteadiness of shock-induced separation. *Journal of Fluid Mechanics*, *585*, 369–394.

Glezer, A. (2011). Some aspects of aerodynamic flow control using synthetic-jet actuation. *Philosophical Transactions of the Royal Society A: Mathematical, Physical and Engineering Sciences*, *369*(1940), 1476–1494.

Glezer, A., & Amitay, M. (2002). Synthetic jets. *Annual Review of Fluid Mechanics*, *34*, 503–529.

Godard, G., Foucaut, J. M., & Stanislas, M. (2006). Control of a decelerating boundary layer. Part 2: Optimization of slotted jets vortex generators. *Aerospace Science and Technology*, *10*(5), 394–400.

Godard, G., & Stanislas, M. (2006). Control of a decelerating boundary layer. Part 3: Optimization of round jets vortex generators. *Aerospace Science and Technology*, *10*(6), 455–464.

Greenblatt, D., & Wygnanski, I. J. (2000). The control of flow separation by periodic excitation. *Progress in Aerospace Sciences*, *36*, 487–545.

Hasan, M., & Khan, A. (1992). On the instability characteristics of a reattaching shear layer with nonlaminar separation. *International Journal of Heat and Fluid Flow*, *13*(3), 224–231.

Ho, C. M., & Huerre, P. (1984). Perturbed free shear layers. *Annual Review of Fluid Mechanics*, *16*, 365–424.

Hussain, A. K. M. F., & Reynolds, W. C. (1970). The mechanics of an organized wave in turbulent shear flow. *Journal of Fluid Mechanics*, *41*(2), 241–258.

Hutchins, N., & Marusic, I. (2007a). Evidence of very long meandering features in the logarithmic region of turbulent boundary layers. *Journal of Fluid Mechanics*, *579*, 1–28.

Hutchins, N., & Marusic, I. (2007b). Large-scale influences in near-wall turbulence. *Philosophical Transactions of the Royal Society A: Mathematical, Physical and Engineering Sciences*, *365*(1852), 647–664.

Jabbal, M., & Zhong, S. (2010). Particle image velocimetry measurements of the interaction of synthetic jets with a zero-pressure gradient laminar boundary layer. *Physics of Fluids*, *22*(6), 063603.

Johnston, J. P., & Nishi, M. (1990). Vortex generator jets - means for flow separation control. *AIAA Journal*, *28*(6), 989–994.

Kelso, R. M., Lim, T. T., & Perry, A. E. (1996). An experimental study of round jets in cross-flow. *Journal of Fluid Mechanics*, *306*, 111–144.

Kim, W., Kim, C., & Jung, K. J. (2012). Separation control characteristics of synthetic jets depending on exit configuration. *AIAA Journal*, *50*(3), 559–570.

Kiya, M., Shimizu, M., & Mochizuki, O. (1997). Sinusoidal forcing of a turbulent separation bubble. *Journal of Fluid Mechanics*, *342*, 119–139.

Klebanoff, P. S., & Diehl, Z. W. (1952). *Some features of artificially thickened fully developed turbulent boundary layers with zero pressure gradient* (tech. rep.). NACA.

Koklu, M. (2018). Effects of Sweeping Jet Actuator Parameters on Flow Separation Control. *AIAA Journal*, *56*(1), 100–110.

Krothapalli, A., Lourenco, L., & Buchlin, J. M. (1990). Separated flow upstream of a jet in a crossflow. *AIAA Journal*, *28*(3), 414–420.

Lardeau, S., & Leschziner, M. A. (2011). The interaction of round synthetic jets with a turbulent boundary layer separating from a rounded ramp. *Journal of Fluid Mechanics*, *683*, 172–211.

Lee, J. H. (2017). Large-scale motions in turbulent boundary layers subjected to adverse pressure gradients. *Journal of Fluid Mechanics*, *810*, 323–361.

Leschziner, M. A., & Lardeau, S. (2011). Simulation of slot and round synthetic jets in the context of boundary-layer separation control. *Philosophical Transactions of the Royal Society A: Mathematical, Physical and Engineering Sciences*, *369*(1940), 1495–1512.

Lim, T. T., New, T. H., & Luo, S. C. (2001). On the development of large-scale structures of a jet normal to a cross flow. *Physics of Fluids*, *13*(3), 770–775.

Lin, J. C. (1992). *Control of Low-Speed Turbulent Separated Flow Over a Backward-Facing Ramp* (Doctoral dissertation).

Lin, J. C. (2002). Review of research on low-profile vortex generators to control boundary-layer separation. *Progress in Aerospace Sciences*, *38*, 389–420.

Lock, R. C., & Williams, B. R. (1987). Viscous-inviscid interactions in external aerodynamics. *Progress in Aerospace Sciences*, *24*, 51–171.

Mahesh, K. (2013). The interaction of jets with crossflow. *Annual Review of Fluid Mechanics*, *45*, 379–407.

Marusic, I., Mathis, R., & Hutchins, N. (2010). High Reynolds number effects in wall turbulence. *International Journal of Heat and Fluid Flow*, *31*(3), 418–428.

Mohammed-Taifour, A., & Weiss, J. (2016). Unsteadiness in a large turbulent separation bubble. *Journal of Fluid Mechanics*, *799*, 383–412.

Mohammed-Taifour, A., & Weiss, J. (2021). Periodic forcing of a large turbulent separation bubble. *Journal of Fluid Mechanics*, *915*.

Monkewitz, P. A. (1982). Influence of the velocity ratio on the spatial instability of mixing layers. *Physics of Fluids*, *25*(7), 1137.

Morris, S. C., & Foss, J. F. (2003). Turbulent boundary layer to single-stream shear layer: The transition region. *Journal of Fluid Mechanics*, *494*, 187–221.

Muppidi, S., & Mahesh, K. (2006). Two-dimensional model problem to explain counter-rotating vortex pair formation in a transverse jet. *Physics of Fluids*, *18*(8), 085103.

O'Meara, M. M., & Mueller, T. J. (1987). Laminar separation bubble characteristics on an airfoil at low Reynolds numbers. *AIAA Journal*, *25*(8), 1033–1041.

Ortmanns, J., Bitter, M., & Kähler, C. J. (2008). Dynamic vortex structures for flow-control applications. *Experiments in Fluids*, *44*(3), 397–408.

Oster, D., Wygnanski, I., Dziomba, B., & Fiedler, H. (1978). On the effect of initial conditions on the two dimensional turbulent mixing layer. In *Structure and mechanisms of turbulence i* (pp. 48–64). Springer.

Pearson, D. S., Goulart, P. J., & Ganapathisubramani, B. (2013). Turbulent separation upstream of a forward-facing step. *Journal of Fluid Mechanics*, *724*, 284–304.

Perlin, M., Dowling, D. R., & Ceccio, S. L. (2016). Freeman Scholar Review: Passive and Active Skin-Friction Drag Reduction in Turbulent Boundary Layers. *Journal of Fluids Engineering*, *138*(9).

Pope, S. B. (2000). *Turbulent Flows*. Cambridge University Press.

Ramírez Vázquez, G. (2022). *Experimental investigation on the use of Helmholtz resonators for turbulent separation control (MSc thesis)*. TU Delft.

Sau, R., & Mahesh, K. (2008). Dynamics and mixing of vortex rings in crossflow. *Journal of Fluid Mechanics*, *604*, 389–409.

Schlichting, H., & Gersten, K. (2016). *Boundary-Layer Theory*. Springer Berlin Heidelberg.

Scholz, P., Kähler, C. J., Radespiel, R., Scholz, P., Ortmanns, J., Kähler, C. J., & Radespiel, R. (2005). Performance optimization of jet actuator arrays for active flow control. *CEAS/KATnet Conference on Key Aerodynamic Technologies*.

Seifert, A., Eliahu, S., Greenblatt, D., & Wygnanski, I. (1998). Use of piezoelectric actuators for airfoil separation control. *AIAA Journal*, *36*(8), 1535–1537.

Selby, G. V., Lin, J. C., & Howard, E. G. (1992). Control of low-speed turbulent separated flow using jet vortex generators. *Experiments in Fluids*, *12*, 394–400.

Sigurdson, L. W. (1995). The structure and control of a turbulent reattaching flow. *Journal of Fluid Mechanics*, *298*, 139–165.

Simmons, D. J., Thomas, F. O., Corke, T. C., & Hussain, F. (2022). Experimental characterization of smooth body flow separation topography and topology on a two-dimensional geometry of finite span. *Journal of Fluid Mechanics*, *944*.

Simpson, R. L. (1996). Aspects of turbulent boundary layer separation. *Progress in Aerospace Sciences*, *32*, 457–521.

Simpson, R. L., Chew, Y. T., & Shivaprasad, B. G. (1981). The structure of a separating turbulent boundary layer. Part 2. Higher-order turbulence results. *Journal of Fluid Mechanics*, *113*, 53–73.

Simpson, R. L., Strickland, J. H., & Barr, P. W. (1977). Features of a separating turbulent boundary layer in the vicinity of separation. *Journal of Fluid Mechanics*, *79*(3), 553–594.

Smith, D. R. (2002). Interaction of a synthetic jet with a crossflow boundary layer. *AIAA Journal*, *40*(11), 2277–2288.

Smits, A. J., McKeon, B. J., & Marusic, I. (2011). High-Reynolds number wall turbulence. *Annual Review of Fluid Mechanics*, *43*, 353–375.

Song, S., & Eaton, J. K. (2004). Flow structures of a separating, reattaching, and recovering boundary layer for a large range of Reynolds number. *Experiments in Fluids*, *36*(4), 642–653.

Squire, H. B. (1933). On the stability for three-dimensional disturbances of viscous fluid flow between parallel walls. *Proceedings of the Royal Society of London. Series A, Containing Papers of a Mathematical and Physical Character*, *142*(847), 621–628.

Stanek, M., Raman, G., Ross, J., Odedra, J., Peto, J., Alvi, F., & Kibens, V. (2002). High frequency acoustic suppression - The role of mass flow & the notion of superposition. *8th AIAA/CEAS Aeroacoustics Conference & Exhibit*.

Steinfurth, B., & Weiss, J. (2022). Efficiency enhancement in active separation control through optimizing the duty cycle of pulsed jets. *AIAA Journal*, 1–15.

Taira, K., Brunton, S. L., Dawson, S. T., Rowley, C. W., Colonius, T., McKeon, B. J., Schmidt, O. T., Gordeyev, S., Theofilis, V., & Ukeiley, L. S. (2017). Modal analysis of fluid flows: An overview. *AIAA Journal*, *55*(12), 4013–4041.

Tricouros, F. A., Amitay, M., & Van Buren, T. (2022). Comparing steady and unsteady rectangular jets issuing into a crossflow. *Journal of Fluid Mechanics*, *942*.

Van Buren, T., Leong, C. M., Whalen, E., & Amitay, M. (2016). Impact of orifice orientation on a finite-span synthetic jet interaction with a crossflow. *Physics of Fluids*, *28*(3).

Vukasinovic, B., Lucas, D. G., & Glezer, A. (2005). Controlled manipulation of small- and large- scales in a turbulent shear layer, Part I: Experimental studies. *35th AIAA Fluid Dynamics Conference and Exhibit*.

Walan, A. M., & Lydecker, J. (2023). DARPA CRANE Program Overview. *AIAA SCITECH 2023 Forum*.

White, F. (2006). *Viscous Fluid Flow* (3rd Edition). McGraw-Hill.

Wu, W., Meneveau, C., & Mittal, R. (2019). Spatio-Temporal dynamics of turbulent separation bubbles. *Journal of Fluid Mechanics*, *883*.

Wu, W., Meneveau, C., Mittal, R., Padovan, A., Rowley, C. W., & Cattafesta, L. (2022). Response of a turbulent separation bubble to zero-net-mass-flux jet perturbations. *Physical Review Fluids*, *7*(8).

Wu, X., & Moin, P. (2009). Direct numerical simulation of turbulence in a nominally zero-pressure-gradient flat-plate boundary layer. *Journal of Fluid Mechanics*, *630*, 5–41.

Zhang, S., & Zhong, S. (2011). Turbulent flow separation control over a two-dimensional ramp using synthetic jets. *AIAA Journal*, *49*(12), 2637–2649.

Zhong, S., Jabbal, M., Tang, H., Garcillan, L., Guo, F., Wood, N., & Warsop, C. (2007). Towards the Design of Synthetic-jet Actuators for Full-scale Flight Conditions. *Flow, Turbulence and Combustion*, *78*(3-4), 283–307.

Zhong, S., & Zhang, S. (2013). Further examination of the mechanism of round synthetic jets in delaying turbulent flow separation. *Flow, Turbulence and Combustion*, *91*(1), 177–208.

Zhou, J., & Zhong, S. (2010). Coherent structures produced by the interaction between synthetic jets and a laminar boundary layer and their surface shear stress patterns. *Computers and Fluids*, *39*(8), 1296–1313.

A

Additional results

A.1. Phase averaged velocity fields

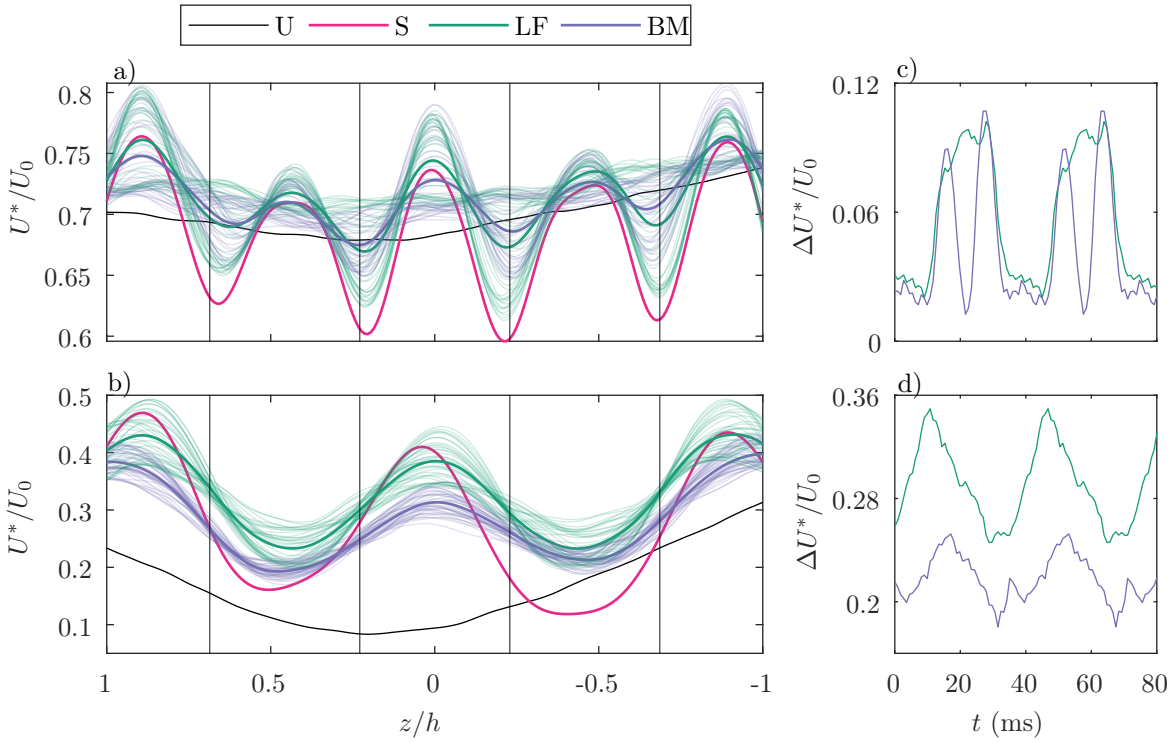

Figure A.1: Streamwise velocity U^* in plane 2 for steady and 3D1 LF and BM control. Time and phase averaged velocity profiles at (a) upstream and (b) downstream edges of plane 2 edges (thick line: time average, thin lines: phase average). Phase-averaged velocity response at $z = 0$ on the (c) upstream and (d) downstream edge given as difference to uncontrolled.

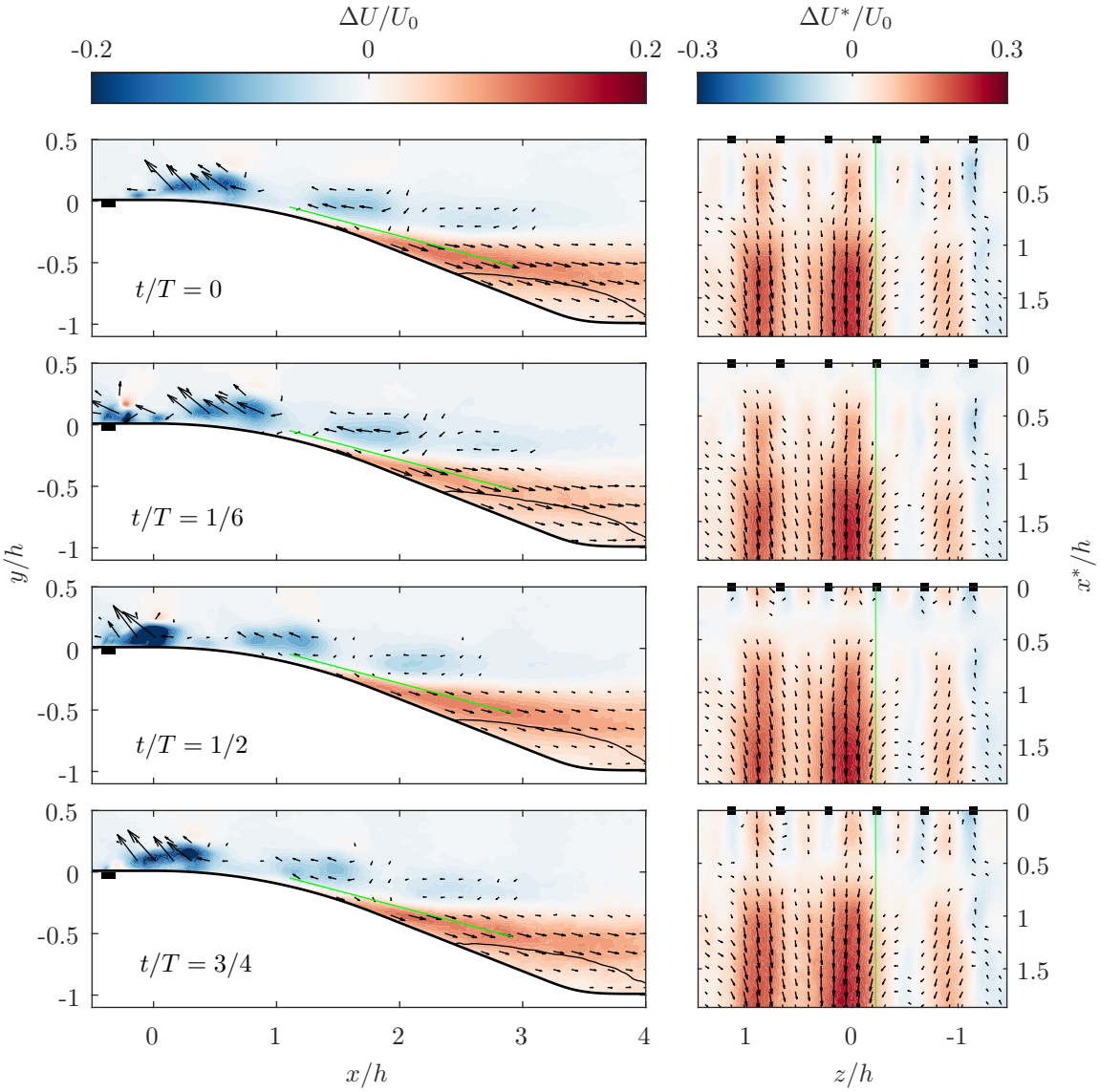

Figure A.2: Phase averaged velocity fields for 3D1 HF forcing shown relative to the uncontrolled baseline. Green lines: PIV plane intersection.

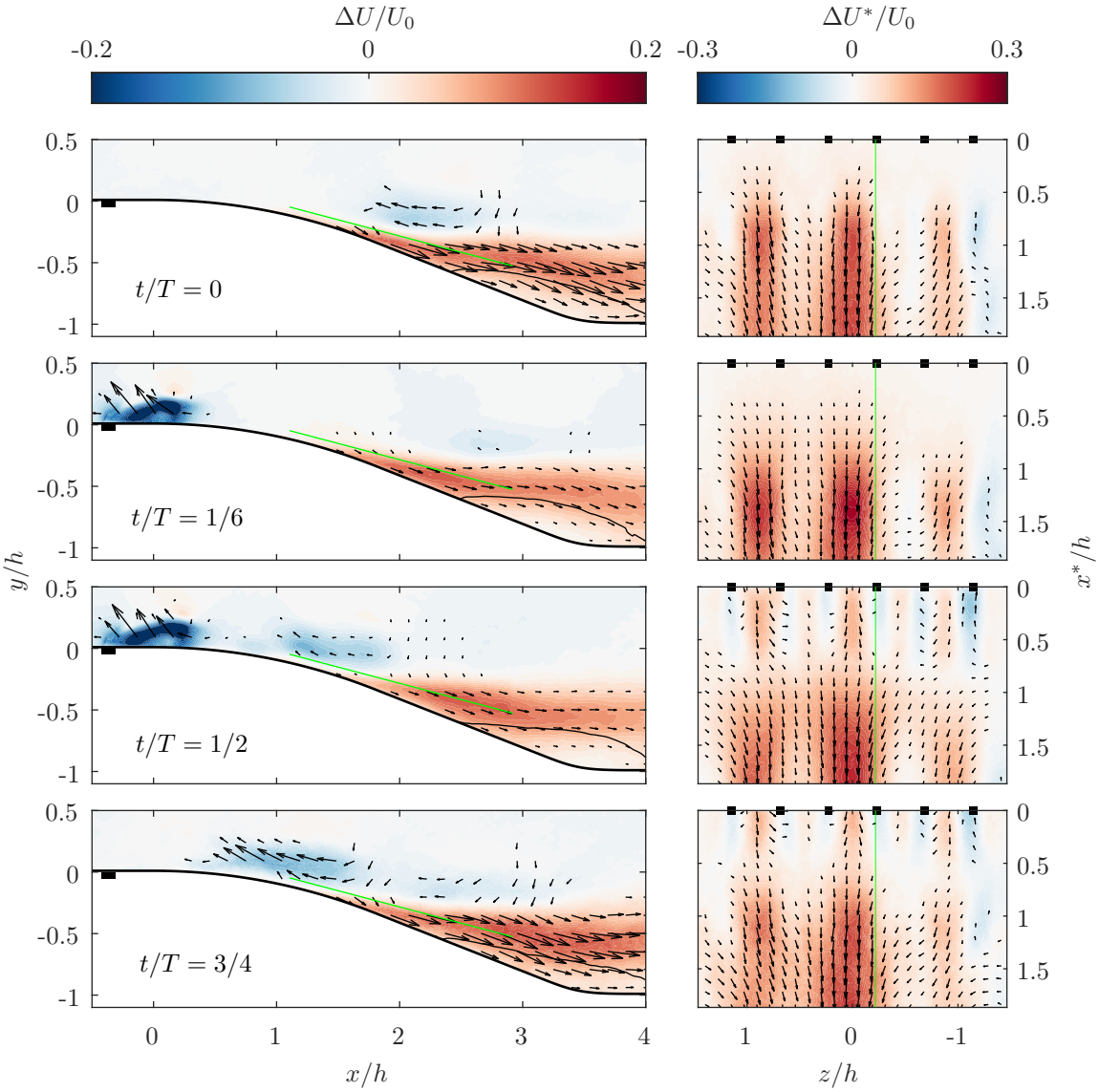

Figure A.3: Phase averaged velocity fields for 3D1 BM forcing shown relative to the uncontrolled baseline. Green lines: PIV plane intersection.